

Few-Body Interactions in an Ultracold Gas of Cesium Atoms

Dissertation
von

Phillip-Tobias Kraemer

zur Erlangung des Doktorgrades
an der Fakultät für Mathematik, Informatik und Physik
der Leopold-Franzens-Universität Innsbruck

durchgeführt am
Institut für Experimentalphysik
unter der Leitung von
Univ.-Prof. Dr. Rudolf Grimm

Innsbruck im Oktober 2006

Abstract

This work shows experiments exploring few-body quantum physics in the zero-energy limit. Three-body and four-body interactions are addressed. Experimental evidence for Efimov quantum states in an ultracold gas of Cs atoms and the observation of magnetically tunable inelastic collision resonances in an ultracold gas of Cs₂ dimers is presented.

We experiment on ¹³³Cs in the energetically lowest, low-field seeking hyperfine ground state at low magnetic fields trapped by far red-detuned optical dipole traps which are loaded from an optically pre-cooled atomic cloud. We can tune the two-body interaction strength via an entrance-channel dominated magnetic Feshbach resonance. We can prepare optically trapped samples of ultracold Cs₂ dimers by Feshbach association from an atomic Bose-Einstein condensate. Accurate measurements of the three-body loss rate coefficient are facilitated by the fact that spin-changing collisions are endothermic, meaning inelastic two-body losses are energetically suppressed.

In the limit of resonant two-body interaction a series of universal three-body bound states, called Efimov states, exists. Striking manifestations of Efimov states have been predicted for three-body recombination processes. We observe the rate of inelastic trap loss involving three Cs atoms and map out the dependence of the three-body loss rate coefficient α_{rec} on the scattering length a . To avoid undue thermal averaging and unitary limitation, we create thermal samples of a few nK by collapsing a Bose-Einstein condensate of Cs atoms. Our measurements concentrate on the universal regime of resonant two-body interaction. We recover the well-established universal a^4 -scaling law for negative and positive, large values of the scattering length. Furthermore we observe a resonant enhancement of three-body losses in the region where $a < 0$, and a suppression of three-body losses in the region where $a > 0$. We attribute these features to the presence of Efimov quantum states. This is the first instant of experimental access to Efimov quantum states.

As first small step towards experimentally exploring four-body interactions, we observe the rate of inelastic binary collisions in an ultracold gas of Cs₂ dimers as a function of the magnetic field strength. By tuning the external magnetic field strength we vary the binding energy of the molecules on a scale corresponding to a few MHz and we transfer the molecules from the initial state into another molecular bound state by following the upper branch of an avoided level crossing. In this second molecular state two Feshbach-like collision resonances show up as strong inelastic loss features. We interpret these resonances as being induced by the presence of Cs₄ bound states, or tetramers, near the molecular scattering continuum.

Investigating few-body physics with ultracold atomic and molecular quantum gases is a newly emerging field of research. Universal aspects of three-body and four-body interactions might reveal universal effects in larger compounds. Understanding few-body systems is of great relevance to various fields of physics and future measurements will benefit from the exceptionally high degree of control over the internal and external degrees of freedom achievable in ultracold quantum gases.

Zusammenfassung

Diese Arbeit stellt Experimente zur Physik quantenmechanischer Systeme aus jeweils drei und vier Teilchen vor. Sie ist somit ein Schritt in Richtung der Erforschung von Systemen aus mehreren Teilchen. Ein experimenteller Nachweis von Efimov-Quantenzuständen in einem ultrakalten Gas aus Cs-Atomen und die Beobachtung magnetisch verstimmbarer Resonanzen der inelastischen Kollisionsrate in einem ultrakalten Gas aus Cs₂-Dimeren werden präsentiert.

Wir arbeiten mit in optischen Dipolfallen gefangenen ultrakalten Ensembles aus ¹³³Cs-Atomen im energetisch niedrigsten Hyperfein-Zustand bei kleinen magnetischen Feldstärken. Die Zweikörperwechselwirkung ist mithilfe einer Feshbach-Resonanz verstimmbar. Optisch gefangene Wolken aus Cs₂ können durch Feshbach-Assoziation von einem Cs Bose-Einstein-Kondensat hergestellt werden. Präzise Messungen des Dreikörper-Verlustkoeffizienten sind möglich, weil inelastische Zweikörperverluste endothermisch und somit energetisch unterdrückt sind.

Im Limes einer resonanten Zweikörperwechselwirkung treten universelle gebundene Dreikörperzustände, sogenannte Efimov-Zustände, auf. Diese haben starken Einfluss auf Dreikörper-Rekombinationsprozesse. Wir beobachten den Dreikörperverlustkoeffizient α_{rec} als Funktion der Streulänge a . Um Limitierungen durch Temperatureffekte weitestgehend zu vermeiden, arbeiten wir mit thermischen Wolken deren Temperatur im Bereich weniger nK liegt. Unsere Messungen konzentrieren sich auf den universellen Bereich resonanter Zweikörperwechselwirkung und bestätigen die bereits bekannte, generelle a^4 -Skalierung. Darüberhinaus zeigt sich eine resonante Überhöhung von α_{rec} für $a < 0$ und eine Unterdrückung von α_{rec} für $a > 0$. Diese Effekte belegen die Existenz von Efimov-Quantenzuständen und stellen den ersten experimentellen Nachweis dieser exotischen Zustände dar.

Als einen experimentellen Zugang zur Wechselwirkung von vier Teilchen untersuchen wir inelastische Kollisionen von zwei Cs₂-Molekülen als Funktion der magnetischen Feldstärke. Indem wir diese ändern, variieren wir die Bindungsenergie der Moleküle im Bereich entsprechend einiger MHz. Auch werden die Dimere dabei vom anfänglichen Molekülzustand in einen weiteren gebundenen Molekülzustand überführt. Dieser Transfer ergibt sich zwanglos aus einer vermiedenen Kreuzung der betreffenden Zustände. In dem zweiten Molekülzustand beobachten wir magnetisch verstimmbare Verlustresonanzen. Diese interpretieren wir als Zeichen einer magnetfeldabhängigen Kopplung zwischen Cs₄-Zuständen und dem Streuzustand zweier Dimere.

Die Untersuchung von Mehrteilchensystemen mit ultrakalten atomaren und molekularen Quantengasen ist ein im Entstehen begriffenes Forschungsfeld. Universelle Eigenschaften von Drei- und Vierkörperwechselwirkungen könnten universelle Effekte in noch größeren Systemen enthüllen. Das Verständnis der Physik von Mehrteilchensystemen ist für eine Reihe von Forschungsfeldern von hohem Interesse. Zukünftige Messungen werden davon profitieren, daß ultrakalte Quantengase eine fast vollständige Kontrolle über die internen und externen Freiheitsgrade des Systems erlauben.

Contents

1 Introduction	9
2 Scientific background: Feshbach tuning and association of molecules in ultracold gases	11
2.1 A short history of Feshbach molecules	12
2.2 Scattering at ultra-low temperatures and Feshbach resonances	13
2.2.1 Feshbach resonances	14
2.2.2 Classification of Feshbach resonances	15
2.3 The simple picture of Feshbach association	16
3 Review on two-body interactions and dimer states in Cesium	19
3.1 Overview: two-body interactions of cold Cesium atoms	19
3.2 Selection rules for collision-induced transitions	20
3.3 Cesium molecular energy structure and low energy scattering behavior	22
3.3.1 $l = 0$ Feshbach resonances	22
3.3.2 $l \neq 0$ Feshbach resonances	26
4 Experimental set-up and preparation methods	29
4.1 Overview: strategy for atomic sample preparation	29
4.2 Vacuum system	30
4.3 Magnetic field control	31
4.4 Optical pre-cooling	33
4.4.1 Laser setup	33
4.4.2 Performance of laser cooling	34
4.5 Optical dipole traps	34
4.5.1 Reservoir trap and levitation	34
4.5.2 Dimple trap	36
4.5.3 Elliptic trap	36
4.6 Bose-Einstein condensation of Cesium atoms	38
4.7 Diagnostics	39
5 Three-body interactions: Measurements of three-body recombination and evidence for Efimov quantum states	41
5.1 Efimov effect	42
5.1.1 Three-body scattering formalism	43
5.1.2 Jacobian coordinates and decomposition at low energy	45

5.1.3	Hyperspherical channel potentials and Efimov effect	47
5.1.4	Efimov's scenario	50
5.1.5	The search for Efimov effects so far	50
5.2	Efimov states in ultracold gases	52
5.2.1	Signature of trap loss	53
5.2.2	Three-body recombination as a function of scattering length	54
5.2.3	Temperature limitations to the observation of three-body recombination	55
5.3	Experimental access to the universal regime	56
5.4	Results from three-body recombination loss measurements	57
5.4.1	Trapping parameters for recombination loss measurements	60
5.4.2	Discussion	61
5.5	Quantitative analysis of three-body trap loss	62
5.5.1	Mathematical model	63
5.5.2	Statistical error	65
6	Four-body interactions: Dimer-dimer collisions and the observation of Feshbach-like resonances	67
6.1	Preparation of pure samples of trapped ultracold Cs ₂ dimers	68
6.1.1	Molecule production	68
6.1.2	Molecule detection	70
6.1.3	Cesium dimers and the reservoir trap	71
6.2	Observation of resonance phenomena in trap loss	74
7	Outlook	77
A	Current control circuit	83
B	Publications	85
B.1	Preparation of a pure molecular quantum gas	85
B.2	Optimized production of a cesium Bose-Einstein condensate	90
B.3	Efficient creation of molecules from a cesium Bose-Einstein condensate	98
B.4	Observation of Feshbach-Like Resonances in Collisions between Ultracold Molecules	106
B.5	Evidence for Efimov quantum states in an ultracold gas of caesium atoms	111
	References	116

CHAPTER 1

Introduction

The field of ultracold atomic quantum gases has met with spectacular success over the last ten years. The first sensational breakthrough was the creation of Bose-Einstein condensates (BECs) [Bos24, Ein25] in dilute atomic alkali gases in 1995 [And95, Dav95]. Since then, atomic quantum gases have led to new developments well beyond traditional atomic, molecular and optical physics. Atomic quantum gases have opened up the new field of matter-wave lasers and nonlinear matter-wave optics, and they have contributed to diverse areas such as condensed matter physics, plasma physics and quantum information. Experimental highlights include the direct observation of the quantum phase transition from a superfluid to a Mott insulator [Gre02] and the observation of fermionization in one-dimensional bosonic systems [Par04, Kin04]. The year 2003 witnessed a major breakthrough in the field of cold molecules when pure samples of diatomic molecules, called dimers, were produced by controlled association from ultracold atomic gases [Her03, Dür04a, Joc03b, Reg03, Xu03]. Shortly thereafter Bose-Einstein condensates of molecules [Joc03a, Gre03, Zwi03] were created. These experiments exploited couplings of two-body bound states to the atomic scattering state, a scenario referred to as Feshbach resonance [Fes58]. The feasibility of dimer association using a Feshbach resonance, called Feshbach association, had been demonstrated in 2002 [Don02] but the dimers could not be probed directly at that time. The achievement of molecular BECs facilitated studies on the conversion of a condensate of molecules into a superfluid of Cooper-pairs and on the properties of the transient regime [Bar04b, Bar04a, Chi04a, Zwi05]. These developments highlight that ultracold quantum gases have revolutionized the understanding of two-body physics and set milestones in the field of many-body physics. Experiments with ultracold atoms and dimer molecules aimed at the exploration of few-body systems are presented in this thesis. They address the presence and properties of certain three-body bound states, called Efimov states, and of four-body bound states of Cesium (Cs) atoms in the ultracold limit.

The wavefunction of a two-body bound state energetically close to the dissociation threshold is independent of the particular nature of the forces acting between the particles. Such wavefunctions concentrate their weight outside the range of the binary interaction and feature almost no probability amplitude within that range. They are therefore called halo-states [Jen04] and feature universal properties in the sense that structural details of the two-body forces are unimportant. In 1970, V. Efimov discovered that such universality for two identical bosons implies universal properties for the

corresponding three-body spectrum [Efi70, Efi71]. This discovery allowed him to find a solution to the notoriously complex problem of three interacting particles. Various nuclear systems [Jen04] and the ^4He trimer were put forward [Brü05] as supporting favorable conditions for the observation of Efimov states. For over 35 years, however, Efimov quantum states eluded their experimental detection. Now, using the tunability of a universal dimer state in the vicinity of a Feshbach resonance, we have been able to find experimental evidence for the existence of these exotic states in careful measurements of three-body recombination loss at ultralow temperatures [Kra06].

Within the context of Feshbach association of molecules [Köh06] from ultracold atomic gases the Cesium atom plays a special role because of the unique dimer level structure just below dissociation threshold. Given the remarkable complexity of interaction between Cs atoms, it is plausible to expect some coupling of Cs dimers to more complex structures. Starting from *diatomic* molecules, couplings to *four-body* bound states might induce a scenario analogous to the atom-dimer case, opening the door to zero-energy four-body interactions. We have found such Feshbach-like collision resonances in collisions among ultracold dimers [Chi05].

This thesis is organized as follows. The second chapter puts this work into the general context of dimer association techniques in ultracold gases. A review of the research on and with Feshbach molecules is given in order to set this work in relation to ongoing research efforts. The third chapter gives a short outline of the binary interactions acting between Cs atoms and the resulting molecular energy structure just below threshold. Emphasis is given to the influence of the molecular states on the low-energy scattering properties which set Cs apart from the other alkali metals. The fourth chapter describes the experimental setup, special features of the apparatus and the key experimental methods we use to produce the high phase-space density atomic samples, thermal or quantum degenerate, which form the starting point of all our experiments.

The chapters five and six form the heart of this thesis. They show effects beyond two-body interactions. Chapter five introduces the Efimov effect as the only known analytical solution to the quantum mechanical three-body problem and describes Efimov physics within the context of ultracold gases. The measurements of three-body recombination and the data analysis indicating the existence of an Efimov state is presented. In chapter six, measurements are presented which hint at the presence of a tunable four-body bound state in the vicinity of the dimer-dimer scattering continuum. These measurements show Feshbach-like collision resonances among dimer-dimer scattering, representing a first small step towards the largely unknown territory of four-body interactions. The seventh chapter concludes this thesis by relating this work to ongoing and possible future measurements.

CHAPTER 2

Scientific background: Feshbach tuning and association of molecules in ultracold gases

The production of high-phase space density molecular samples in a trap is a tricky business. In contrast to the case of atoms laser cooling is not applicable to molecules due to the lack of closed optical transitions. In principle, there are two different approaches to the creation of translationally cold molecules.

One way is to prepare a source of molecules such as molecular vapors or beams as a starting point and create cold samples from that source. Examples following this line are the deceleration of polar molecules in a supersonic jet expansion with time-varying electric fields [Bet00], sympathetic cooling with a helium buffer gas [Wei98] or Coulomb crystals [Bly05], the doping of Helium nano-droplets with molecules [Mud04], and the velocity selection from a thermal source [Rie05]. Even though these methods have been shown to achieve mK temperatures, the resultant phase-space densities are rather low, providing molecular ensembles far away from quantum degeneracy.

The other way is to associate molecules from ultracold atomic samples. The molecular ensemble thus ‘inherits’ the low temperatures and high phase-space densities from the atomic ensemble. The viability of this idea has first been demonstrated by photo-associating molecules from trapped vapors of alkali atoms [Fio98]. In photo-association two colliding ground-state atoms are transferred to an excited molecular state by absorbing one photon. Ground state molecules are then formed by spontaneous de-excitation of the photo-associated molecules. Photo-association from pre-cooled atomic samples produces temperatures in the μK range [Fio98, MS01, Van02] but the phase-space density is still many orders of magnitude away from quantum degeneracy. Another method following the controlled-association idea is to exploit couplings of the two-atom scattering state to molecular states. These couplings result in scattering resonances, called Feshbach resonances, among the binary collisions of ultracold atoms. Feshbach resonances were originally introduced in nucleon scattering physics by Feshbach [Fes58] and first predicted in low-temperature atomic physics by Stwalley [Stw76]. The dimer association method using Feshbach resonances is by far more efficient than photo-association and has led to many ground-breaking discoveries during the last three years among which are the production of a molecular condensate [Joc03a, Gre03] and the production of a superfluid of Cooper-pairs [Chi04a, Zwi05].

Sec. 2.1 gives a short history of research on and with Feshbach-associated dimers. The properties of ultralow energy scattering and its connection to molecular bound

states is outlined in Sec. 2.2. In Sec. 2.3 the association of molecules using Feshbach resonances, called Feshbach association, is briefly reviewed.

2.1 A short history of Feshbach molecules

The year 2003 witnessed a major breakthrough when a number of experiments succeeded in making pure samples of ultracold molecules using Feshbach resonances. The existence of molecules created via Feshbach resonances had been reported previously in a BEC of ^{85}Rb atoms [Don02]. This study also demonstrated the coherence of the Feshbach coupling by observing oscillations between atomic and molecular populations. The existence of Feshbach molecules was also reported in thermal samples of ^{133}Cs [Chi03] and in degenerate Fermi gases of ^{40}K [Reg03]. However, the molecular ensembles produced in these experiments could not be probed directly. In our approach a separation of the atomic and molecular components immediately follows the Feshbach association [Her03]. Thus, starting with a BEC of Cs atoms, we were able to create pure molecular samples of high-phase space density. Thereupon followed similar experiments using ^{87}Rb [Dür04a] and ^{23}Na [Xu03], the latter directly proving the coherent nature of such out-coupled molecular matter waves. Shortly thereafter, Feshbach couplings were used to produce molecules from two-component degenerate Fermi gases [Joc03b, Cub03, Str03]. These dimers turned out to be surprisingly stable against collisional de-excitation. This stability was later attributed to the anti-symmetry of the fermionic constituents' wavefunction [Pet04]. The suppression of quenching collisions is termed Pauli-blocking.

With the long-lived molecules from fermionic atoms evaporation became possible and Bose-Einstein condensation of molecules was achieved [Joc03a, Gre03, Zwi03]. This development led to a wealth of investigations addressing the conversion of a condensate of molecules into a superfluid of Cooper-pairs and the properties of the transient regime [Bar04b, Bar04a, Chi04a, Zwi05], the so-called BEC-to-BCS crossover.

On the bosonic side the Feshbach dimers have proven to be rather fragile compounds which are highly susceptible to de-excitation during binary collisions, regarding both dimer-dimer and dimer-atom scattering. Lifetimes of trapped pure molecular samples and atom-dimer mixtures have been reported to exceed several ten milliseconds only at very low densities [Chi05] or within a lattice environment [Tha06] where the lattice suppresses tunneling among neighboring sites. For this reason trapping at high densities, evaporation or even the observation of a predicted quantum phase transition from an atomic to a molecular BEC [Rom04] seem difficult to achieve with dimers from bosonic atoms. Thus, present research efforts are concentrated on the association [Mar05, Hod05, Tho05b] and dissociation processes [Tho05a, Muk04, Dür04b, Dür05, Vol05], on single-molecule effects [Kra, AS05] and precision spectroscopy [Cla03, Mar07b], and on the dimer-dimer interactions [Muk04, Chi05, Sya06] and atom-dimer interactions [Muk04, Sya06, Smi06, Mar07a]. Here, collisions among very weakly bound dimers [Mar07a] are of special interest be-

cause the collision cross sections might be independent of the atomic species.

2.2 Scattering at ultra-low temperatures and Feshbach resonances

For a spherically symmetric interaction potential the elastic part of the scattering amplitude can be characterized by a phase shift for the scattering wave function before and after colliding. This becomes particularly simple when higher orbital angular momentum contributions are suppressed, i.e. when the collision energy is insufficient to overcome any centrifugal barrier. The remaining s -wave phase shift $\delta_0(k)$ in the zero-energy limit $k \rightarrow 0$, k being the wave vector of the relative motion, is quantified by the scattering length $a = -\lim_{k \rightarrow 0} \tan(\delta_0(k))/k$, reducing the effects of the complicated two-body interactions to one single number. For ultracold gases, the scattering length is a useful quantity. The sign of the scattering length determines whether the interaction is repulsive ($a > 0$) or attractive ($a < 0$). In the product na^3 , n being the atomic number density, the scattering length determines the diluteness of the gas and whether or not the two-body interaction can be treated as a small perturbation of an ideal gas [Met99]. The elastic scattering cross section scales as a^2 [Met99]. For large a , the rate of three-body collisions is proportional to a^4 , see Sec. 5.2.2 and references therein.

In the limit of large positive scattering lengths the connection between the molecular structure and scattering length becomes very simple. The binding energy E_b of the last bound molecular state is given by the well-known formula [Lan77, Köh06]

$$E_b = -\frac{\hbar^2}{ma^2}. \quad (2.1)$$

The condition for this limit is that the scattering length a must be much larger than the characteristic range of the interaction potential ℓ . The characteristic range of an alkali two-body potential is determined by the C_6/r^6 -tail of the interaction which is caused by induced dipoles as outlined in Sec. 3 for the case of Cs and called van-der-Waals interaction. It can be quantified by the van-der-Waals length $l_{vdW} = (mC_6/\hbar^2)^{1/4}/2$ [Köh06], and hence the condition $a \gg \ell$ can be expressed as

$$a \gg l_{vdW}. \quad (2.2)$$

In this so-called *universal regime* the wave function of the last bound state assumes the universal form

$$\phi(r) = \frac{1}{\sqrt{2\pi a}} \frac{e^{-r/a}}{r} \quad (2.3)$$

for sufficiently large inter-particle distances $r \gg r_{cl}$ where r_{cl} is the classical turning point for the molecular bound state given by

$$r_{cl} = \left[a (2l_{vdW})^2 \right]^{1/3}. \quad (2.4)$$

The molecular wave function has most of its weight outside of the classical region. Such molecules are known as *halo molecules* [Jen04, Köh06]. Note that in Eq. 2.3 the molecular potential enters only through the scattering length. In the universal regime the scattering length gives a direct measure for the mean distance between the two atoms, i.e. the molecular bond length:

$$\langle r \rangle = a/2. \quad (2.5)$$

As discussed in detail later on, experiments with ultracold atoms and molecules easily enter the regime $\langle r \rangle \gg r_{cl} > l_{vdW}$.

It is highly desirable to know and to control the value of the scattering length. Its value depends very sensitively on the presence of the last, most weakly bound molecular states. The presence of a molecular state, virtual or bound, dramatically effects a . If a virtual molecular state hovers just above threshold, the scattering length is large and negative. When the potential becomes a little bit deeper, just enough for the virtual state to become bound, a is large and positive. Right on resonance the scattering length diverges leading to a so-called zero-energy resonance. The two-body and three-body scattering cross sections are then governed by some other length scale such as the de-Broglie wavelength or the inverse Fermi-momentum of the atoms or the size of the trap. Throughout this thesis, a is given in units of Bohr's radius $a_0 \approx 0.53 \times 10^{-10}$ m.

2.2.1 Feshbach resonances

The Born-Oppenheimer interaction potential of two ground-state atoms with hyperfine interaction depend on the relative orientation of the two atomic spins. The various spin configurations define the so-called scattering channels. They are termed 'open' when their asymptotic energy, i.e. the potential energy at large internuclear distance, lies below the initial scattering state, and 'closed' in case the asymptotic energy lies above the initial scattering state. The spin configuration of the initial scattering state is called the entrance channel.

The magnetic tunability of the scattering length arises from the fact that entrance channel and closed channels respond differently to an external magnetic field when they have a different magnetic moment. Feshbach resonances occur when a molecular state belonging to another channel is tuned into degeneracy with the entrance channel. The properties of a Feshbach resonance depend on the coupling strength $|M|^2$ between the molecular and the atomic scattering state and the off-resonant background scattering length.

In the vicinity of a magnetic Feshbach resonance at B_0 the scattering length a shows a dispersive divergence as a function of the magnetic field strength B . a behaves as $a(B) = a_{bg}(1 - \Delta B/(B - B_0))$ in the limit of zero collision energy. Here, a_{bg} denotes the off-resonance background scattering length. The width of the resonance ΔB is determined by the difference in magnetic moments μ_{res} and the coupling strength $|M|^2$ between the atomic scattering state and the molecular state causing the resonance.

2.2 Scattering at ultra-low temperatures and Feshbach resonances

Following Ref. [Köh06], $\Delta B \propto |M|^2 / (a_{bg} \mu_{res})$. For alkali atoms, μ_{res} is typically on the order of one Bohr magneton μ_B . The Feshbach resonance widths, however, can vary from μG to hundreds of Gauss due to the variation in $|M|^2$.

In this thesis Feshbach resonances are labeled in the following way. The quantum number of the total internal angular momentum of the molecule $\mathbf{f} = \mathbf{F}_1 + \mathbf{F}_2$ is denoted by f . The quantum number of the relative orbital angular momentum of the two atoms forming the molecule l is denoted by l . Feshbach resonances are labelled according to the f and l quantum number of the respective dimer state. Note that molecular states with quantum number l are often referred to as l -wave states and that l is given using spectroscopic notation $l = s, p, d, f, g, h, i, k, l, \dots$ for $l = 0, 1, 2, 3, 4, 5, 6, 7, 8, \dots$ [Rus29].

Feshbach resonances are classified according to the nature of the coupling of the dimer state to the scattering state as outlined in the following section.

2.2.2 Classification of Feshbach resonances

By tuning a molecular closed channel state close to the dissociation threshold one should be able to access the universal regime where the dimer wavefunction is independent of the structural details of the interaction due to its halo structure [Jen04, Köh06]. Two-body universality requires the properties of the dimer state to be fully characterized by a single interaction potential, in our case the entrance channel. In contrast, the divergence of a on resonance is generated by coupling of at least one additional molecular potential. Nevertheless, a range of magnetic field strength representing the universal regime can be associated to every Feshbach resonance. Within this range, usually well within the width of the resonance, a description in terms of a single scattering channel becomes possible, because the dressed molecular state then carries a negligible admixture of the bare molecular state. The range of validity of a single-channel description provides a scheme of classifying magnetically tunable Feshbach resonances. Feshbach resonances accurately describable by a single channel approach even outside the resonance widths are called entrance-channel dominated¹, and in the contrary case they are classified as closed-channel dominated.

The question whether or not a single channel approach is applicable outside the universal regime of magnetic field strengths can be answered by considering the short- and long-range contributions to the molecular state [Köh06]. Mathematically, the criterion for an entrance-channel dominated Feshbach resonance is

$$\eta = \frac{\bar{a}}{a_{bg}} \frac{\hbar^2 / (m\bar{a}^2)}{\mu_{res} \Delta B} \ll 1. \quad (2.6)$$

Here, the so-called Gribakin-Flambaum mean scattering length \bar{a} is a crucial ingredient. \bar{a} gives a characteristic scale of the scattering length. For example, in the toy model of a square well plus hard core interaction potential, \bar{a} recovers the radius of the

¹In the literature also the term ‘open-channel dominated’ is found.

outer well. In the limit of $a \gg \bar{a}$, the energy of the highest lying excited bound state is well approximated by the formula $E_b \approx -\hbar^2/[m(a - \bar{a})^2]$. For alkali interaction potentials, \bar{a} is on the order of the characteristic van-der-Waals length l_{vdW} , and \bar{a} serves as a first order correction to the assumption of a point-like contact potential for alkalis by taking into account the $1/r^6$ -tail of the interaction.

In the opposite limit ($\eta \gg 1$) the Feshbach resonance is said to be closed-channel dominated. The properties of the dressed molecular state associated with such a resonance are not universal and depend on the details of the interaction potential the state lives in.

In practice, closed-channel dominated resonances are narrow, and the universal range of magnetic fields is hard to address. In contrast, entrance-channel dominated resonances are easily controllable and thus make prime candidates for the search for effects in the universal regime $a \gg \ell$.

2.3 The simple picture of Feshbach association

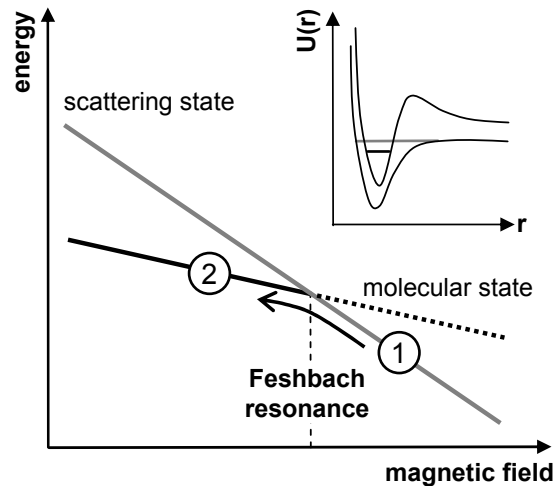


Figure 2.1: Molecule production near a Feshbach resonance. Simplified Zeeman diagram for the atomic scattering state and the molecular bound state. The Feshbach resonance corresponds to the crossing point of atomic and molecular state. Molecules at (2) are created from the atomic BEC at (1) by a downward sweep of the magnetic sweep across the resonance. The inset shows the configuration (2) for the molecular potentials where the molecular state is below the scattering continuum.

Feshbach association of two trapped atoms occupying the trap ground state can be described by a Landau-Zener transition model [Lan32, Zen32]. The molecular bound state and the atomic scattering state form an avoided level crossing [Köh06]. By linearly ramping the magnetic field strength one can coherently transfer the atom pair state into the molecular bound state by adiabatically following the avoided crossing

2.3 The simple picture of Feshbach association

into the region where the bound state exists, given the two atoms are close enough in phase space. Such an association procedure is illustrated in Fig. 2.1. The molecule is termed Feshbach molecule or Feshbach dimer. The transition probability is quantified by a Landau-Zener formula according to $1 - e^{-\varepsilon}$, with $\varepsilon \propto |M|^2 \times \Delta B / (\hbar \dot{B})$ [Köh06]. Here, \dot{B} is the magnetic field ramp speed. Near unity transition probability in the adiabatic limit where $\hbar \dot{B} \ll |M|^2 \Delta B$ has recently been demonstrated experimentally in Ref. [Tha06]. Note that the atom pair state is usually transferred to one of the highest-lying vibrational molecular states. The Feshbach dimer is thus in a highly excited state.

For atomic clouds rather than two atoms the Landau-Zener model remains valid but has to be extended. The figure of interest is the conversion efficiency, defined as the number of atoms transferred to the dimer state divided by the initial atom number. Apart from the transition probability, the conversion efficiency also takes possible loss processes into account. In the adiabatic regime ($e^{-\varepsilon} \ll 1$) the conversion efficiency for a given atomic cloud is closely linked to its initial phase-space density [Hod05]. To be able to form a molecule, the atomic pair has to be sufficiently close in phase space. Intuitively, one would expect an adiabatic passage to smoothly alter the wavefunction describing the atom pair without changing the phase space volume occupied by the pair. Hence, for a condensate where all atoms occupy the same state in phase space, the conversion efficiency must reach unity.

In experiments involving Bose-Einstein condensates, however, the observed conversion efficiencies are much lower than unity and reach no more than 10 % [Her03, Xu03, Dür04a]. This is attributed to loss from atomic two- and three-body decay and to collisional decay of the molecules during the association process. Possible loss processes include

- atom-dimer collisions. During such a collision, the highly excited dimer can decay to more deeply-bound states under release of the binding energy. Considering the prevailing atomic and molecular densities, this is the most severe loss process [Muk04, Smi06, Sya06].
- inelastic higher-order atomic scattering. In the vicinity of the resonance, three-body recombination is dramatically enhanced due to its a^4 scaling, see Sec. 5.2.2 and references therein.
- dimer-dimer collisions. The Feshbach molecules are sufficiently excited to mutually dissociate during a collision. Also, de-exciting collisions under release of binding energy are possible.
- optical pumping. The trapping light, perfectly suitable for atoms, might address molecular optical transitions and thus empty the Feshbach dimer state [Mar05].

The Landau-Zener model and the phase space arguments have been successfully applied to characterize molecule formation from both fermionic and bosonic atoms

[Hod05]. For a review on the production of ultracold molecules via magnetically tunable Feshbach resonances, see Ref. [Köh06].

CHAPTER 3

Review on two-body interactions and dimer states in Cesium

This chapter describes the interactions among two ground state Cs atoms. The two-body bound states unique to Cs and their effect on low energy scattering are introduced. Sec. 3.1 provides an overview of the various interaction mechanisms. In Sec. 3.2 the possible transitions two Cs atoms can undergo during a collision are reviewed. In Sec. 3.3 an overview of the behavior of the molecular states below the scattering continuum of two Cs atoms in the $F = 3, m_F = 3$ hyperfine ground state is given.

3.1 Overview: two-body interactions of cold Cesium atoms

The pair-wise forces of two neutral Cs atoms originate from various interaction mechanisms. The structure of the interaction Hamiltonian is well known, but a quantitative analysis is an intricate affair due to the large nuclear spin [Tie93, Chi01, Chi04a].

Non-relativistic interactions

The most eminent of mutual forces stem from the exchange interaction V_{exc} and the van-der-Waals interaction V_{vdW} . The exchange interaction represents an effective description of all Coulomb forces between two atoms and depends on the magnitude of the total electron spin [Tie93]. Due to the antisymmetry of the total electronic wave function, the exchange term raises (lowers) the energy of the triplet (singlet) potential when the electronic wave functions overlap. This overlap drops exponentially with internuclear distance [Wei85], and so decreases the exchange term, making the van-der-Waals interaction dominant at large distances. V_{vdW} contains a collection of induced electric multipole interactions, all of which are attractive. Of these, the induced dipoles chiefly contribute at large distances, and consequently V_{vdW} scales as $-C_6/r^6$, with r the relative coordinate and C_6 quantifying the van-der-Waals interaction strength.

Relativistic interactions

Other, though much weaker, interactions include relativistic interactions which couple the molecular spin and relative orbital angular momentum degrees of freedom. Here,

dipolar forces are the leading contributors to these couplings. The dipolar interaction $V_{dd} = V_{md} + V_{ss}$ originates from the spin-spin interactions between the two unpaired electrons and consist of a direct magnetic dipole interaction V_{md} , and a second-order spin-orbit contribution, also termed indirect spin-spin coupling V_{ss} . The latter is mediated through electronically excited states and mimics the effect of the direct spin-spin interaction [Tie93]. Both effects have the same spin dependence, but differ in their spatial dependence [Mie96]. The indirect contribution V_{ss} is proportional to the electronic wave function overlap which decreases exponentially with internuclear distance [Wei85], whereas the direct coupling V_{md} falls off as $1/r^3$. They lift the degeneracy of the triplet state projections onto the molecular axis, and hence lead to a coupling of the internal and relative orbital angular momentum degrees of freedom. Note that relative orbital angular momentum in the context of two ground state atoms does not refer to electronic orbits but the relative orbital angular momentum of the two atoms.

3.2 Selection rules for collision-induced transitions

The various interaction mechanisms allow two colliding atoms to change their internal states and their relative orbital angular momentum state. They couple certain molecular states to the two-atom scattering continuum and facilitate Feshbach resonances. The selection rules related to the interactions determine which transitions are allowed.

For two ground state ^{133}Cs atoms in a small magnetic field, each separately described by the usual hyperfine basis states $|F, m_F\rangle$, it is convenient to introduce the total angular momentum $\mathbf{j} = \mathbf{l} + \mathbf{f}$, with \mathbf{l} the relative orbital angular momentum, $\mathbf{f} = \mathbf{F}_1 + \mathbf{F}_2$ the total spin, j , l and f the quantum numbers and m_j , m_l and m_f the respective projection quantum numbers. The magnetic field is small when the energy resulting from the coupling to the external field is small compared to the ground state hyperfine energy splitting. Note that, independent of atomic interactions, j and m_j are good quantum numbers in case of zero field, and only m_j otherwise. Since ^{133}Cs is a boson the total wave function must be symmetric under exchange of atoms. This implies that for an even (odd) value of l , the spin configuration must be symmetric (antisymmetric).

The van-der-Waals interaction does not induce singlet-triplet transitions since it is independent of the electronic spin degree of freedom. The exchange interaction, however, can couple singlet and triplet contributions. As a spherically symmetric interaction, it conserves l and m_l . Since m_j is good quantum number, it follows that the exchange interaction can only induce transitions with the same m_f . In the case of zero magnetic field, both f and m_f are good quantum numbers [Tie93].

The exchange interaction does not couple two Cs atoms in the stretched states $|F = 4, m_F = \pm 4\rangle$ to other internal spin states. Since for stretched states m_F is minimal or maximal, so is the m_f quantum number and no other states with the same m_f are available. Spin-changing collision rates are minimal for stretched rates. In cold Cs gases, this is true also for the $|F = 3, m_F = \pm 3\rangle$ states because the ground state

3.2 Selection rules for collision-induced transitions

hyperfine energy splitting is orders of magnitude larger than typical collision energies.

The dipolar spin-spin interactions V_{dd} couple \mathbf{l} and \mathbf{f} meaning that *all* internal spin states are coupled to some other internal spin states by V_{dd} , even stretched states. Spin-changing collisions due to V_{dd} are called dipolar relaxation. The dipolar interaction V_{dd} of the two electron spins $\mathbf{S}_1, \mathbf{S}_2$ is given by $V_{dd} = V_r(r)[\mathbf{S}_1 \cdot \mathbf{S}_2 - 3(\mathbf{S}_1 \cdot \mathbf{n})(\mathbf{S}_2 \cdot \mathbf{n})]$, with \mathbf{n} the unit vector along the molecule axis and $V_r(r)$ describing the r -dependent part. $V_r(r)$ consists of the two contributions from the direct and the indirect part $V_r(r) = -2\alpha^2 R(a_0^3/r^3 - De^{r/r_d})$, where $\alpha \approx 1/137$ is the fine structure constant, $R \approx 14$ eV is the Rydberg energy, $a_0 = 0.53$ Å is the Bohr radius, $r_d = 0.83 a_0$, and $D = 0.06$ [Chi01]. V_{dd} allows the transfer of up to two units of internal to orbital angular momentum as outlined below.

The derivation of the selection rules related to V_{dd} is described in detail in various quantum mechanics textbooks. The following is intended to briefly outline the mechanism that couples internal and relative orbital angular momentum degrees of freedom by separating V_{dd} into a part acting on \mathbf{l} and one acting on \mathbf{S} . The former will be traced back to spherical harmonic functions Y_{lm} , from which the selection rules follow naturally, whereas the latter will be expressed in terms of the spin flip operators S_+ and S_- together with S_z . The argument closely follows the description of a dipole-dipole coupling given in reference [CT99].

One can rewrite the expression given above in terms of the spin components $S_{(1,2)(x,y,z)}$ with θ and φ the polar angles of \mathbf{n} :

$$V_{dd} = V_r(r)\{3[S_{1z} \cos(\theta) + \sin(\theta)(S_{1x} \cos(\varphi) + S_{1x} \cos(\varphi))] \\ \times [S_{2z} \cos(\theta) + \sin(\theta)(S_{2x} \cos(\varphi) + S_{2x} \cos(\varphi))] - \mathbf{S}_1 \cdot \mathbf{S}_2\},$$

and, using $S_+ = S_x + iS_y$ and $S_- = S_x - iS_y$, one arrives at

$$V_{dd} = V_r(r)\{3[S_{1z} \cos(\theta) + \sin(\theta)(S_{1+}e^{-i\varphi} + S_{1-}e^{i\varphi})/2] \\ \times [S_{2z} \cos(\theta) + \sin(\theta)(S_{2+}e^{-i\varphi} + S_{2-}e^{i\varphi})/2] - (S_{1z}S_{2z} + (S_{1+}S_{2-} + S_{1-}S_{2+})/2)\}.$$

After multiplication and sorting according to the polar coordinates, one gets the following expression

$$V_{dd}/V_r(r) = c_0 Y_{20} S_{1z} S_{2z} + c_{-2} Y_{2-2} S_{1+} S_{2+} + c_2 Y_{22} S_{1-} S_{2-} \\ + c'_0 Y_{20} (S_{1+} S_{2-} + S_{1-} S_{2+}) \\ + c_{-1} Y_{2-1} (S_{1z} S_{2+} + S_{1+} S_{2z}) \\ + c_1 Y_{21} (S_{1z} S_{2-} + S_{1-} S_{2z}).$$

Here, the Y_{2q} are the usual spherical harmonic functions, and the c_n some coefficients of proportionality. From the combinations of the spin operators $S_{(1,2)(z,+,-)}$ it is apparent that only transitions with $|\Delta f| \leq 2$ are allowed. When evaluating the matrix element $\langle l', m_{l'} | V_{dd} | l, m_l \rangle$ between some orbital angular momentum states $|l, m_l\rangle$ and $|l', m_{l'}\rangle$, the

contribution from Y_{2q} will cause a term proportional to

$$\int d\Omega Y_{l'm'}^*(\theta, \varphi) Y_{2q}(\theta, \varphi) Y_{lm}(\theta, \varphi),$$

which is nonzero only for $l' = l, l - 2, l + 2$ with $l \neq 0$ and $l' \neq 0$ and $m_{l'} = m_l + q$, see, e.g., [CT99]. Note that in this context, m_l denotes the quantum number of the projection of l onto the molecular axis, given by the unit vector \mathbf{n} .

In general, for couplings among molecular states and for Feshbach resonances, $\Delta m_j = \Delta(m_l + m_f) = 0$ holds. Coupling matrix elements due to V_{dd} are found to be nonzero only if $0 \leq |\Delta m_f| \leq 2$. In principle, molecular states with an arbitrary l can couple to each other and to the two-atom scattering state. Transitions with $|\Delta l| > 2$ or $|\Delta m_f| > 2$ are of higher order in V_{dd} .

For this thesis the case of two Cs atoms in the $|F = 3, m_F = 3\rangle$ state in the limit of vanishing collision energy at small magnetic field strengths B is relevant. Spin-changing collisions can occur only by dipolar relaxation which is energetically suppressed because a change of the m_F quantum number requires an energy $3\mu_B/4 \times B$, with μ_B Bohr's magneton, the $m_F = 3$ state being the energetically lowest. The selection rules can be applied as follows. The quantum numbers are $m_j = m_l + m_f = 0 + 6 = 6$. Only molecular states with $m_j = 6$ and only molecular l -wave states with even l can lead to Feshbach resonances. Molecular s -wave states are coupled to the atomic scattering state by V_{exc} and V_{vdW} and the coupling strength $|M|^2$ is comparatively large. In contrast, molecular states with $l \neq s$ are coupled by V_{dd} and $|M|^2$ is comparatively weak. Feshbach resonances caused by couplings of first order in V_{dd} are associated with molecular states with $m_f = 4, 5, 6$. Those of higher order in V_{dd} feature $l \geq 2$ or $m_f \leq 3$.

3.3 Cesium molecular energy structure and low energy scattering behavior

In the ultracold limit collision physics is determined by the molecular energy structure of the last, most weakly bound states. The most relevant molecular states for the case of Cs are introduced in this section. It starts with the general picture of the Cs₂ situation just below threshold. It then focusses on details in the magnetic field region up to 150 G which is the maximum magnetic field strength we can generate in the current experimental set-up. The resulting behavior of the scattering length for two Cs atoms in the $F = 3, m_F = 3$ state in that magnetic field region is described.

3.3.1 $l = 0$ Feshbach resonances

An overview of the general behavior of the molecular states below $(F = 3, m_F = 3) \times (F = 3, m_F = 3)$ scattering continuum is given in Fig. 3.1. Weakly bound s -wave states belonging to the $(F_1, F_2, f) = (3, 3, 6)$ channel with vibrational quantum

3.3 Cesium molecular energy structure and low energy scattering behavior

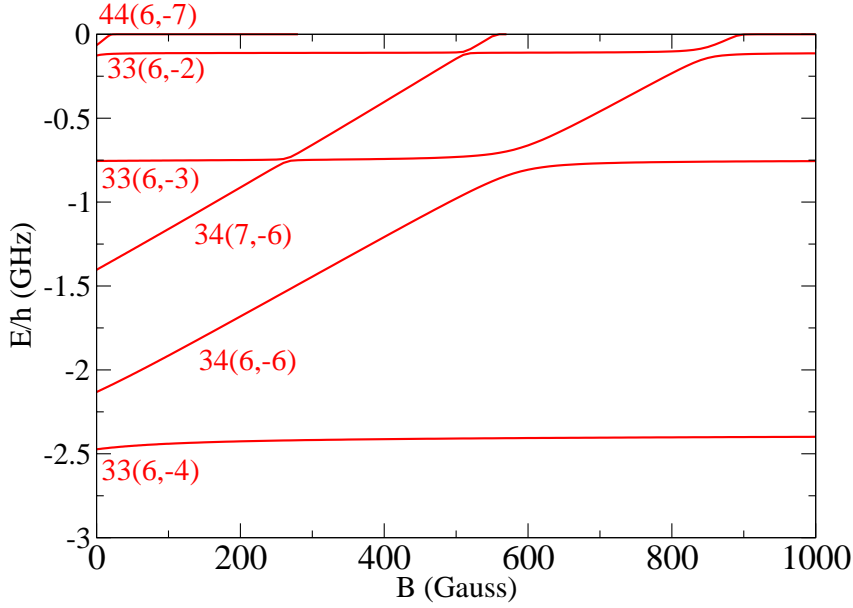


Figure 3.1: Overview of Cs s -wave molecular states. The binding energy of the dimers is plotted as a function of the magnetic field strength. The energy scale is linear, and the threshold energy is given by two Cs atoms in the $F = 3, m_F = 3$ state. The first three of the quantum numbers $F_1 F_2(f, -\nu)$ give the asymptotic (large internuclear distance) Born-Oppenheimer potentials or closed channels the states belong to, with $-\nu$ their vibrational quantum number as counted from threshold at zero magnetic field. The states 34(7,-6) and 34(6,-6) lead to broad Feshbach resonances at 550 G and 850 G. The plot narrowly resolves a weakly bound state labeled 44(6,-7) which turns over at about 20 G into the state 33(6,-1) in the upper left hand corner. This state is not resolved. Its behavior can be seen more clearly in Fig. 3.2. Figure by courtesy of E. Tiesinga, NIST.

numbers $\nu = -2, -3$, and -4 as counted from threshold (horizontal in this plot, labeled 33(6,-2), 33(6,-3) and 33(6,-4)) are intersected by s -wave states from other channels with $(F_1, F_2, f) = (4, 4, 6), (3, 4, 6)$ and $(3, 4, 7)$ (inclined in this plot), leading to strong avoided level crossings. The last bound state 33(6,-1) is so close to the scattering continuum that it is not resolved in this plot. It plays a crucial role for this work. From Fig.3.1 one would expect a Feshbach resonance at about 20 G when the 44(6,-7)-state hits threshold. A strong avoided level crossing with the 33(6,-1)-state shifts the resonance position to -12 G and mainly determines the variation of the scattering length in the magnetic field region of up to 150 G. A similar situation is found at 850 G where one would expect a Feshbach resonance caused by the 34(6,-6)-state. Again an avoided level crossing with the 33(6,-1)-state shifts the resonance position. It is found at 800 G. The 33(6,-1)-state up to 700 G including the situation around 550 G

where the $34(7, -6)$ -state hits threshold are depicted more clearly in Fig. 3.2.

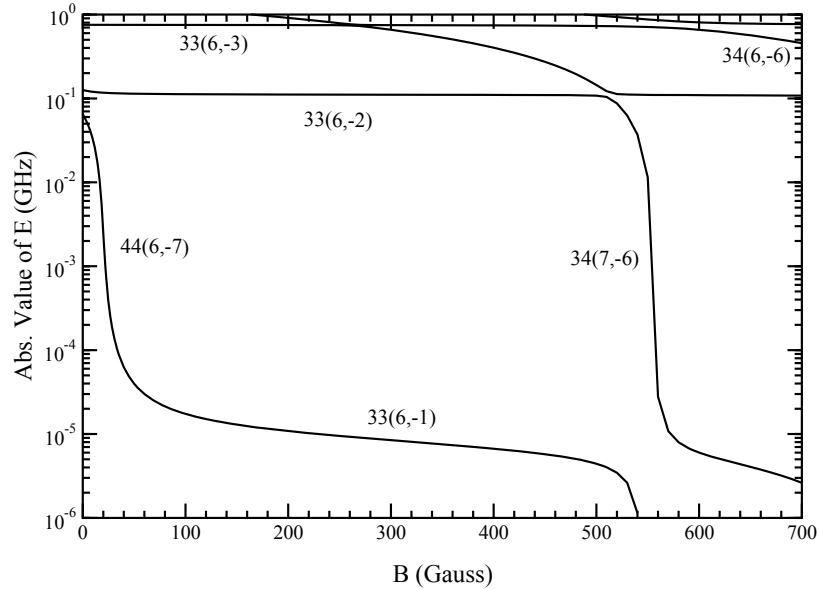


Figure 3.2: The weakly bound molecular s -wave state. The binding energy of dimers is plotted as a function of the magnetic field strength. The energy scale is logarithmic, and the threshold energy is given by two Cs atoms in the $F = 3, m_F = 3$ state. Note that the binding energy is counted positive, i.e. the energy scale is reversed with respect to Fig. 3.1. One can clearly identify the weakly bound $44(6, -7)$ state as it turns over near 20 G into the state $33(6, -1)$ which then remains at a binding energy of about 10 kHz. Beyond 500 G it turns over again as a result of strong avoided crossing with the state $34(7, -6)$, leading to a broad Feshbach resonance at 550 G. The state $33(6, -1)$ is responsible for the unusually large background scattering length of Cs in the $F = 3, m_F = 3$ state. Figure by courtesy of E. Tiesinga, NIST.

A clearer view of the very weakly bound s -wave state is given in Fig. 3.2. Again, the binding energy of dimers is plotted as a function of the magnetic field strength. Now the energy scale is logarithmic, and again the threshold energy is given by two Cs atoms in the $F = 3, m_F = 3$ state. Note that the binding energy is counted positive, i.e. the energy scale is reversed. The crucial level crossing for this work is that of the $44(6, -7)$ state, with a binding energy of 0.07 GHz at zero magnetic field, and the $33(6, -1)$ state. The $44(6, -7)$ state decreases its binding energy with increasing field strength and reaches a binding energy of a few ten kHz at around 20 G. Here, it bends over due to the avoided level crossing with the $33(6, -1)$ -state, which runs parallel to threshold with a binding energy of only about 10 kHz.

Away from any Feshbach resonances, the $33(6, -1)$ -state causes a background scattering length of around $2000 a_0$. It can be regarded as an universal dimer state.

3.3 Cesium molecular energy structure and low energy scattering behavior

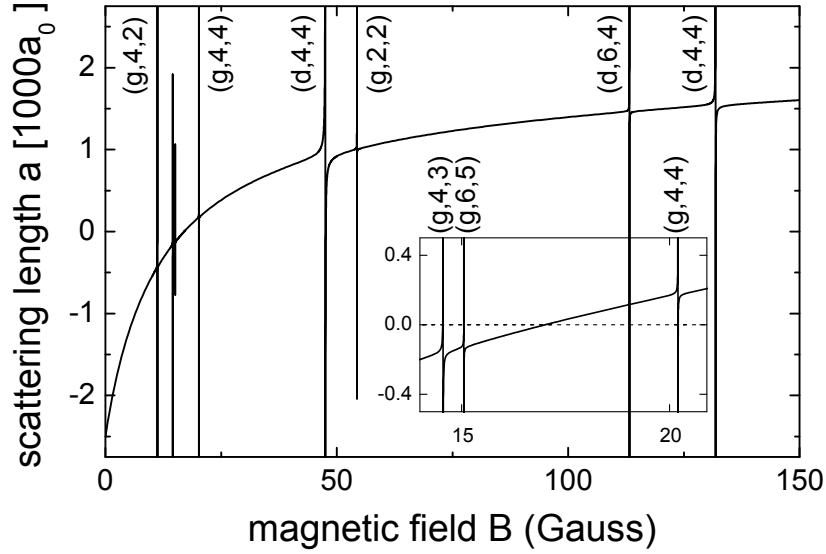


Figure 3.3: Scattering length as a function of magnetic field for the state $F = 3, m_F = 3$. The smooth variation of the scattering length from $-2300 a_0$ at zero Gauss to $1600 a_0$ at 150 G with a zero crossing at 17 G is caused by a universal dimer state. Several narrow Feshbach resonances are visible. The resonance at 48.0 G is caused by coupling to a d -wave molecular state. The very narrow resonances at 11.0, 14.4, 15.0, 19.8 and 53.5 G result from coupling to g -wave molecular states. The inset is a zoom into the region around 17 G where the scattering length crosses zero. The g -wave resonance plotted at 20.1 G is in fact located at 19.8 G [Mar05]. The quantum numbers characterizing the molecular states are indicated here as (l, f, m_f) . Figure courtesy of E. Tiesinga and P. Julienne, NIST.

The avoided level crossing with the $44(6, -7)$ -state leads to a broad open-channel dominated Feshbach resonance at -12 G. This resonance is responsible for a characteristic smooth run of the scattering length in between zero and 150 G. The scattering length as function of magnetic field strength is plotted in Fig. 3.3. It varies between $-2500 a_0$ at zero magnetic field and $1600 a_0$ at 150 G with a zero crossing at 17 G. On top of this smooth variation appear several narrow (closed-channel dominated) Feshbach resonances resulting from couplings to molecular states with large orbital angular momentum which are described in the following section. Disregarding the narrow resonances, the scattering length is well fit by $a(B)/a_0 = (1722 + 1.52 B/G)(1 - 28.72/(B/G + 11.74))$.

Beyond 150 G, the $33(6, -1)$ state couples to the $34(7, -6)$ state around 500 G (see Fig. 3.2) leading to a broad Feshbach resonance at 550 G. The same happens beyond 800 G where $33(6, -1)$ couples to $34(6, -6)$, giving a broad Feshbach resonance at 850 G. These resonances and the resonance at -12 G are mediated by the exchange interaction V_{exc} and the coupling to the atomic scattering state is comparatively strong, featuring resonance widths of several ten Gauss. For magnetic fields up to 1000 G these three resonances are the only clearly open-channel dominated Feshbach resonances avail-

able.

3.3.2 $l \neq 0$ Feshbach resonances

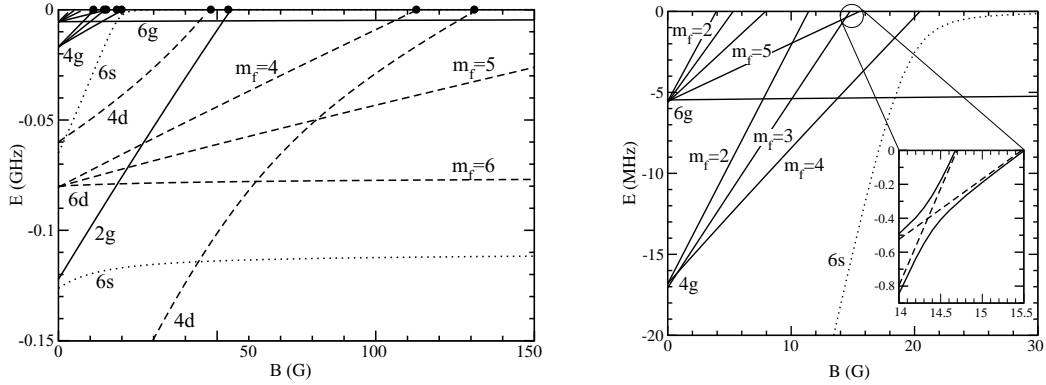


Figure 3.4: Low-field molecular spectrum. The states are labeled according to the f , l and m_f quantum numbers. The left plot covers the range from 0 to 150 G accessed in this work. The right plot is a blow up of the range up to 30 G; note the different energy scales. The inset in the right plot is a magnification of an avoided molecular level crossing at ~ 14.5 G. The $4g, m_f = 4$ state is used in this work for Feshbach association. The plot is adapted from reference [Chi04b].

The narrow Feshbach resonances in Fig. 3.3 are caused by couplings to molecular states with nonzero relative orbital momentum. Thus, they are caused by the comparatively weak magnetic dipole-dipole interactions V_{dd} . The g -wave resonances are clearly in the closed-channel regime ($\eta \gg 1$ in eq. 2.6) whereas for the d -wave resonances $\eta \approx 1$.

The Zeeman diagram of the associated molecular states is shown in Fig. 3.4. Again, the binding energy is given relative to two Cs atoms in the $F = 3, m_F = 3$ state. The labeling of states is according to the f , l and m_f quantum numbers. Note that $m_l = 6 - m_f$. The energy scale is linear, and the binding energy is counted negative. The plot shows the molecular spectrum up to g -wave molecular states together with a more detailed blow-up for low magnetic fields. g -wave molecular states are plotted as solid lines, d -wave states are represented by dashed lines and s -waves by dotted lines. The two $6s$ states visible in the left plot correspond to the $33(6,-2)$ state (running almost parallel with threshold at a binding energy of 0.12 GHz) and the $44(6,-7)$ state in the upper left corner. In the right plot, one readily identifies the $6s$ state which bends over near 20 G from $44(6,-7)$ to $33(6,-1)$ and continues onward just below threshold. The $m_f = 4$ state of the $4g$ manifold is of special relevance for this work because it is used for the association of molecules from a BEC of Cs atoms.

The g -wave resonances are of second order in V_{dd} and show resonance widths of only a few mG, whereas the d -wave resonances, of first order in V_{dd} , are a few 100 mG in width. Fig. 3.4 depicts results from calculations carried out at NIST [Chi04b], based

3.3 Cesium molecular energy structure and low energy scattering behavior

on the experimental determination of the positions of the various Feshbach resonances [Chi04b]. The calculation does not include molecular states with $l > 4$. At least two molecular l -wave states (i.e. $l = 8$) have been detected in the magnetic field region below 50 G [Her05, Mar07a]. Coupling from ultracold atoms in an s -wave scattering state to g -wave or higher orbital angular momentum molecular states is observed only for cesium atoms as a result of the large indirect spin-spin coupling [Mie96].

CHAPTER 4

Experimental set-up and preparation methods

The setting-up of the apparatus started in 2000 with the aim of producing a BEC of Cs atoms. The apparatus is operational since 2002 and has been described in the thesis of Tino Weber [Web03a]. The PhD thesis of Jens Herbig [Her05] focusses on molecule production via Feshbach association which was first achieved in mid 2003 and provides an additional description of the magnetic field generation.

This chapter is meant to acquaint the reader with the main features of the apparatus and focusses on components which are relevant for this work or which have not been described previously.

4.1 Overview: strategy for atomic sample preparation

All our experiments are carried out under ultra-high vacuum conditions to isolate the atoms from the laboratory environment. The typical experimental sequence starts with loading a magneto-optical trap (MOT) [Raa87, Met99] from a Zeeman-slowed diffuse atomic beam [Met99]. Then, the MOT is compressed and a brief phase of molasses cooling [Met99] follows. The pre-cooled atomic cloud is then loaded into a three-dimensional optical lattice for additional Raman-sideband cooling [Ker00]. The Raman-sideband cooling procedure polarizes the sample in the $F = 3, m_F = 3$ state. The atoms, internally now in their absolute ground state, are released from the lattice into a shallow, large-volume far-off resonance optical dipole trap, derived from two crossed CO₂-laser beams. The optical forces are complemented by magnetic forces to counteract gravity. This reservoir trap allows us to collect a large fraction of the laser-cooled atomic sample and thus serves as a starting point for experiments involving Bose-Einstein-condensation [Web03b, Kra04], Feshbach association and molecule trapping [Chi05].

Forced evaporative cooling [Met99] is applied to obtain higher phase-space densities and lower temperatures. We find the reservoir trap unsuitable for evaporation because of the low atomic density [Her05, Web03a]. Instead, a small-volume, far red-detuned optical dipole trap which we call dimple trap is loaded from the reservoir. This second dipole trap is derived from a Yb:YAG fibre laser operating at 1064 nm, and also helped by the magnetic forces. Thus, efficient forced evaporative cooling, all the way to condensation if desired, is achieved. During evaporation the scattering length is magnetically tuned so as to optimize evaporation efficiency.

Following this strategy we routinely produce optically trapped Bose-Einstein condensates (BECs) of up to 2×10^5 Cs atoms. The BEC itself is described in greater detail in Sec. 4.6 of this work, and in references [Web03b, Kra04, Web03a, Her05]. The role of the BEC with regard to this work is twofold. First, it serves as a starting point with as high a phase-space density as possible for all experiments involving Feshbach association. Second, condensation is an essential step in producing thermal samples in the few-nK regime. This second point is explained in Sec. 5.5.

4.2 Vacuum system

The vacuum chamber is basically a sealed steel vessel with a central experimental chamber with as much optical access as possible. It consists of an oven section, the central or main experimental chamber, and pumping sections. A Cs source emits an effusive beam through a differential pumping section into the main experiment chamber. Along the beam path a pressure difference of seven orders of magnitude is established by two differential pumping stages. Two ionization gauges are used to determine the pressure after the first differential pumping stage and in the main chamber. Next to the ionization gauges, all-metal valves allow to connect external turbomolecular pumps, which in conjunction with a roughing pump can bring the main chamber from atmospheric pressure to below 10^{-8} mbar before the standard bakeout procedure. A cross-section of the entire vacuum vessel is shown in Fig. 4.1.

The oven section consists of a stainless steel tube containing two sets of five Cs dispenser rods, each mounted on two current feedthroughs, and a six-way cross used to mount two pumps, an automated beam shutter, a pressure gauge and two valves. Towards the crosspiece the steel tube is closed but for a copper nozzle, allowing the emission of an effusive beam of Cs atoms. The oven is operated at 100° Celsius at a Cs vapor pressure of about 10^{-5} mbar. The first differential pumping stage comprises the oven nozzle and the pumps mounted on the six-way cross the oven is connected to. This first stage sustains a pressure difference of about four orders of magnitude. Under normal operation conditions we measure a pressure of 10^{-9} mbar in the crosspiece.

The Zeeman slower tube, 250 mm in length, connects the oven and the main chamber, and forms the second differential pumping stage, covering three orders of magnitude. The designed maximum capture velocity is 160 m/s. The corresponding magnetic field is generated by four coils which produce a maximum field of 90 G. Having passed through the main chamber, the atomic beam enters an ion getter pump. To insert the Zeeman slowing light opposite the beam direction, a CF40 flange carrying a viewport is welded onto the pump's housing, directly in line-of-sight with the oven nozzle.

All experiments are carried out in the center of the main experimental chamber. Its footprint is a twelve-sided polygon with each edge having a length of 70 mm, its height being 100 mm. Two opposite sides are used to connect the Zeeman slower tube and the main pumping section. In the chamber, a pressure of well below 10^{-11} mbar is

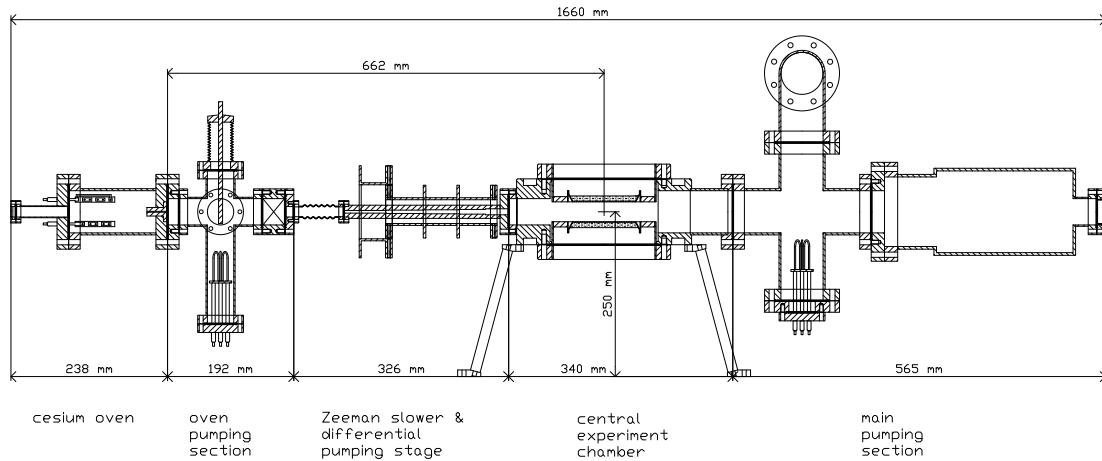


Figure 4.1: Overview of the vacuum system (side view). From left to right: (1) cesium oven with the electrical feedthroughs for the dispenser current, (2) pumping section with beam shutter and titanium sublimation pump, Varian UHV-24p ionization gauge, VAT series 54 all-metal angle valve and Varian Vacion Plus 20 StarCell 20 l/s ion getter pump, (3) VAT series 01 sealed gate valve, (4) differential pumping tube with Zeeman slowing coils, (5) main experimental chamber, (6) main pumping section with titanium sublimation pump, Varian UHV-24p ionization gauge and VAT Series 57 all-metal angle valve, (7) 60 l/s Varian triode ion getter pump with viewport along the axis.

maintained. The other ten sides carry various viewports. Four of these are made of ZnSe, which is transparent for the wavelength of $10.6 \mu\text{m}$ of CO_2 -laser light and anti-reflection (AR) coated for this wavelength. The other viewports are made of quartz glass, AR coated for 850-1050 nm. The top and bottom faces carry CF150 flanges which hold custom-made re-entrant quartz-glass viewports with a diameter of 95 mm and an AR coating for 852-1064 nm. Reaching into the chamber as shown in Fig.4.2, their inner surfaces are spaced 34.1 mm apart. Magnetic field coils are mounted around and on top of the re-entrant quartz windows.

4.3 Magnetic field control

We generate the desired magnetic fields by an assembly of various coils, each serving a different task. We need a quadrupole field for MOT operation, a gradient field for levitation, a homogeneous field for Feshbach tuning and a small offset field to cancel residual stray fields like the earth's magnetic field. Stable and fast control especially over the Feshbach field is of first importance.

A home-made current supply which is described in appendix A feeds the Feshbach field coils and delivers a stable and reproducible current at a relative uncertainty level of a few 10^{-6} . With a bias field of 20 G this allows a resolution of well below 1 mG. There is, however, a magnetic field ripple with an amplitude of 4 mG at 50 Hz present

in our lab that we cannot get rid of. We believe this is caused by the various cooling fans and power supplies in the lab. For a preliminary solution we have referenced the experiment control timing to the power line. Thus, on a timescale shorter than the power line period of 20 ms, the magnetic field stability is indeed limited by the current stability.

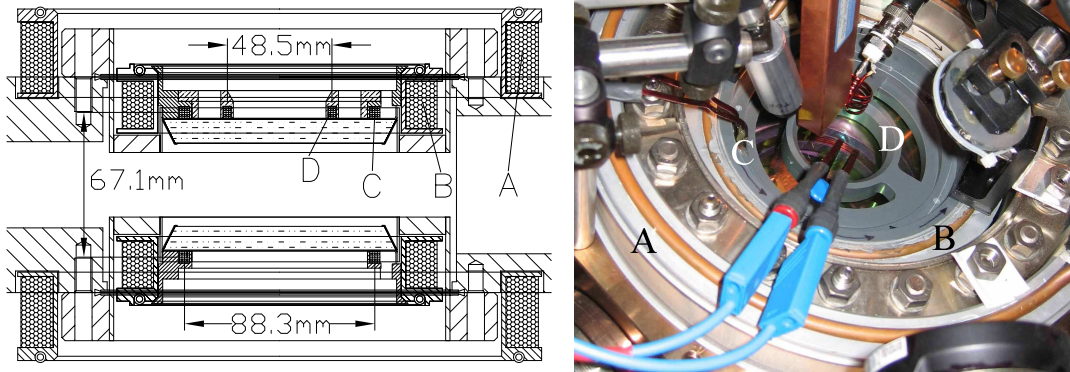


Figure 4.2: Cut through the main chamber (left) and top view (right). (A) The outer coils produce a homogeneous magnetic field. They are only used to produce magnetic field strengths exceeding 60 Gauss. (B) The inner coils consists of several bunches of turns, each individually connected. They serve to generate the levitation quadrupole field and the bias field for tuning the atomic interaction. (A) and (B) are thermally contacted to a water-cooled aluminium housing which acts as a heat dump for the electrical power dissipated in the coils. (C) Additional pair of coils for a faster Helmholtz field. (D) Single coil used to generate μs -steps in the magnetic field. In the picture, the series of nuts belongs to the upper re-entrant viewport. The two water-cooled aluminium housings with copper tubing can be seen. The grey PVC-mounts for the additional fast coils including their supply leads are clearly visible.

The $1/e$ -switching times of all fields generated by the outer coils is limited to a few ms by eddy currents generated within the experiment chamber. To achieve faster decay times for small additional magnetic fields we have placed coils directly to the top and bottom viewport windows. We use mounts made from PVC and set the coils apart from the metallic enclosure. One pair of coils is in roughly Helmholtz configuration, as seen in Fig. 4.2. This pair produces an almost homogeneous field with a $1/e$ -decay time of $300 \mu\text{s}$, thus working comparatively fast. It is powered by a precise and stable home-made supply similar to the one used for the Feshbach coils. For sub- μs switching applications where high precision is not called for, a single coil is situated as close to the viewport center as possible without obstructing optical access. This coil generates a field of up to 6 G at the trap position. After the current feeding this coil is completely switched off, the corresponding magnetic field strength falls to below 1% of its initial value within $1 \mu\text{s}$.

4.4 Optical pre-cooling

In this section the laser system for optical cooling and the performance of the laser cooling procedures we employ are briefly outlined. The pre-cooled atomic cloud described here serves to load the optical traps introduced in the following section.

4.4.1 Laser setup

The laser system for optical cooling relies entirely on laser diodes. In total, we employ six diode lasers to generate the desired light near a wavelength of 852 nm for the D2 line of ^{133}Cs which connects the $6^2\text{S}_{1/2}$ ground state to the $6^2\text{P}_{3/2}$ excited state.

What light do we need? Zeeman slowing and MOT operation require light to drive the cooling transition from the $F = 4$ ground state and simultaneously re-pump from the $F = 3$ ground state [Met99]. Raman-sideband cooling [Ker00, Tre01] requires a 3-dimensional lattice potential, light to drive the Raman-transitions, re-pumping light to empty the $F = 4$ ground state manifold and finally polarizing light which induces cooling and pumps into the lattice dark state. In degenerate Raman-sideband cooling as employed in our setup [Tre01] the first three of these tasks are served by a single laser frequency.

How do we meet these requirements? Our diode lasers can be grouped according to the hyperfine ground state they address.

Lasers addressing the $F = 4$ hyperfine ground state: We use two diode lasers for the MOT and Zeeman-slower cooling light which are referenced via beat-lock to a grating-stabilized master laser, which itself is locked to the $6^2\text{S}_{1/2}, F = 4$ to $6^2\text{P}_{3/2}, F' = 5$ transition using a modulation transfer spectroscopy technique. A third laser diode is injection locked to the master laser. It is resonant with the $F = 4$ to $F' = 4$ transition and used for the production of the optical lattice required for Raman-sideband cooling. Also, it empties the $F = 4$ manifold and induces the necessary Raman-sideband transitions. The imaging light is derived from the master laser. We use acousto-optical modulators (AOMs) to individually shift the light frequencies accordingly.

Lasers addressing the $F = 3$ hyperfine ground state: We use two diode lasers for the re-pumping and polarizing frequencies. They are not referenced to the master laser since the frequency difference between the master laser and the required re-pumping and polarizing frequencies is about 9 GHz. Instead, each is locked separately to a temperature-stabilized Cs absorption cell. The polarizing light for Raman-sideband cooling is derived from the re-pumping light of the Zeeman-slower.

The locking scheme used for the MOT re-pumping laser works over the Doppler-broadened absorption line, thus featuring a linewidth of about 3.5 MHz. The stabilization of all other lasers achieves linewidths of below 300 kHz.

The light is delivered to the experiment by single-mode optical fibres. At the fibre outputs we measure an optical power of around 30 mW each for the MOT and the Zeeman slower cooling light and about 5 mW for the corresponding repumping light.

The Raman lattice laser delivers a good 60 mW in total, and the polarizing light a few hundred μW of optical power.

4.4.2 Performance of laser cooling

We load the MOT from the Zeeman-slowed atomic beam until 3×10^8 atoms have accumulated after 6 s. The ultra-high vacuum of less than 10^{-11} mbar in the main chamber gives 200 s for the $1/e$ -lifetime of the MOT after the atomic beam shutter is closed. We compress the atomic cloud by increasing the gradient by a factor of 5 within 40 ms and simultaneously ramping the detuning of the cooling light from 7 to 30 MHz to the red. We then apply degenerate Raman-sideband cooling to the compressed cloud to further cool and to polarize the atoms in the desired $F = 3, m_F = 3$ ground state. We have adopted the technique as described in reference [Tre01]. The spacing of the relevant energy bands of the optical lattice is on the order of 100 kHz. We apply a small magnetic field of a few hundred mG to induce the Raman-sideband transition. When adiabatically released into free space after a cooling time of 4.5 ms, the cloud comprises up to 3×10^7 atoms and has a temperature of $0.7 \mu\text{K}$.

4.5 Optical dipole traps

The optically pre-cooled atomic cloud of the previous section is loaded into the reservoir trap described here, including the magnetic gradient field used to levitate the atoms. For this work, the reservoir serves two purposes. Firstly, it acts as an intermediate storage for loading the small-volume or dimple trap. This is common to all experiments. The second purpose is to create and trap molecules.

The dimple trap is described in the following section and is used for efficient evaporation, the production of BECs and for trapping the atoms without the magnetic field gradient. Due to the high minimum trap depth required for trapping without levitation, the atomic densities in the dimple trap are rather high ($> 10^{13} \text{ cm}^{-3}$). For trapping without gradient at lower densities, the elliptic trap described in Sec. 4.5.3 is available. In this trap, a CO_2 beam which features a strong focus only in the vertical direction allows to avoid high densities. The elliptic trap and the reservoir cannot be operated simultaneously. Therefore, the elliptic trap is loaded from the dimple trap.

4.5.1 Reservoir trap and levitation

The reservoir trap is generated by the optical dipole potential from two Gaussian CO_2 laser beams and a magnetic gradient field whose force on the Cs atoms exactly cancels the gravitational force. The lasers run freely. The temperature of the laser heads is stabilized to reduce mode-hops and deliver an optical output power of around 100 W each. We horizontally cross these beams at right angles as shown in Fig. 4.3 a. At the crossing point the beams are focused to $1/e^2$ -beam radii of about $650 \mu\text{m}$.

The reservoir trap is completed by applying a magnetic field gradient. We produce this field gradient by combining a quadrupole field and a homogeneous bias field. The required vertical magnetic field gradient for levitation of Cs in the $F = 3, m_F = 3$ state is $\partial B/\partial z = (4/3)mg/\mu_B = 31.3$ G/cm. Since $\text{div}\mathbf{B} = 0$, a corresponding field results in field gradients of $\partial B_x/\partial x = \partial B_y/\partial y = -(2/3)mg/\mu_B$. With a homogeneous bias field oriented along the vertical axis, this combination leads not only to the desired gradient in the vertical direction, but also to a field curvature in the horizontal plane. In essence, this curvature causes an anti-trapping force which depends on the bias field strength B_{bias} . Within the harmonic approximation the anti-trapping effect is best described in terms of the anti-trapping frequency $\alpha = g\sqrt{m/(3\mu_B B_{\text{bias}})} \approx 2\pi \times 3.4$ Hz at $B_{\text{bias}} = 17$ G. This effect reduces the effective trap depth in the horizontal direction. For fields above 20 G, the trap depth is roughly $7 \mu\text{K}$ and the magnetic anti-trapping is barely perceptible. However, below 20 G, this effect becomes dramatic, and already at 10 G the trap depth is reduced by 40 %. The horizontal trap frequencies are reduced by quadratically subtracting α . This is usually a very small effect for all but the lowest trap frequencies. Note that levitation also affects the horizontal motion of free atoms after the optical trap is shut off. The horizontal motion follows $\rho(t) = \rho_0 \cosh(\alpha t) + \alpha^{-1}v_0 \sinh(\alpha t)$ for initial position ρ_0 and initial velocity v_0 . The vertical motion is not affected.

In order to characterize trap properties, we excite vertical trap oscillations by briefly changing the vertical magnetic field gradient and hence tilting the trap. For exciting horizontal trap oscillations we shift the equilibrium position of the atoms by adding a horizontal magnetic field component. In both cases we monitor the center-of-mass oscillation of the atomic cloud after 50 ms time-of-flight. The geometrically averaged measured value of the trap frequency is (13.2 ± 0.2) Hz. It is in good agreement with the calculated value of (12.6 ± 1.5) Hz.

We leave the light of the two CO₂-lasers on during the entire pre-cooling phase for transfer of the pre-cooled atoms into the reservoir trap, because the small light shift introduced by the lasers does not affect the initial loading and cooling efficiency. The reservoir trap is then activated by ramping up the magnetic field and its gradient. We do not expect the transfer to be fully adiabatic due to the finite switching times and an imperfect phase space matching between the pre-cooled cloud and the trap. We find that the atoms are heated to about $2.2 \mu\text{K}$ by the transfer into the reservoir trap.

After 2 s of plain evaporation, the atomic cloud has reached thermal equilibrium. We measure more than 6×10^6 atoms at a temperature of $\sim 1 \mu\text{K}$, corresponding to a peak phase space density of a few 10^{-3} and an atomic number density of a few 10^{11} cm^{-3} . During plain evaporation the bias field is set to $B_{\text{bias}} = 150$ G, corresponding to a scattering length of $\sim 1200 a_0$.

The density and phase space density, however, are difficult to determine accurately, because some weak back reflections of the CO₂-laser beams lead to an undesirable corrugation of the optical potential. By measuring trap depths and apparent trapping frequencies of thermal samples in the nK-regime and of BECs trapped by a single CO₂ laser beam we estimate a corrugation magnitude of roughly 100 nK.

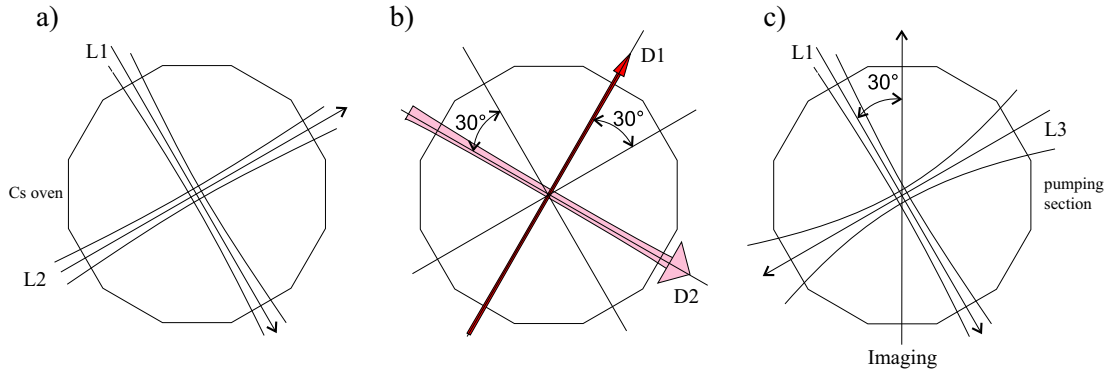


Figure 4.3: Illustration of the laser beams inducing the various optical dipole potentials as seen from above. (a) CO₂ laser beams L1 and L2 forming the reservoir trap. (b) Yb:YAG beams D1 and D2, enabling an efficient evaporation and the production of BECs. (c) L1 and the elliptic, strongly focused CO₂ laser beam L3. In this configuration, the trap can be operated without the magnetic gradient field.

4.5.2 Dimple trap

For forced evaporative cooling [Met99], we load a small-volume far red-detuned optical dipole trap. It is generated by horizontally intersecting one tightly focused laser beam D1 with $34 \mu\text{m}$ waist and another less focused beam D2 with $260 \mu\text{m}$ waist at right angles, rotated by 30° in the horizontal plane with respect to the CO₂-laser beams as shown in Fig. 4.3b. Beams D1 and D2 are derived from a broadband fiber laser operating at 1064 nm. The power in these beams are ramped up within 1.5 s to a maximum power of 130 mW for D1 and 350 mW for D2, causing a small but deep dent in the reservoir potential. Therefore, this small-volume trap is referred to as ‘dimple’ trap. It is populated by elastic collisions. The local deforming of the reservoir leads to a local increase in phase-space density [SK98]. To remove the reservoir we switch off CO₂-laser beam L2 after ramping up the dimple power. The axial confinement is now given by both L1 and D2. The density and phase space density at this point are roughly $2 \times 10^{11} \text{ cm}^{-3}$ and 0.1, respectively. We force evaporative cooling by ramping down the power in all three remaining laser beams while adjusting the scattering length via the bias field. For the attainment of almost pure BECs we eventually reduce the power in CO₂-laser beam L1 to zero, thus adiabatically replacing L1 by the Yb:YAG beam D2. Evaporation and condensate are described in Sec. 4.6.

We use the dimple trap as an intermediate stage to load the elliptic CO₂-laser trap which does not require levitation. In this case, we do not use D2.

4.5.3 Elliptic trap

The elliptic trap consists of reservoir beam L1 and another CO₂-laser beam L3, running in the horizontal plane and perpendicular to L1, see Fig. 4.3c. L3 creates an elliptic

focus of $250 \mu\text{m}$ and $550 \mu\text{m}$ in the vertical and horizontal direction, respectively, at the point of intersection with reservoir beam L1. The resulting elliptic trap can be operated without the levitation field, even though in this case the trap depth is reduced to $2 \mu\text{K}$ as compared to $20 \mu\text{K}$ with gradient. Along the elliptic beam axis we measure a trap frequency of $2\pi \times 11 \text{ Hz}$, in the transverse directions we observe $2\pi \times 21 \text{ Hz}$ horizontally and $2\pi \times 80 \text{ Hz}$ vertically, at a maximum power of 38 W . We produce L3 by an optical path which runs through the zeroth order of the AOM whose first order forms reservoir beam L2. We find it impossible to efficiently load the elliptic trap directly from the reservoir trap. This is due to the variations in beam pointing and shape as the radio-frequency power to the AOM is varied, and possibly also to the corrugation in the reservoir potential. We therefore use the dimple trap as an intermediate storage to load the elliptic trap. The corrugation also prevents an adiabatic re-loading of a BEC from the dimple trap into the reservoir trap.

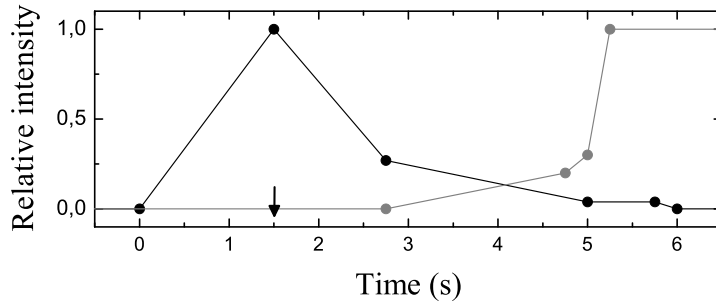


Figure 4.4: A typical ramping procedure used to load the elliptic CO_2 trap. $t = 0$ corresponds to 2 s after loading the reservoir trap. The black and grey lines correspond to the laser intensity in the dimple beam and the elliptic CO_2 beam, respectively. The respective peak powers in the beams are 130 mW and 38 W . The arrow indicates the time when reservoir beam two is switched off.

In Fig. 4.4 we have illustrated a typical loading sequence for the elliptic trap. The attainable maximum trap frequencies in this geometry are insufficient to allow for efficient evaporation. We therefore use our dimple beam for evaporation previous to loading the elliptic trap. The arrow indicates the time when reservoir beam L2 is switched off. By varying the evaporation and loading timings, we achieve different initial temperatures and densities in the elliptic trap. Typical particle numbers and temperatures range from 10^4 to 10^6 and from below 100 to 700 nK , respectively. The densities vary from 10^{12} to 10^{13} cm^{-3} . We turn off the gradient within 180 ms without exciting trap motion or otherwise heating the trap.

Originally this trap was intended for trapping of Cs_2 dimers without the need for a magnetic gradient field. This is not possible with the broadband Yb:YAG laser light because of optical pumping from the ground state potential to somewhere within the electronically excited molecular $S + P$ potential. Within the context of this thesis it serves as a non-levitation container featuring atomic number densities well below 10^{13} cm^{-3} and is used for three-body loss measurements.

4.6 Bose-Einstein condensation of Cesium atoms

The starting point for forced evaporation and condensate production are up to 1×10^6 Cs atoms in the dimple trap. As described in Sec. 4.5.3 and illustrated in Fig. 4.3, the dimple trap is formed by the two crossed Yb:YAG laser beams D1 and D2. Efficient forced evaporation is achieved by ramping down the power in D1 and D2, initially at 130 mW and 350 mW, respectively. This corresponds to a trap depth of a few μK . For D1 we approximately follow an exponential ramp over 5.5 s, whereas we linearly decrease the power in D2 by 20 %. The final power in D1 and D2 is 0.5 mW and 280 mW. We find that a magnetic field value of 21 G with scattering length $a = 210 a_0$ is optimal during the forced evaporation phase. This value appears optimal because it combines high elastic scattering rates with unusually low three-body losses. As can be seen from Fig. 4.5 the evaporation efficiency lies around 3 during the forced evaporation ramp. The evaporation efficiency is commonly defined as the orders of magnitude gained in phase space divided by the orders of magnitude lost in atom number for a given evaporation step. We attribute this high efficiency to the fact that atoms can escape the trap into almost all directions as a result of levitation.

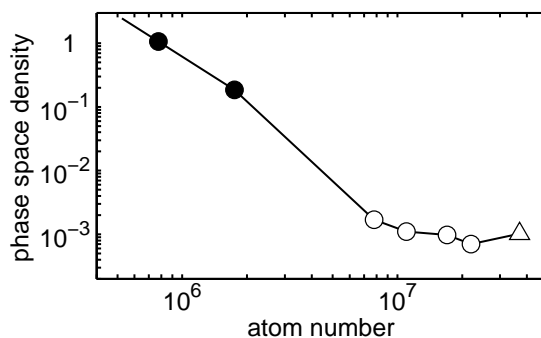


Figure 4.5: Peak phase space density as function of atom number. The path of evaporation proceeds from right to left. The triangle shows the atomic ensemble immediately after lattice cooling. The open circles show the ensemble in the reservoir trap after 0.08, 0.22, 0.64, and 2.0 s. The filled circles correspond to the sample in dimple trap right after loading and at 1.5 s after starting the evaporation ramp. The phase transition occurs 2 s after starting forced evaporation with $\sim 5 \times 10^5$ atoms left in the dimple trap.

The phase transition occurs 2 s after starting the forced evaporation ramp. At this point, the temperature is around 200 nK and 5×10^5 atoms are in the trap. The atom loss from forced evaporation corresponds to half the atom number initially loaded into the dimple trap.

At the end of the evaporation ramp, we measure $2\pi \times 21$ Hz and 4.5 Hz for the radial (transverse directions of D1) and axial (along D1) trap frequencies, respectively. At this point, the BEC is almost pure and contains 2×10^5 atoms. In good agreement with theory, we measure a chemical potential [Pet02] of 14 nK. We infer for the Thomas-Fermi radii [Pet02] in the radial and axial directions $9 \mu\text{m}$ and $43 \mu\text{m}$, respectively.

4.7 Diagnostics

We measure the spatial density distribution of our samples by absorption imaging. When illuminated by resonant light, the cloud casts a shadow which is mapped onto a CCD chip by a lens system. This method is a standard technique quite commonly used in cold atom experiments [Ket99].

We use linearly polarized light resonant on the $6^2S_{1/2}, F = 4$ to $6^2P_{3/2}, F' = 5$ transition. We turn on the MOT repumper 500 μs before the imaging cycle to pump all atoms into the $F = 4$ hyperfine state and then keep it on during the typically 200 μs absorption pulse.

The imaging beam traverses the chamber in the horizontal plane and crosses the atomic beam line at 90° , see Fig. 4.3c. In the camera frame, we call the horizontal direction x and the vertical direction y . The imaging beam propagation direction is then z . The beam is linearly polarized in the x -direction. The unperturbed beam intensity profile $I_0(x, y)$ is attenuated by the atoms according to $I(x, y) = I_0(x, y)e^{-\sigma_{exp}n_z(x, y)}$. The attenuation depends on the atomic column density $n_z(x, y)$, which is the atomic number density integrated along the z -direction, and the absorption cross section σ_{exp} . σ_{exp} depends on the intensity and the detuning of the imaging beam, the atomic transition linewidth and, finally, the resonant absorption cross section σ of the atomic transition. For a measurement, two images are taken, with and without the atoms, corresponding to $I(x, y)$ and $I_0(x, y)$, respectively. From these, the column density can be readily determined once the parameters of the imaging light, the CCD pixel size and the atomic transition properties are known. The procedure is described in detail in [Web03a].

Imaging at small magnetic fields

The atomic absorption cross section σ for zero field is calculated based on the closed-transition cross section of the D2 line $\sigma_0 = 3\lambda^2/2\pi$, with $\lambda = 852$ nm. To calculate σ , we compare the strengths of the $F = 4, m_F \rightarrow F' = 5, m_{F'}$ transitions to the $F = 4, m_F = 4 \rightarrow F' = 5, m_{F'} = 5$ transition strength. Since the latter can be regarded as a true two-level system, σ is then obtained by multiplying the average relative transition strength by σ_0 . This results in $\sigma = 0.407\sigma_0 = 1.41 \times 10^{-9}\text{cm}^2$, and we use this value in all further calculations.

For imaging at non-zero magnetic bias fields B_{bias} of up to 50 G, we detune the imaging light by $+\mu_B B_{\text{bias}}$ to the blue. In doing so we compensate for the magnetic field shift of the $F = 4, m_F = 4$ to $F' = 5, m_{F'} = 5$ cycling transition. The imaging beam runs perpendicular to the quantization axis given by the magnetic field. Also, the polarization axis is perpendicular with respect to the magnetic field direction. The absorption cross section $\sigma_{\text{B-field}}$ of such a scenario is derived in reference [Geh03] as part of a treatment of the more general case of an arbitrary angle between the imaging beam and the quantization axis. For our setup, the absorption cross section is given by $\sigma_{\text{B-field}} = \sigma_0/2$. Thus, the apparent atom number obtained at non-zero magnetic field $N_{\text{B-field}}$ differs from the actual atom number N as $N_{\text{B-field}} = 0.814N$. We measure a

factor of 0.77(6), which agrees reasonably well with the calculation, considering that we do not detune the re-pumping light. The re-pumper bears a detuning of about 10 linewidths to the red at a magnetic field strength of 50 G. At non-zero magnetic field, re-pumping precedes imaging by 1 ms. This time appears sufficient to transfer the atoms into the $F = 4, m_F = 4$ state prior to the imaging pulse.

CHAPTER 5

Three-body interactions: Measurements of three-body recombination and evidence for Efimov quantum states

The classical three-body problem in the form of its paradigm example earth-moon-sun has been around since earliest times. Solutions to the equations of motion for three interacting particles can be found only within certain limits. Up until now even the orbit of the moon is not completely understood [Gut98]. The quantum mechanical version of the three-body problem with pairwise interaction is encountered in all sub-fields of physics [Nie01] and like its classical counterpart it is in general considered unsolved. In the special case of short-ranged two-body interactions solutions exist if the two-body interaction is ‘sufficiently resonant’. The existence of these solutions is known as the Efimov effect.

At low collision energies, when the inverse scattering vector of the particles is larger than the characteristic range of interaction ℓ , two-body physics is largely determined by the s-wave scattering length a . Universal properties of the two-body system are encountered in the regime where $|a| \gg \ell$. An example of a universal property is the existence of a two-body bound state with a binding energy proportional to a^{-2} for positive and large scattering lengths $a \gg \ell$. The corresponding dimer wavefunction is independent of the particular nature of the forces acting between the atoms and is in this sense universal. It assumes a universal shape [Köh06] which supports little probability amplitude in the interaction region and concentrates its weight outside that region. The universal dimer state therefore belongs to the class of quantum halo states [Jen04]. Efimov proved that a three-particle system also features universal properties when $|a| \gg \ell$. In particular, he proposed the existence of an infinite series of arbitrarily weakly bound three-body states, now called Efimov states, appearing in the limit when the scattering length approaches infinity for two or three binary subsystems [Efi70, Efi71]. The corresponding Efimov state wavefunction assumes a universal shape and also belongs to the class of quantum halo states [Jen04, Bra06]. The occurrence of a whole series of these states reflects a universal scaling symmetry in three-body systems with large scattering length [Bra06].

Efimov trimers dramatically alter the low-energy scattering cross sections for collisions between three atoms, between dimers and atoms [Efi79], and possibly also between dimers and dimers in the vicinity of the respective dissociation thresholds. Since the theoretical proposal of their existence, Efimov states have been eluding experimental attempts at a direct detection and they continue to do so. Within the frame of this thesis, their fingerprint in collisions involving three Cs atoms has been found

[Kra06]. This is the first instant of experimental evidence for effects related to Efimov states. We make the presence of Efimov states visible by observing three-atom inelastic trap loss while tuning the binary interaction strength via a suitable Feshbach resonance resulting from a universal dimer state. The presence of an Efimov state is then revealed in a giant loss resonance for negative scattering lengths and a suppression of three-body loss for positive scattering lengths.

This chapter is divided in five sections. In Sec. 5.1, the string of arguments leading to the theoretical proposal of Efimov states will be reviewed. Sec. 5.2 relates Efimov states to ultracold atomic and molecular gases. Sec. 5.3 is devoted to the experimental accessibility of the universal regime in our setup. Sec. 5.4 presents the relevant experimental data, and Sec. 5.5 provides the details of the measurement analysis and the error budget.

5.1 Efimov effect

In 1935 L.H. Thomas predicted that a three-body bound state, now called Thomas trimer, exists in a system of spinless particles when the two-body interaction supports a single virtual or bound two-body state at the dissociation threshold [Tho35]. The Thomas trimer is the ground state of the three-body system and its size is given by the characteristic range of the binary interaction ℓ , and its binding energy becomes infinitely large in the limit of $\ell \rightarrow 0$. As a generalization to Thomas's effect, Efimov's effect occurs in the universal realm where $|a| \gg \ell$. In short Efimov's effect is based on the fact that three particles interacting via short-ranged two-body potentials see an attracting effective three-body potential which falls off as the inverse square of the mean inter-particle distance R for $R \gg \ell$. In the limit of infinite scattering length $|a| \rightarrow \infty$ this effective three-body potential supports an infinite number of three-body bound states, called Efimov trimers. For large but finite values of $|a|$ the effective three-body potential is cut off at $R \approx a$ and supports only a finite number of Efimov trimers.

This section first reviews the relevant three-body scattering formalism. The so-called Lippman-Schwinger equation formally describes the two-body potential scattering problem for the two-body case [Sit91, Joa75]. In the three-body realm scattering is adequately described by the so-called Faddeev set of equations [Fad61, Fad65]. In Sec. 5.1.2 coordinate-space Faddeev equations [Fed93] using hyperspherical coordinates are introduced. Their solution leads to so-called channel potentials for R of which only the energetically lowest is attractive [Fed93, Bra06, Nie01]. Sec. 5.1.3 then discusses the Efimov effect [Efi70, Efi71] and gives emphasis on the case of large but finite scattering lengths. In Sec. 5.1.4 an illustration of the universal dimer and Efimov states in the vicinity of a zero-energy resonance is given. This illustration is known as Efimov's scenario [Efi71, Efi79]. Sec. 5.1.5 reviews the search for Efimov-related effects and Efimov states up to now.

5.1.1 Three-body scattering formalism

In the stationary formulation the scattering problem is given by the Schrödinger equation $(E - H_0 - V)\Psi = 0$. Here, H_0 describes the non-interacting part of the Hamiltonian, V is the interaction vanishing at sufficiently large interparticle distance \mathbf{r} , and E is the collision energy. For $\mathbf{r} \rightarrow \infty$, the solution Ψ must be the sum of an incident wave Φ , satisfying $(E - H_0)\Phi = 0$, and an outgoing scattered wave.

The Lippman-Schwinger equation for the two-body case

For two-body potential scattering the formal solution for the center-of-mass frame is known as the Lippman-Schwinger equation which is described in detail in various textbooks. The description given here loosely follows Ref. [Joa75] and Ref. [Sit91]. In symbolic form it is given by $\Psi_k = \Phi_k + G_0 V \Psi_k$. Here, G_0 is the Green operator belonging to H_0 . Note that G_0 satisfies the inhomogeneous equation $(E - H_0)G_0 = \delta$ with δ a point-like inhomogeneity. In a time-independent picture $\psi_k(\mathbf{r}) = \langle \Psi_k | \mathbf{r} \rangle$ is the scattering state wave function and $\phi_k(\mathbf{r}) = \langle \Phi_k | \mathbf{r} \rangle$ denotes an incoming plane wave with wave vector \mathbf{k} , which is related to the collision energy $E = \hbar^2 k^2 / 2\mu$, with μ the reduced mass. In coordinate space representation the Green function $G_0(E, \mathbf{r}, \mathbf{r}')$ is obtained by expanding G_0 in terms of the coordinate space eigenfunctions of H_0 , resulting in $G_0(E, \mathbf{r}, \mathbf{r}') = \langle \mathbf{r}' | G_0(E) | \mathbf{r} \rangle$. This leads to the integral formulation of the Lippman-Schwinger equation $\psi_k(\mathbf{r}) = (2\pi)^{-3/2} e^{i\mathbf{k}\mathbf{r}} + \frac{2m}{\hbar^2} \int d\mathbf{r}' G_0(\mathbf{r}, \mathbf{r}') V(\mathbf{r}') \psi_k(\mathbf{r}')$. The boundary condition of an outgoing spherical wave for large \mathbf{r} is satisfied by an appropriate choice of the Green function.

Having evaluated the Green function $G_0(E, \mathbf{r}, \mathbf{r}')$ the integral $\int d\mathbf{r}' G_0(\mathbf{r}, \mathbf{r}') V(\mathbf{r}') \psi_k(\mathbf{r}')$ takes on the form of a spherical wave at large \mathbf{r} , and its amplitude is proportional to $T_{\text{fi}} = \langle \phi_{\mathbf{k}_f} | V | \psi_{\mathbf{k}_i} \rangle$, depending on the initial and final wave vectors \mathbf{k}_i and \mathbf{k}_f , respectively. T is called the transition operator, with T_{fi} its matrix elements. T_{fi} is proportional to the scattering amplitude, and $|T_{\text{fi}}|^2$ is proportional to the differential scattering cross section. In symbolic form, $T = V + V G_0 T$, as can be seen from the definition of T_{fi} by inserting the Lippman-Schwinger equation for $\psi_{\mathbf{k}_i}$. The transition operator will come in handy when introducing the Faddeev equations in the following section.

The three-body case

The Lippman-Schwinger equation in the two-body realm is a mathematically well-behaved integral equation with a unique solution for $E > 0$. For three interacting particles, however, this is not the case. Firstly, the kernel $G_0 V$ is not square integrable and cannot be made so, meaning that possible solutions are un-physical. The reason for this behavior lies in so called disconnected configurations where two particles interact while the third particle remains unaffected. Secondly, solutions to the Lippman-Schwinger equation are not unique in the three-body realm. This is due to the possibility of rearrangement or reactive scattering where in a two-particle compound

one constituent is being replaced by the third particle during collision. A detailed and in-depth analysis of these properties may be found in various text books, see e.g. Ref. [Joa75, Sit91].

It was Faddeev who resolved these difficulties [Fad61]. His idea is to split the total interaction V into three two-body components such that $\tilde{V}(\mathbf{r}_1, \mathbf{r}_2, \mathbf{r}_3) = V_{12} + V_{23} + V_{31}$, where $V_{ij} \equiv V(\mathbf{r}_i, \mathbf{r}_j)$ are the two-body potentials of particles i and j at \mathbf{r}_i and \mathbf{r}_j . Thus the potential \tilde{V} is assumed to be separable and to have a negligible genuine three-body component, which is appropriate for atomic collisions at low energy. Including a genuine three-body interaction comes with greater formality but no effect on Faddeev's arguments [Nie01]. The crucial feature of this decomposition into two-body forces is that each of the Lippman-Schwinger equations for the respective two-body components contain all disconnected configurations. This facilitates their exclusion from the problem by algebraic manipulations, which result in the so called Faddeev equations.

One can choose to formulate the three-body scattering problem in terms of Green functions, transition matrices and wave functions. For each such description a set of Faddeev equations can be derived. The following illustration of Faddeev's arguments is given in terms of the three-body transition operator \tilde{T} and based on the three-body scattering chapters in Ref. [Joa75] and in Ref. [Sit91]. The set of Faddeev equations for the three-body scattering wave function $\tilde{\Psi}$ takes on the form $\tilde{\Psi} = \Psi^{(1)} + \Psi^{(2)} + \Psi^{(3)}$ and reads

$$(H_0 - E)\Psi^{(i)} + V_{jk}\tilde{\Psi} = 0, \quad ijk = 123, 231, 312. \quad (5.1)$$

If $\Psi^{(1)}, \Psi^{(2)}$ and $\Psi^{(3)}$ are solutions to the Faddeev equations, then $\tilde{\Psi}$ is a solution to the three-body Lippman-Schwinger and in consequence also to the three-body Schrödinger equation.

Due to the decomposition of \tilde{V} into the binary potentials V_{ij} , \tilde{T} can be written as $\tilde{T} = T^{(1)} + T^{(2)} + T^{(3)}$, with the $T^{(k)}$ defined as

$$T^{(k)} = V_{ij} + V_{ij}G_0\tilde{T}, \quad ijk = 123, 231, 312. \quad (5.2)$$

We can replace \tilde{T} on the right hand side by its individual terms. By iterating $T^{(k)}$ once in the above equation, one will obtain

$$T^{(k)} = V_{ij} + V_{ij}G_0(V_{ij} + V_{ij}G_0)(T^{(i)} + T^{(j)} + T^{(k)}). \quad (5.3)$$

The disconnected configurations are represented by $V_{ij}G_0V_{ij}G_0T^{(k)}$ and render the solutions un-physical by introducing a delta function due to momentum conservation of the third, uninvolved particle. These terms can be avoided if $T^{(k)}$ does not appear on the right-hand side of Eq. (5.3):

$$\begin{aligned} [1 - V_{ij}G_0]T^{(k)} &= V_{ij} + V_{ij}G_0[T^{(i)} + T^{(j)}] \text{ and hence} \\ T^{(k)} &= [1 - V_{ij}G_0]^{-1}V_{ij} + [1 - V_{ij}G_0]^{-1}V_{ij}G_0[T^{(i)} + T^{(j)}]. \end{aligned} \quad (5.4)$$

Note that for the two-body subsystems the transition operators are given by

$$T_{ij} = V_{ij} + V_{ij}G_0T_{ij}, \quad (5.5)$$

where the $V_{ij}G_0T_{ij}$ introduce the disconnected configurations when transferred to the three-body case. Suppose the T_{ij} were known. Eq. (5.5) then serves to evaluate the binary operator $[1 - V_{ij}G_0]^{-1}$ in Eq. (5.4). From Eq. (5.5) it follows that $V_{ij} = [1 - V_{ij}G_0]T_{ij}$ and hence $[1 - V_{ij}G_0]^{-1}V_{ij} = T_{ij}$. Thus, one can rewrite (5.4) for the individual terms of the transition operator as

$$T^{(k)} = T_{ij} + T_{ij}G_0[T^{(i)} + T^{(j)}]. \quad (5.6)$$

Using the more convenient notation $T_k \equiv T_{ij}$ another way of writing Eq. (5.6) is

$$\begin{pmatrix} T^{(1)} \\ T^{(2)} \\ T^{(3)} \end{pmatrix} = \begin{pmatrix} T_1 \\ T_2 \\ T_3 \end{pmatrix} + \begin{pmatrix} 0 & T_1 & T_1 \\ T_2 & 0 & T_2 \\ T_3 & T_3 & 0 \end{pmatrix} G_0 \begin{pmatrix} T^{(1)} \\ T^{(2)} \\ T^{(3)} \end{pmatrix}. \quad (5.7)$$

The 3×3 matrix multiplied from the right by G_0 is called the Faddeev kernel K . The two-body T -operators appearing in K now cause the disconnected configurations. However only the off-diagonal parts of K contain disconnected parts meaning that any iteration of K will produce connected parts. Iterating once gives

$$\begin{pmatrix} T^{(1)} \\ T^{(2)} \\ T^{(3)} \end{pmatrix} = \begin{pmatrix} T_1 \\ T_2 \\ T_3 \end{pmatrix} + K \begin{pmatrix} T_1 \\ T_2 \\ T_3 \end{pmatrix} + K^2 \begin{pmatrix} T^{(1)} \\ T^{(2)} \\ T^{(3)} \end{pmatrix} \quad (5.8)$$

with

$$K^2 = \begin{pmatrix} T_1G_0T_2 + T_1G_0T_3 & T_1G_0T_3 & T_1G_0T_2 \\ T_2G_0T_3 & T_2G_0T_1 + T_2G_0T_3 & T_2G_0T_1 \\ T_3G_0T_2 & T_3G_0T_1 & T_3G_0T_1 + T_3G_0T_2 \end{pmatrix} G_0. \quad (5.9)$$

In contrast to (5.2), this system of interconnected operator equations has a single valued solution [Fad61, Fad65] and contains no disconnected configurations.

5.1.2 Jacobian coordinates and decomposition at low energy

In coordinate space representation one usually employs Jacobi or hyperspherical coordinates. As an example, one of three possible sets of Jacobi coordinates is illustrated in Fig. 5.1. Here, $\mathbf{r}_{ij} = \mathbf{r}_i - \mathbf{r}_j$ and $\mathbf{r}_{k,ij} = \mathbf{r}_k - \frac{1}{2}(\mathbf{r}_i + \mathbf{r}_j)$ for particles with equal mass and (i, j, k) being cyclic permutations of $(1, 2, 3)$. The hyperradius R is defined by $R^2 = \frac{1}{3}(r_{12}^2 + r_{23}^2 + r_{31}^2) = \frac{1}{2}r_{ij}^2 + \frac{1}{3}r_{k,ij}^2$ and the five hyperangles α_k are $\alpha_k = \arctan(\sqrt{3}r_{ij}/2r_{k,ij})$. The meaning of the indices is illustrated in Fig. 5.1 for $(i, j, k) = (1, 2, 3)$. Jacobi coordinates are a convenient choice in describing the three two-body subsystems in the Faddeev equations for the three-body wavefunction in coordinate space representation. The structure of the Faddeev equations for the three-body wavefunction is given in Eq. 5.1. In coordinate space representation the three-body wavefunction is determined by [Fed93, Bra06]

$$(T_R + T_{\alpha_i} + \Lambda_{i,jk}^2/(2mR^2))\Psi^{(i)} + V(r_{jk})(\Psi^{(i)} + \Psi^{(j)} + \Psi^{(k)}) = E\Psi^{(i)}.$$

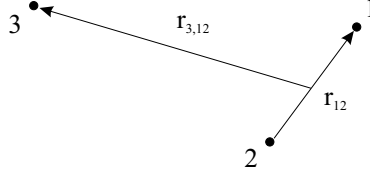


Figure 5.1: Jacobi coordinates. One out of three possible coordinate sets.

T_R and T_{α_i} denote the kinetic energy operators associated with the hyperradius and the hyperangles, respectively. $\Lambda_{i,jk}^2$ is the total angular momentum of the subsystems ij and k, ij composed of the sum of the angular momentum operators with respect to \mathbf{r}_{ij} and $\mathbf{r}_{k,ij}$. Note that in the center-of-mass system six coordinates are required to describe the system.

The Faddeev equations are reduced from six to four variables by ignoring subsystem angular momentum, i.e. by setting $\Lambda_{i,jk}^2 = 0$. This assumption has no effect on the general formalism, but avoids a decomposition of $\Psi^{(i)}$ into spherical harmonics. It is motivated by the general suppression of higher orbital angular momentum components at low energies. A further simplification can be achieved by rotating the wavefunctions defined in the other two frames into the one we choose to work with. This rotation expresses one set of coordinates by another and subsequently averages over the angular variables of the chosen working frame [Fed93]. The averages are the same for both the rotated frames. Thus, the Faddeev equations can be reduced to a single integro-differential equation depending only on the hyperradius and one hyperangle

$$(T_R + T_\alpha - E) \psi(R, \alpha) + V(\sqrt{2}R \sin \alpha) \times \left(\psi(R, \alpha) + \frac{4}{\sqrt{3}} \int_{|\pi/3-\alpha|}^{\pi/2-|\pi/6-\alpha|} d\alpha' \frac{\sin(2\alpha')}{\sin(2\alpha)} \psi(R, \alpha') \right) = 0,$$

where the integral on the right hand side is the result of the rotation of the other two frames.

One popular method of solving this equation employs the expansion of the wave function ψ in a complete set of hyperangular functions ϕ_n ,

$$\psi(R, \alpha) = \frac{1}{R^{5/2} \sin 2\alpha} \sum_n f_n(R) \phi_n(R, \alpha). \quad (5.10)$$

The ϕ_n are the eigenfunctions of the α -dependent part of the Faddeev equation

$$-\frac{\partial^2 \phi_n(R, \alpha)}{\partial \alpha^2} + \frac{2mR^2}{\hbar^2} V(\sqrt{2}R \sin \alpha) \times \left(\phi_n(R, \alpha) + \frac{4}{\sqrt{3}} \int_{|\pi/3-\alpha|}^{\pi/2-|\pi/6-\alpha|} d\alpha' \phi_n(R, \alpha') \right) = \lambda_n(R) \phi_n(R, \alpha),$$

with $\lambda_n(R)$ the corresponding eigenvalues. In solving this equation, the hyperradius R is treated as a parameter. The pre-factor $1/(R^{5/2} \sin 2\alpha)$ to the hyperangular functions ϕ_n in (5.10) is for normalization only and cancels with corresponding terms from the T_R and T_α operator.

The hyperradial wave functions $f_n(R)$ in (5.10) are solutions to a coupled set of radial differential equations. The dimensionless eigenvalues $\lambda_n(R)$ define so-called channel potentials for the $f_n(R)$ which are described in greater detail in the following section. The convergence of the sum in (5.10) with respect to $f_n(R)\phi_n$ is very fast, and already $f_0(R)\phi_0(R, \alpha)$ gives a good approximation [Fed93]. Inserting expansion (5.10) into the Faddeev equation, projecting onto $\phi_n^*(R, \alpha)$ and taking only the diagonal part leads to a set of eigenvalue equations for the hyperradial wave functions $f_n(R)$

$$\frac{\hbar^2}{2m} \left(-\frac{\partial^2}{\partial R^2} + \frac{\lambda_n(R) - 1/4}{R^2} \right) f_n(R) = E f_n(R). \quad (5.11)$$

Here, in taking only the diagonal part coupling terms of the form $\langle \phi | \frac{\partial}{\partial R} | \phi \rangle$ and $\langle \phi | \frac{\partial^2}{\partial R^2} | \phi \rangle$ have been neglected. The omission of these coupling potentials is called the adiabatic hyperspherical approximation and is justified when the $\lambda_n(R)$ vary sufficiently slowly with R . In general, the adiabatic hyperspherical approximation becomes better with large R [Fed93, Bra06]. Note that Eq. (5.11) supports a hyperradial potential $V(R) = \hbar^2(\lambda_n(R) - 1/4)/(2mR^2)$ falling off as $1/R^2$ which is attractive or repulsive depending on the value of $\lambda_n(R)$.

5.1.3 Hyperspherical channel potentials and Efimov effect

The assumptions about the total interaction so far are that it can be split into two-body potentials for each pair of atoms and a possible three-body component is negligible. We now assume that the two-body interaction potential falls off faster than the inverse square of the distance. Thus, a length ℓ can be defined which gives the range of the potential. The potential gives a scattering length a . Outside the range of the potential ($\rho \gg \ell$), ρ denoting the relative coordinate of a two-body subsystem, and for a large scattering length ($a \gg \rho$) the zero-energy solution for the binary scattering wave function of a given subsystem $\psi(\rho)$ to first order in ρ/a is $\psi(\rho) = 1 - \rho/a$, irrespective of details of the interaction. Using this universal expression, Efimov found analytic solutions for the hyperangular eigenfunctions ϕ_n , which in turn yield a transcendental equation for $\lambda_n(R)$. In Fig. 5.2 which is adapted from Ref. [Bra06] numerical solutions to the transcendental equation are shown. The lowest three channel eigenvalues $\lambda_n(R)$ for $a < 0$ and $a > 0$ are shown as functions of $R/|a|$. For $R \ll |a|$, the eigenvalues approach constants independent of a . The lowest eigenvalue λ_0 approaches -1.0125 in the limit of $R/|a| \rightarrow 0$ [Efi71, Efi79, Fed93, Nie01, Bra06]. All other eigenvalues assume positive values in that limit.

Upon substituting this value into the hyperradial equation (5.11), we obtain an attractive channel potential $V(R) \propto -1.2625/R^2$, which supports an infinite number of bound states. This is the origin of Efimov's effect.

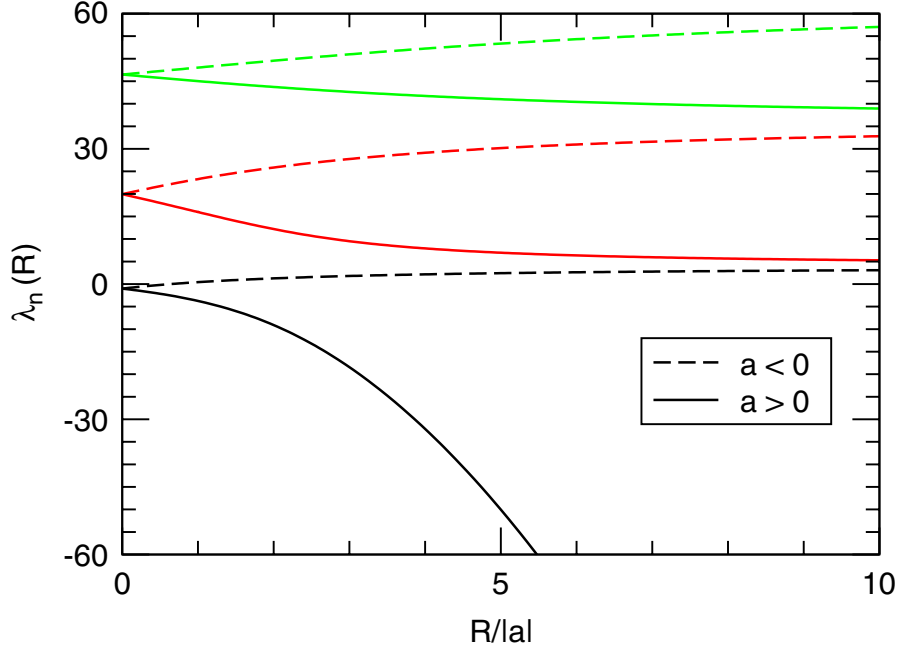


Figure 5.2: The lowest three channel eigenvalues $\lambda_n(R)$, ($n = 1, 2, 3$), as a function $R/|a|$ for $a > 0$ (solid lines) and $a < 0$ (dashed lines). The figure has been taken from Ref. [Bra06].

It is convenient to introduce a scalar s_0 such that $-s_0^2 = \lambda_0$. Let κ be the binding wave number related to an Efimov state's binding energy $E_T = \hbar^2 \kappa^2 / m$ in the limit of $|a| \rightarrow \infty$. As a universal property of the hyperradial wavefunctions f_0 of Efimov states in the limit of $\kappa R \ll 1$,

$$f_0(R) = -(\pi/[s_0 \sinh(\pi s_0)])^{1/2} R^{1/2} \sin[s_0 \ln(\kappa R) + \alpha_0], \quad (5.12)$$

where α_0 is some universal phase. The spectrum of Efimov states $E_T^{(n)}$ in the limit of $\kappa R \ll 1$ is universally given by

$$E_T^{(n)} = (e^{-2\pi/s_0})^{n-n_*} \frac{\hbar^2 \kappa_*^2}{m}, \quad (5.13)$$

where κ_* is the binding wave number for the Efimov state $E_T^{(n_*)}$. Thus any two adjacent Efimov states are spaced by a factor of $e^{-2\pi/s_0} \approx 1/515$ in binding energy. As a non-universal property of the Efimov spectrum κ_* is related to a so-called three-body parameter which depends on the structural details of the two-body interaction. It is determined by the fact that the hyperspherical wavefunctions have to fulfil some unknown boundary condition at short range.

Note that the $e^{-2\pi/s_0}$ -scaling of the spectrum is strictly given only in the limit where $\ell/|a| \rightarrow 0$. For realistic potentials there is a cut-off at small distances, leading to a bound of the Efimov spectrum from below. Hence there is a first or most deeply

bound Efimov state, and for the first few higher lying states the scaling holds in an approximate sense only.

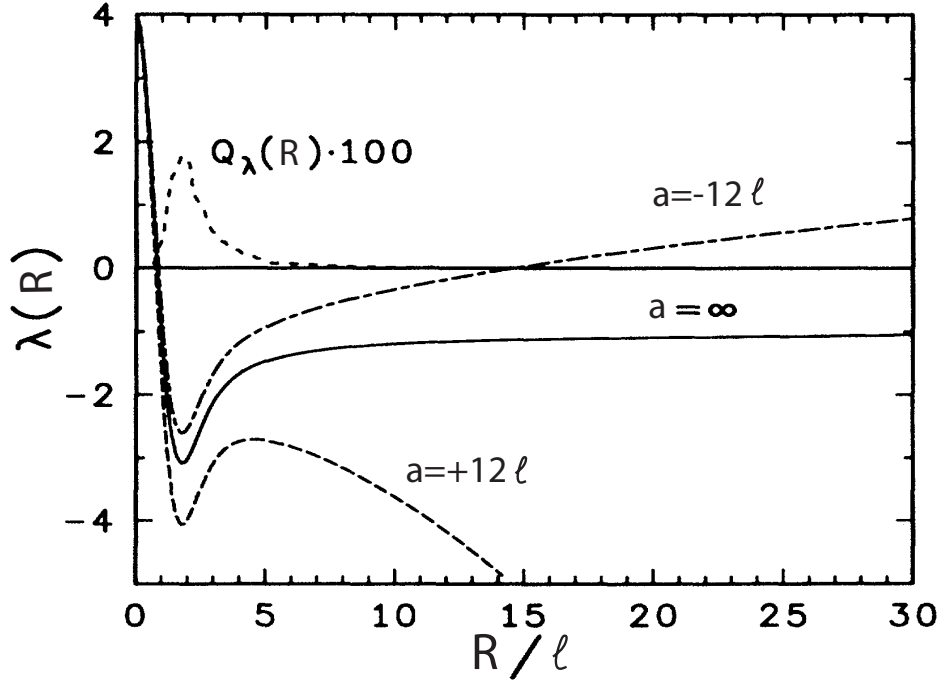


Figure 5.3: The lowest hyperspherical channel eigenvalue λ_0 as a function of the hyperradius R for a Gaussian two-body model potential. Its range is denoted by ℓ and its depth is adjusted to produce scattering lengths of $a = -12\ell$ (dot-dashed curve), $a = +12\ell$ (dashed curve) and $a = \infty$ (solid curve). The diagonal part of the coupling potential $\langle \phi | \frac{\partial^2}{\partial R^2} | \phi \rangle \equiv Q_\lambda$ is magnified by a factor of 100. For $a = \infty$ and $R \gg \ell$ $\lambda_0 \rightarrow -1.0125$. The figure has been adapted from Ref. [Fed93].

In the intermediate region where $R \leq \ell$ the universal expression for the two-body scattering wave function $\psi(\rho) = 1 - \rho/a$ is not valid and the behavior of the lowest hyperspherical channel potential is not obvious. Numerical solutions to the α -dependent part of the Faddeev equation [Fed93] visualize the behavior of $\lambda_0(R)$. Fig. 5.3 which is adapted from Ref. [Fed93] shows λ_0 as a function of R for small R . It also illustrates the effects of finite positive or negative scattering lengths on $\lambda_0(R)$ by showing the region where $R \approx |a|$. The numerical calculations use a Gaussian two-body model potential $U(\rho) = U_0 \exp(-\rho^2/\ell^2)$ of depth U_0 and range ℓ which is adjusted to produce scattering lengths of $a = \pm 12\ell$ and $a = \infty$.

For $R = 0$ the limit is $\lambda_0(R) = 4$ in all cases. For large and finite *positive* $a \gg \ell$, the system supports a universal two-body bound state with a binding energy $E_b \propto 1/a^2$. The hyperradial channel potential V reflects the existence of a universal dimer by the fact that $V(R) = -E_b$ for $R \gg \ell$. Since $V(R) \approx \lambda_0(R)\hbar^2/(2mR^2)$ the binding energy of the binary subsystem leads to a parabolic shape of $\lambda_0(R)$ which is clearly visible in

Fig. 5.3. For large but finite *negative* $a \ll -\ell$ and for large $R \gg \ell$ $\lambda_0(R)$ returns to 4. At $R \approx 20\ell$ in Fig. 5.3 λ_0 becomes larger than 1/4 and renders the hyperspherical potential repulsive. Fig. 5.3 clearly shows local minima of λ_0 at $R \approx 2\ell$ leading to local minima of the channel potential and in consequence to a bound of the Efimov spectrum from below.

In essence a finite $|a|$ cuts off the attractive $-1/R^2$ hyperspherical channel potential at $R \approx a$ and limits the number of Efimov states. A good estimate of the number of Efimov states at a given scattering length and potential range ℓ is given by counting the nodes of the hyperradial wavefunction in between ℓ and $|a|$, i.e. $N_E \simeq \frac{s_0}{\pi} \ln(\frac{|a|}{\ell})$ [Efi71, Bra06, Nie01].

5.1.4 Efimov's scenario

The universal dimer state and the series of Efimov states are visualized in what is known as Efimov's scenario [Efi71, Efi79]. It illustrates Efimov's findings in terms of the the energy spectrum of the three-body system as a function of the inverse scattering length $1/a$. Efimov's scenario is depicted in Fig. 5.4. Here, the resonance limit corresponds to $1/a \rightarrow 0$, the dimer energy E_b is represented by a parabola for $a > 0$.

A natural three-body threshold is given by $E = 0$ and $E = E_b$ for negative and positive a , respectively. This threshold is indicated by the hatched line in Fig. 5.4. States energetically below this threshold are necessarily three-body bound states. When $1/a$ approaches the resonance from the negative- a side, a first Efimov trimer state appears in a range where a weakly bound two-body state does not exist. When passing through the resonance the state connects to the positive- a side, where it finally disappears at the dimer-atom threshold. An infinite series of such Efimov states is found when scattering lengths are increased and energies are decreased in powers of the universal scaling factors [Efi71, Efi70, Bra06] $e^{\pi/s_0} \approx 22.7$ and $e^{2\pi/s_0} \approx 515$ ($s_0 = 1.00624$), respectively.

The binding energy of the first Efimov state $E_T^{(0)}$ at the point where it passes through resonance depends on the details of the short-range part of the interaction and is thus not universal. In consequence also the point of intersection between the first Efimov state and the three-atom threshold (marked $a_-^{(0)}$ in Fig. 5.4) and the point where the first Efimov state connects to the dimer state (marked $a_{ad}^{(0)}$ in Fig. 5.4) are not universal. In order to describe the three-body problem in the universal regime $\ell/|a| \rightarrow 0$ two parameters are required, the scattering length and the three-body parameter introduced in the previous section. The three-body parameter determines the Efimov spectrum and thus fixes the $E_T^{(n)}$. For realistic potentials the scaling behavior of the binding energies $E_T^{(n)}$ of the Efimov spectrum is strictly given only for large n as outlined in the previous section.

5.1.5 The search for Efimov effects so far

V. Efimov as a nuclear theorist proposed to consider a system of three ^{12}C or three ^3H nuclei in order to confirm his predictions. Many other nuclear systems have been

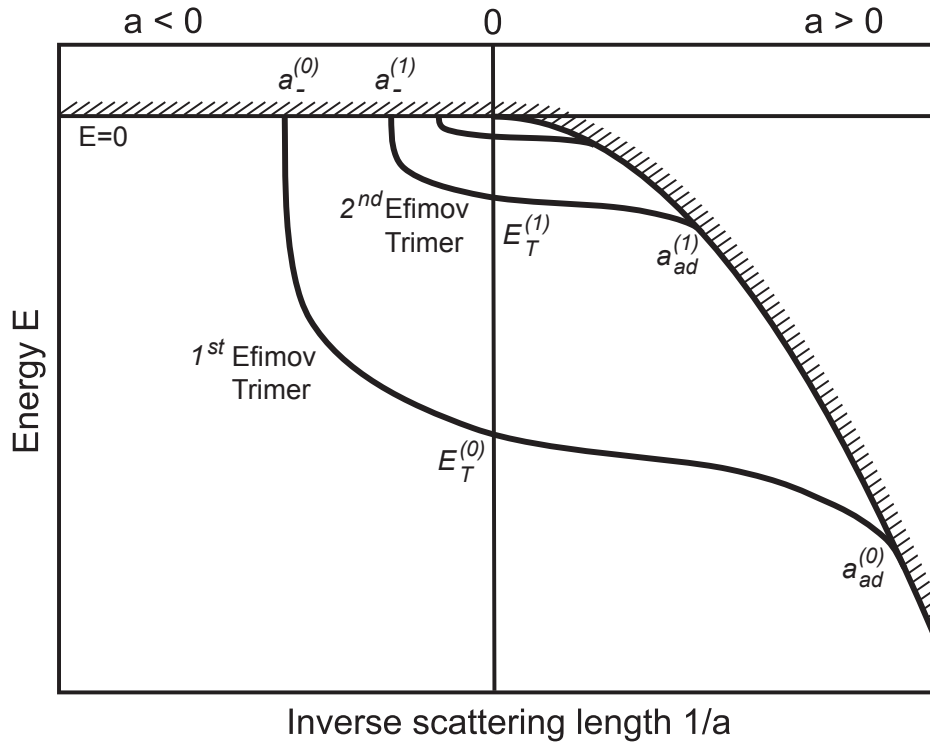


Figure 5.4: Efimov's scenario. Appearance of an infinite number of bound trimer states for resonant two-body interaction. The binding energy is plotted as a function of the inverse scattering length $1/a$. Above the hatched line, the scattering continuum for three atoms ($a < 0$) and for an atom and a dimer ($a > 0$) is situated. The $a_{-}^{(n)}$ mark the intersection of the Efimov trimers with the three-atom threshold, and the $a_{ad}^{(n)}$ mark the points where the Efimov trimers disappear into the atom-dimer scattering continuum. The $E_T^{(n)}$ denote the Efimov state binding energy for $|a| \rightarrow 0$. To illustrate the series of Efimov states, the universal scaling factor is reduced from 22.7 to 2.

theoretically investigated since then. Despite extensive searches, however, no example for the Efimov effect has been found up to now. In general, the long-ranged Coulomb interaction prevents the appearance of Efimov states, and only very weakly bound two-neutron ($n + n$) systems surrounding a spinless core are expected to be possible candidates. For a review and a discussion of the prospects for observing Efimov phenomena in nuclear systems see [Jen04] and references therein. The search for suitable nuclear systems is very active, the latest publications investigating a $n + n + {}^9\text{Li}$ system [Gar06] and a $n + n + {}^{18}\text{C}$ system [Maz06].

In molecular physics the ${}^4\text{He}$ system supports exactly one (bound) dimer state. The dimer and the ground state of the three-atom bound state spectrum (the Thomas trimer) have been detected [Sch94]. The existence of an excited trimer state representing an Efimov state is expected [Gri00]. The trimer ground and Efimov state differ in size by an order of magnitude and should be distinguishable in matter wave diffraction exper-

iments as performed in Ref. [Brü05]. This experiment is based on diffracting a beam of ^4He clusters by an inclined transmission grating. A 10 % fraction of trimers in the Efimov state was estimated for the beam parameters. However the presence of Efimov trimers in the beam at the grating position could not be confirmed. Their occurrence was excluded to within a remaining experimental uncertainty of 6 % [Brü05].

Other molecular systems which might support Efimov states have been investigated theoretically. The Efimov effect for spin-1/2 fermions with arbitrary relative subsystem angular momenta l has been analyzed in Ref. [Mac06]. The authors indeed find a hyperradial channel potential supporting an infinite number of Efimov trimer states. More specifically, this is the case for three spin-1/2 fermions in a state with 1/2 total spin and with $l = 1$.

5.2 Efimov states in ultracold gases

In contrast to other systems ultracold gases offer almost complete control over the internal and external degrees of freedom. The ultralow temperatures allow to explore quantum scattering in the limit of zero collision energy. Ultracold gases can serve as a model system capable of accessing the full Efimov's scenario due to the presence of magnetically tunable open-channel dominated Feshbach resonances. The presence of Efimov states in ultracold gases dramatically influences zero-energy collisions involving three atoms, atoms and dimers and possibly also collisions of dimers with dimers. In the universal regime Efimov derived analytic expressions for several three-body collision processes, known as Efimov's radial law [Efi79], including the cross section for three-particle scattering at zero energy and particle-pair scattering cross sections, both elastic and inelastic. The atom-dimer scattering cross section is generally proportional to the atomic scattering length a [Efi79] and the three-body collision cross section generally scales as a^4 [Fed96]. In addition to this smooth scaling the two collision cross sections display a logarithmic periodicity when the scattering length is varied due to the appearance of Efimov states. The logarithmic periodicity corresponds to the universal scaling factor e^{π/s_0} .

The formation of a bound diatomic molecule in a three-body collision is called recombination event. In ultracold gases recombination is a first step towards the association of molecules and larger compounds and ultimately limit the lifetime of trapped atomic vapors. The physical picture behind the effect of Efimov states on recombination depends on the sign of the scattering length. For negative a , recombination can only occur into deeply bound non-universal dimer states. It is resonantly enhanced when the presence of an Efimov trimer opens up an additional recombination pathway. For positive a , recombination occurs predominantly into the universal dimer state. The *incoming* three colliding atoms necessarily see a repulsive hyperspherical channel potential because the only attractive channel potential contains the two-body bound state. The recombination event corresponds to a decay into the attractive channel. The incoming three-atom wave function decays into an *outgoing* and an *incoming* atom-

dimer wave function. The ingoing part acquires a phase with respect to the outgoing part which depends on a . The interference of the two parts [Esr99, Esr06] cause an oscillatory recombination pattern under variation of a .

In trapped gases the recombination event rate per unit volume and time is given by $\alpha_{rec}n^3$, where n denotes the atom number density and α_{rec} is called the recombination rate coefficient. The release of the two-body binding energy of the newly formed molecule resulting from recombination can lead to loss from typical atom traps and to heating of the remaining trapped sample. The possible heating mechanisms are described in Sec. 5.5.1. The trap loss as a function of time can be used to experimentally determine α_{rec} once the trapping parameters are known. In the following section the usual simple model for the time evolution of the trapped atom number $N(t)$ as determined by the relevant loss processes is introduced.

5.2.1 Signature of trap loss

Up to three-body processes, particle loss from a trap is governed by the following differential equation for the atomic number density $n(\mathbf{r}, t)$

$$\dot{n}(\mathbf{r}, t) = -\tau^{-1}n(\mathbf{r}, t) - L_2n^2(\mathbf{r}, t) - L_3n^3(\mathbf{r}, t), \quad (5.14)$$

where τ , L_2 and L_3 denote the $1/e$ lifetime, the two-body and the three-body loss rate constants, respectively. Integrating Eq. 5.14 over the sample gives $\dot{N}(t)/N(t) = -\tau^{-1} - L_2\langle n \rangle(t) - L_3\langle n^2 \rangle(t)$, $N(t)$ being the total particle number. Granted that the collision loss rate is slow compared to the rate of thermalization, the sample retains its initial density distribution $n(\mathbf{r}, t) = n(\mathbf{r}, 0)/N(0) \times N(t)$. Thus, by introducing an effective volume $V_{\text{eff}}^{-1} = \int_V d^3r n^2(\mathbf{r}, 0)/N^2(0)$, Eq. 5.14 gives an expression for the directly accessible quantity $N(t)$. For a sample with a gaussian distribution at a constant temperature T in a harmonic trap with a geometrically averaged trap frequency $\bar{\omega} = \sqrt[3]{\omega_x\omega_y\omega_z}$ the effective volume is given by $V_{\text{eff}} = (m\bar{\omega}^2/(4\pi k_B T))^{-3/2}$, m being the particle mass. The differential equation for the particle number takes on the form

$$\dot{N} = -\alpha N - \beta N^2 - \gamma N^3, \quad (5.15)$$

with $\alpha = \tau^{-1}$, $\beta = L_2/V_{\text{eff}}$ and $\gamma = (4/3)^{3/2} \cdot L_3/V_{\text{eff}}^2$. Here the temperature is assumed to remain constant. A derivation of differential equations for $N(t)$ and $T(t)$ in the case of non-constant temperature as a result of the aforementioned heating mechanisms is given in Sec. 5.5.1.

For finite α and β , but sufficiently small γ , meaning $L_3\langle n^2 \rangle \ll L_2\langle n \rangle$, Eq. 5.15 is solved by

$$N(t) = \frac{\alpha N_0}{(\alpha + \beta N_0)e^{\alpha t} - \beta N_0}. \quad (5.16)$$

Similarly, if three-body processes dominate, $L_2\langle n \rangle \ll L_3\langle n^2 \rangle$, the solution is

$$N(t) = \left(\frac{\alpha N_0^2}{(\alpha + \gamma N_0^2)e^{2\alpha t} - \gamma N_0^2} \right)^{1/2}. \quad (5.17)$$

The three-body loss rate constant L_3 and the recombination coefficient α_{rec} are connected via

$$L_3 = n_l \alpha_{rec}, \quad (5.18)$$

where n_l gives the number of lost atoms as a result of one recombination event. n_l depends on trapping parameters and binding energy of the newly formed molecule as outlined in Sec. 5.5. Usually $n_l = 3$ can be assumed.

5.2.2 Three-body recombination as a function of scattering length

For large positive scattering length a the recombination coefficient α_{rec} was shown to generally scale as $\alpha_{rec} = C\hbar a^4/m$ [Fed96]. Here m is the mass of one atom and C is a dimensionless parameter. In 1999 the authors of Ref. [Nie99] argued that also for large negative scattering lengths the a^4 -scaling holds and derived an upper limit C_{max} equal to 68.4 for positive a . Shortly thereafter the authors of Ref. [Esr99] demonstrated the a^4 -scaling for large $|a|$ in numerical calculations using various two-body model potentials. They also showed that C can take on values in between $0 < C < 60$ due to a quantum mechanical interference effect for $a > 0$ and that C is resonantly enhanced at certain negative values of a . In 2000 the authors of Ref. [Bed00] introduced a field theoretical approach which confirmed the predictions of Refs. [Nie99, Esr99] and showed that the variations of C display a logarithmically periodic oscillation $C(a) = C(22.7a)$ in the limit where $a \rightarrow \infty$. In 2001 Ref. [Bra01] showed a logarithmic periodicity with a factor of 22.7 in the resonance pattern of $C(a)$ in the case of large negative a in the limit of $|a| \rightarrow \infty$. Analytical expressions from field theory exist for α_{rec} in the case of positive [Bed00] and negative scattering length [Bra01]. For a review of the field theory approach refer to Ref. [Bra06].

The logarithmic periodicity of the parameter $C(a)$ reflects the existence of the infinite series of weakly bound Efimov trimers in the limit of infinite scattering length. $C(a)$ in the simultaneous limit of infinite $|a|$ and zero temperature is given by the two following analytical expressions from the field theoretical approach [Bra06].

Negative scattering length

The crossing points of the Efimov trimer states with threshold are located at $a = a_-, 22.7a_-, \dots$. These crossings result in enhanced three-body loss rates which we call triatomic Efimov resonances. As outlined in Sec. 5.1.3 and Sec. 5.1.4 the value of a_- depends on the short range properties of the specific three-body interaction of Cs. Efimov's radial law does not include the presence of tightly bound pair states [Efi79]. The field theoretical approach [Bra01, Bra06] extends Efimov's radial law by taking into account the presence of deeply bound non-universal dimer states. It introduces another non-universal parameter η_- related to the width of the triatomic Efimov resonance as a result of possible decay of Efimov trimers into these deeply bound states.

This approach provides the analytic expression

$$C(a) = 4590 \sinh(2\eta_-) / \left(\sin^2 [s_0 \ln(|a|/a_-)] + \sinh^2 \eta_- \right). \quad (5.19)$$

Triatomic Efimov resonances can be interpreted as a three-body analogue to Feshbach resonances.

Positive scattering length

The existence of the universal dimer state at large positive scattering lengths leads to an oscillatory behavior of three-body loss due to the interference effect outlined in Sec. 5.2. As in the case of negative a the effective field theory approach [Bed00, Bra06] extends Efimov's radial law by allowing for the presence of more deeply bound non-universal dimer states. It introduces the non-universal parameter η_+ which determines the contrast of the oscillation in $C(a)$. Recombination into non-universal dimers remains constant under variation of a . We define the non-universal parameter a_+ such that maxima of $C(a)$ are found at scattering lengths $a = a_+, 22.7a_+, \dots$. The analytic expression then reads

$$C(a) = 67.1 e^{-2\eta_+} \left(\cos^2 [s_0 \ln(a/a_+)] + \sinh^2 \eta_+ \right) + 16.8 (1 - e^{-4\eta_+}) \quad (5.20)$$

with the two non universal parameters a_+ and η_+ . The first term describes recombination into the weakly bound universal dimer state showing the oscillatory behavior. The second term results from decay into deeply bound states.

Efimov's scenario suggests a fixed relation between a_+ and a_- apart from factors of e^{π/s_0} in the sense that $\ln(a_+/|a_-|) \bmod \pi/s_0$ is a constant. The theoretical approach [Bed00, Bra01, Bra03, Bra06] predicts $a_+ = 0.96|a_-|$ in the limit of $|a| \rightarrow \infty$. According to theory [Bra03, Bra06], the trimer states connect to the dimer-atom threshold at $a_{ad} = 1.1a_+$ apart from factors of e^{π/s_0} .

5.2.3 Temperature limitations to the observation of three-body recombination

In general, the experimental access to the resonant regime at large absolute values of the scattering length will be restricted by unitarity, which limits the recombination rate to finite values at finite temperatures, thus causing a saturation effect. Also, at nonzero temperatures, the resonance and oscillation patterns of α_{rec} are expected to wash out due to thermal averaging. These effects have been investigated theoretically in Ref. [D'I04] in numerical calculations. The authors use the mass of helium atoms and a model dimer potential $\propto D \sec^2(r/r_0)$, with D and r_0 adjusted to give a single two-body s -wave bound state. Their results visualize the saturation and averaging effects of finite temperatures on recombination and are shown in Fig. 5.5, which has been taken from Ref. [D'I04]. The three-body recombination rate is labelled K_3 ($K_3 = 2\sqrt{3}\alpha_{rec}$) and plotted as a function of negative (a) and positive (b) scattering length.

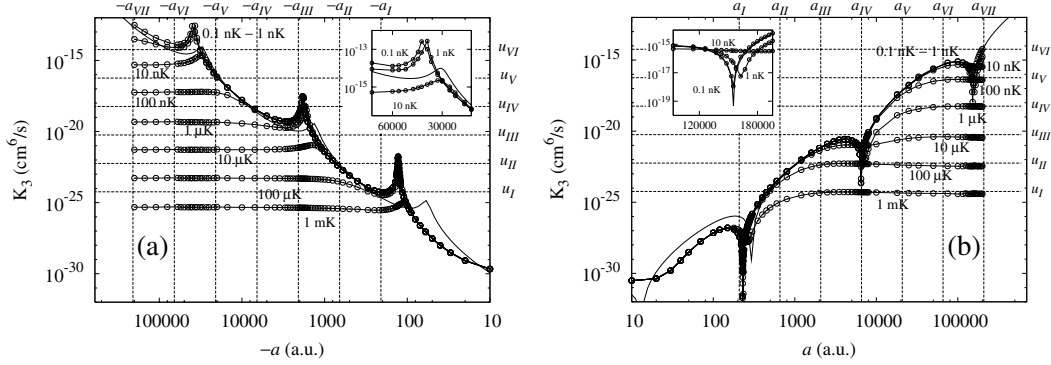


Figure 5.5: Numerically calculated three-body recombination rate for (a) negative a and (b) positive a . The calculation is based on ^4He two-body interaction parameters and carried out for various temperatures. The horizontal lines represent the unitary limit u_N for a given temperature. A characteristic length scale a_N can be assigned to each temperature. For $a \geq a_N$, the scattering cross sections are no longer determined by a . The a_N are indicated by the vertical lines. The numerical data points are interconnected by straight lines. The solid curves are analytical expressions from universal theory, similar to those introduced in the previous section. The insets show the third resonance peak (a) and the third interference minimum (b) as counted from $a = 0$. In the analytical formulas, a phase and a width parameter, essentially a_{\pm} and η_{\pm} of the preceding section, are adjusted to give the best fit to the third interference minimum at 0.1 nK. For any given temperature, the rates deviate from the universal curve at some point, with the highest temperature departing soonest, and approach the corresponding unitary limit. In plot (a) the triatomic Efimov resonances appear as spikes and in plot (b) the oscillation is seen as dips. Note that the pattern periodicity of the universal curve differs somewhat from that of the numerical data. The difference reflects the fact that the universal e^{π/s_0} -scaling applies only approximately for the first few Efimov states. The figure has been taken from Ref. [D'I04].

At ultralow but finite collision energies, triatomic Efimov resonances are expected to shift to lower absolute values of the scattering length as they evolve into continuum resonances [Bri04]. When contributions from higher partial waves become energetically allowed they obscure Efimov-related effects on recombination [Fed93, Nie01, D'I04, Bra06].

5.3 Experimental access to the universal regime

The dimer level structure just below the $(F = 3, m_F = 3) \times (F = 3, m_F = 3)$ threshold was introduced in Sec. 3.3. This section discusses possible access to the universal regime for magnetic fields up to 150 G which is currently the maximum field strength we can generate.

In this region our system clearly does not reproduce the original Efimov scenario.

5.4 Results from three-body recombination loss measurements

The regions of attractive and repulsive interaction are not separated by a singularity of the scattering length but by a zero crossing. It is not obvious how Efimov physics interconnects the two regions in this case. Also, the role of the narrow Feshbach resonances with respect to three-body physics is not undisputed. Except for the close vicinity of the narrow Feshbach resonances, however, the scattering length is solely determined by the open-channel dominated Feshbach resonance centered at -12 G which leads to a smooth variation of a between $-2500 < a < 1500 a_0$ for magnetic field strengths B between $0 < B < 150$ G.

The characteristic range ℓ of the Cs two-body potential is determined by the C_6/r^6 -tail of the van-der-Waals interaction which can be quantified by the van-der-Waals length $l_{vdW} = (mC_6/\hbar^2)^{1/4}/2$ [Köh06]. Taking $\ell \equiv l_{vdW} = 101 a_0$ we are given ample leeway to study the universal regime requiring $a \gg \ell$. Efimov's estimate $\frac{1}{\pi} \ln(|a|/\ell)$ for the number of weakly bound trimer states [Efi71] suggests the presence of one triatomic Efimov resonance in the accessible range of negative scattering lengths.

In our measurements of the recombination coefficient α_{rec} we carefully avoid regions where the narrow resonances influence the scattering length. We compare only data with $a > 500 a_0 \approx 5\ell$ to theory. This somewhat arbitrary condition is introduced as a reasonable choice to satisfy $a \gg \ell$ for the validity of the universal theory.

5.4 Results from three-body recombination loss measurements

We visualize the general trend of recombination loss by measuring the loss of atoms after a fixed storage time in the optical traps as a function of scattering length. For *negative* scattering lengths this is plotted in Fig. 5.6. The data recorded at an initial temperature of 350 nK shows narrow loss resonances which correspond to the Feshbach resonances at 11, 14.5, 15 and 20 G. A broad loss feature around -800 G is visible which cannot be attributed to two-body physics and marks a possible triatomic Efimov resonance. For $a < -1500 a_0$ the fraction of lost atoms settles at a value of 65 % due to trap depletion. For comparison data taken at an initial temperature of 650 nK is shown. Here, the broad loss feature is not visible. For *positive* scattering lengths the data is shown in Fig. 5.7. The data reveals the occurrence of a loss minimum unaccounted for by two-body physics. The minimum is located at $a = 210(10) a_0$ in addition to a second minimum close to zero scattering length. Note that the existence of the minimum at $210 a_0$ is very advantageous for efficient evaporative cooling of Cs as it combines a large elastic scattering cross section with very low loss.

Our quantitative measurements of the recombination rate coefficient α_{rec} are presented in terms of the three-body loss rate $L_3 = 3\alpha_{rec}$ in Fig. 5.8 together with previous data from the same apparatus [Web03c] and data from a second Cs BEC apparatus [Ham02, Ryc04]. Fig. 5.8 shows L_3 as a function of the scattering length a . For $a < 0$ two different data sets have been taken which correspond to initial sample tempera-

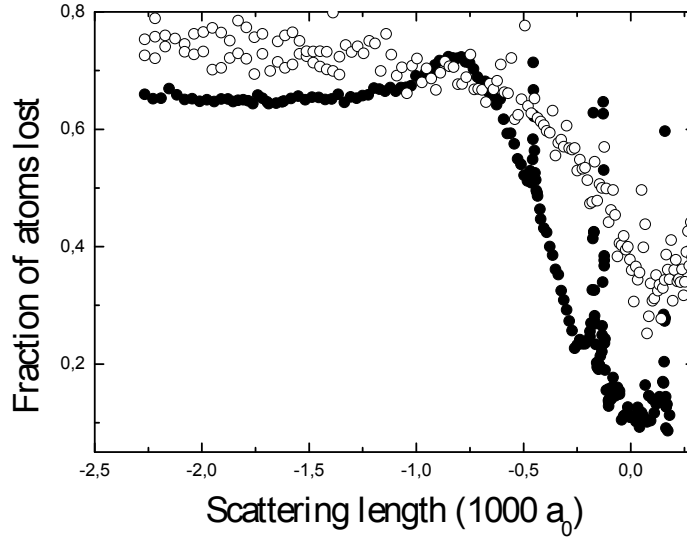


Figure 5.6: Fraction of lost atoms after 1 s of storage time for negative scattering lengths. The filled and empty dots represent data at an initial temperature of 350 nK and 650 nK, respectively. Besides several narrow loss resonances due to narrow Feshbach resonances one broad resonant feature around $800 a_0$ is clearly visible in the 350 nK data. It is not visible in the 650 nK data. The narrow loss resonances correspond to Feshbach resonances at 11, 14.5, 15 and 20 G. For details on trapping parameters, initial densities and atom numbers see Sec. 5.4.1.

tures of 10 and 200 nK. For $a > 0$ the initial sample temperature was 200 nK. We observe a resonant enhancement of L_3 at $-800 a_0$ and two local minima of L_3 around 100 and 200 a_0 . A fit of the zero-temperature expression Eq. (5.19) resulting from the analytic theory [Bra01, Bra06] to our experimental data taken for negative a at temperatures $T \approx 10$ nK shows a remarkable agreement with the data. It determines the resonance position to $a_- = -850(20) a_0$ and the decay parameter to $\eta_- = 0.06(1)$. The pronounced resonance behavior results from a small value for the decay parameter ($\eta_- \ll 1$). The grey lines result from setting the \sin^2 and \cos^2 -terms in Eqs. (5.19) and (5.20) to unity and represent the general a^4 -scaling.

For positive scattering lengths we found three-body losses to be typically much weaker than for negative values. Our measurements are consistent with a maximum recombination loss of $C_{max}(a) \approx 70$ as predicted by [Nie99, Esr99, Bed00]. The grey line for $a > 0$ indicates the a^4 -scaling with $C = C_{max}$ in Fig. 5.8. For a below 600 a_0 the measured recombination length significantly drops below this upper limit. This region is shown more clearly in the inset. The fit of Eq. (5.20) is quite insensitive to the value of the decay parameter and yields $0 < \eta_+ < 0.2$. This is consistent with the theoretical assumption [Bra01] of the same value for the decay parameter for positive

5.4 Results from three-body recombination loss measurements

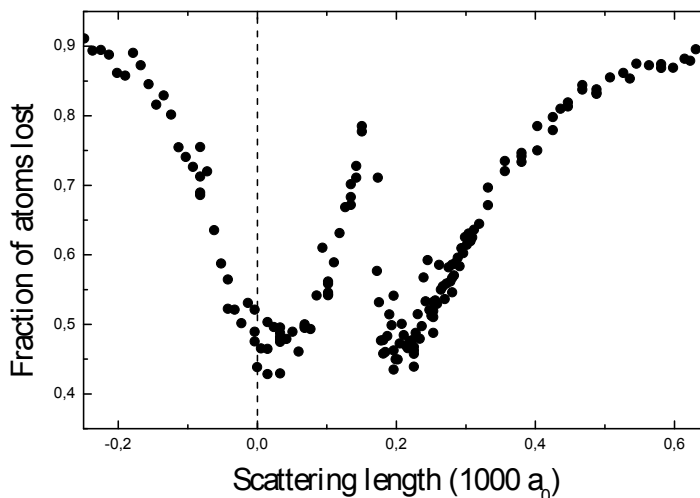


Figure 5.7: Atom loss after a fixed storage time of 200 ms. The initial temperature was 250 nK. Besides a minimum near zero scattering length we observe another minimum of recombination loss around $210 a_0$ which cannot be attributed to known two-body physics. Data points which could be affected by a narrow g -wave Feshbach resonance situated in the vicinity of $200 a_0$ have been removed.

and negative a , which in our case is $\eta_+ = \eta_- = 0.06(1)$. For the position of maximum loss a_+ , we obtain $a_+ = 1060(70) a_0$. According to theory [Bra06] the dimer-atom threshold is thus located at $a = 1.1 a_+ \approx 1170 a_0$. The logarithmic periodicity of the Efimov scenario suggests adjacent loss minima to occur at $\sqrt{22.7} \times 1060 a_0 \approx 5000 a_0$ and at $1060 a_0 / \sqrt{22.7} \approx 220 a_0$. While the former value is out of our accessible range, the latter value ($a \approx 2\ell$) is too small to strictly justify universal behavior in the resonant limit ($a \gg \ell$). Nevertheless, our experimental results shown in the inset to Fig. 5.8 and in Fig. 5.7 indicate a minimum at $a \approx 210 a_0$ and the analytic expression for $C(a)$ is found to describe our data quite well down to this minimum.

The results discussed so far are valid in the zero-energy collision limit of sufficiently low temperatures. For non-zero temperatures the recombination rate is unitarity limited [D'I04, Gre05] to $844\hbar^5/(m^3k_B^2T^2)$. For $T = 10$ nK this limit corresponds to about 5.6×10^{-20} cm⁶/s and our sample is thus cold enough to justify the zero-temperature limit. For 250 nK, however, unitarity limits the recombination rate to about 9.0×10^{-23} cm⁶/s. The Efimov resonance is still visible at temperatures of 200 and 250 nK represented by the filled triangles and open diamonds in Fig. 5.8, even though less pronounced and slightly shifted [Bri04] to lower values of $|a|$. In our trap loss measurements we observed the resonant loss structure to disappear above ~ 500 nK, see Fig. 5.6.

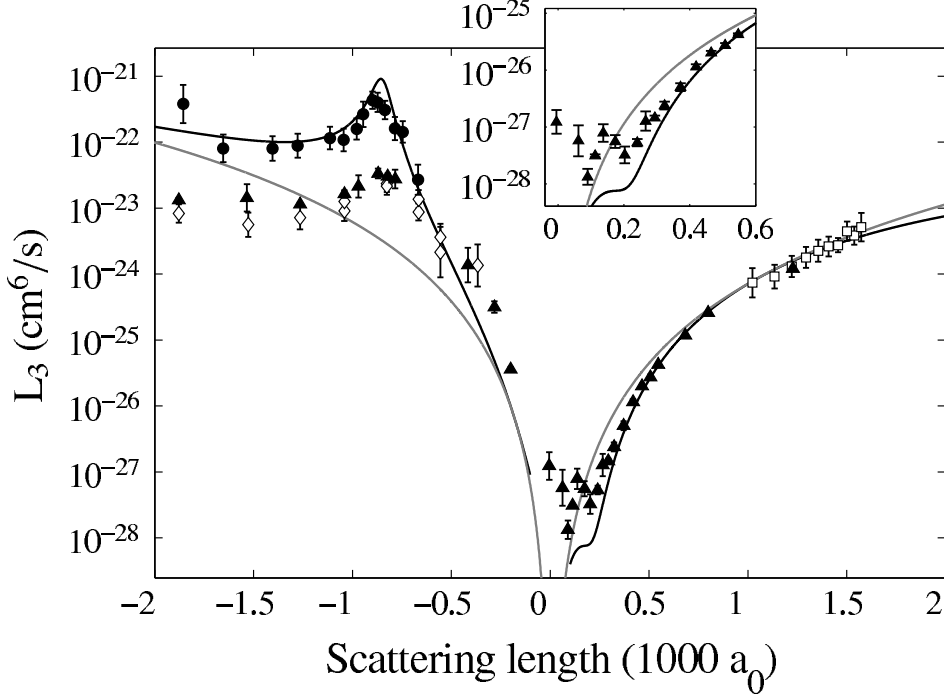


Figure 5.8: Three-body loss rate $L_3 = 3\alpha_{rec}$ as a function of the scattering length a . The dots and triangles represent data taken at initial temperatures of 10 nK and 200 nK, respectively. The open squares are previous data at initial temperatures between 250 and 450 nK. The open diamonds represent 250 nK data taken independently at a second Cs BEC apparatus [Ham02, Ryc04]. The solid black line represents the fits according to the effective field theory, the grey lines result from setting the \sin^2 and \cos^2 -terms in Eqs. (5.19) and (5.20) to unity and represent the general a^4 -scaling. The regions of positive and negative scattering lengths are fitted independently. The inset is a zoom into the region $0 < a < 600 a_0$ showing the two local minima for L_3 more clearly.

5.4.1 Trapping parameters for recombination loss measurements

At large *negative* values of the scattering length the large recombination rates lead to trap depletion which obscures possible variations of α_{rec} in measurements of trap loss after a fixed storage time. We use samples with as low an initial atomic density as possible. The absence of a magnetic field gradient allows to resolve the narrow Feshbach resonances. The two data sets in Fig. 5.6 were recorded using the elliptic trap without the levitation gradient. The filled (empty) data points in Fig. 5.6 were recorded with an initial atom number of 8×10^5 (2×10^5) resulting in an initial density of $5.8 \times 10^{12} \text{ cm}^{-3}$ ($1.6 \times 10^{12} \text{ cm}^{-3}$). The gradient was gradually turned off within 180 ms after trap loading. The start of the hold time was defined by a jump to the magnetic field value in question, the hold time was 1 s. For trapping frequencies and

5.4 Results from three-body recombination loss measurements

trap depths of the elliptic trap see Sec. 4.5.

At *positive* values of a three-body loss is generally much lower. For the attainment of reasonable initial atomic densities in measurements of trap loss after a fixed storage time we use the dimple trap. The data in Fig. 5.7 was recorded from a trap with 42 mW in the dimple beam D1 and reservoir beam L1 after a hold time of 200 ms at each magnetic field value. The trap frequencies were determined to $\omega_{\text{rad}} = 2\pi \times 168$ Hz in the radial and $\omega_{\text{ax}} = 2\pi \times 14$ Hz in the axial direction resulting in a trap depth of a few $\mu\text{K} \times k_B$. With 8×10^5 atoms at the beginning of the waiting time the mean initial density was $6.4 \times 10^{12} \text{ cm}^{-3}$. The initial sample temperature was 250 nK.

For our quantitative measurements of L_3 plotted in Fig. 5.8 we have taken data at initial temperatures of less than 10 nK and around 200 nK. We use the dimple trap for negative a and the reservoir trap for positive a . The attainment of a condensate was a crucial step for achieving temperatures in the few-nK regime. We create these low temperatures by stepping the magnetic field from 22 G to 16.2 G after producing an almost pure BEC which is characterized in Sec. 4.6. The step corresponds to a sudden jump from a scattering length of $a = 210 a_0$ to a value of $a = -50 a_0$ and induces a collapse of the condensate. We allow 1 s for equilibration of the remains. We are left with up to 2×10^4 atoms at mean densities around $8 \times 10^{11} \text{ cm}^{-3}$ in a shallow trap of only $75 \text{ nK} \times k_B$ depth. The measured trap frequencies were $\omega_{\text{rad}} = 2\pi \times 24$ Hz and $\omega_{\text{ax}} = 2\pi \times 3$ Hz.

Condensates with attractive interaction are not necessarily unstable. In a trap, the kinetic energy of the condensate counteracts the attraction and stabilizes the condensate for small enough attractive interactions. The criterion for stable condensates can be calculated with $N_c |a|/a_{ho} = 0.574$ [Rob01], where N_c is the maximum number of atoms in the condensate at a given scattering length a and $a_{ho} = \sqrt{\hbar/m\bar{\omega}}$ the harmonic oscillator length characterizing the ground state kinetic energy and $\bar{\omega}$ the geometrically averaged trap frequency. Inserting the typical trap parameters and $a = 50 a_0$ gives $N_c \approx 900$. Atom number and temperature of the remaining cloud are found to be independent of the final scattering length value for $a < -50 a_0$.

For our quantitative measurements of the L_3 coefficient at temperatures around 200 nK we interrupt the evaporation ramp shortly before reaching the critical temperature. We do not replace reservoir beam L1 by D2 but re-compress the trap by ramping up the power in D1. We vary the power in the dimple beam at the end of the upward ramp between 18 mW and 42 mW, according to the mean density we want to start with. The resulting trap frequencies lie in between $2\pi \times 104$ Hz and $2\pi \times 202$ Hz in the vertical and $2\pi \times 8$ Hz and $2\pi \times 14$ Hz in the horizontal direction, respectively. The mean densities range from $5 \times 10^{12} \text{ cm}^{-3}$ to $5 \times 10^{13} \text{ cm}^{-3}$, the trap depths are on the order of $10 \mu\text{K} \times k_B$.

5.4.2 Discussion

We point to an interesting relation between our values for a_- and a_+ , which we obtained by independently fitting the data for negative and positive scattering lengths.

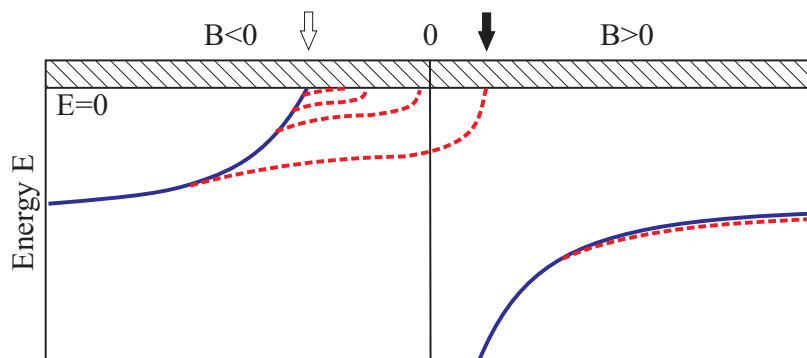


Figure 5.9: Adaptation of Efimov’s scenario to the case of Cs at low magnetic fields. The plot shows the known dimer states and possible Efimov states. The threshold ($E = 0$) is given by three free Cs atoms in the $F = 3, m_F = 3$ state and indicated by the hatched region. The solid curves depict the avoided level crossing of the $44(6,-7)$ and $33(6,-1)$ dimer states leading to the open-channel dominated Feshbach resonance at -12 G which is indicated by the empty arrow. The dashed lines represent Efimov states which would lead to the recombination behavior we observe. The triatomic Efimov resonance is located at a magnetic field strength of $B = 8$ G and indicated by the filled arrow. Beyond 17 G a possible Efimov state would run almost parallel to the dimer state because of the slow variation of the scattering length.

Theoretically a ratio of $a_+/|a_-| = 0.96$ modulo factors of 22.7 is expected [Bra06]. The experimental value $a_+/|a_-| \approx 1.25$ is quite close to this prediction, considering the full Efimov factor of 22.7 . For our experiment, however, a fundamental relation between the two parameters is not obvious, because the regions of negative and positive a are not connected through the resonant point where $a \rightarrow \pm\infty$, but are separated by a zero crossing ($a = 0$) as outlined in Sec. 5.3. The Efimov state that causes the observed resonance for $a < 0$ is thus not adiabatically connected to the dimer-atom threshold for $a > 0$. Fig. 5.9 illustrates how Efimov’s scenario might be transferred to our situation. If not an accidental coincidence, we speculate that the apparent relation between a_+ and a_- may be a further consequence of universality, since the interaction in this magnetic field region is determined by the entrance-channel dominated s -wave Feshbach resonance at -12 Gauss.

5.5 Quantitative analysis of three-body trap loss

This section describes how to extract the three-body loss coefficient L_3 from the measurement of trap loss. It extends the constant-temperature model of Sec. 5.2.1 by introducing a system of coupled differential equations allowing to describe the time evolution of the atom number $N(t)$ when three-body loss leads to heating. Also, we will give an account of data analysis and the statistical and systematic errors involved. A crucial ingredient for precise measurements of the three-body loss coefficient is the absence of two-body losses. We can exclude inelastic two-body loss because we work

5.5 Quantitative analysis of three-body trap loss

with Cs in the absolute ground state. Thus, spin-changing collisions are endothermic and energetically suppressed. We can exclude elastic loss to a high degree when the trap depth in terms of temperature is larger than the sample temperature T . To accurately determine the three-body loss coefficient, we use the model of trap loss and temperature increase as derived in Ref. [Web03c].

5.5.1 Mathematical model

To determine the three-body loss coefficient L_3 , we have recorded the temporal evolution of particle number and temperature in the trap. Due to substantial temperature increase the simple model introduced in Sec. 5.2.1 is not readily applicable but has to be extended. A detailed description of this extension has been given in [Web03a, Web03c]. In brief, the process of three-body recombination not only leads to a loss of atoms, but also induces ‘anti-evaporation’ and ‘recombination heating’. The first effect is present at any value of the scattering length a . Due to its n^3 dependence, three-body loss predominantly occurs at the trap center where atoms carry less than the average energy. The second effect is present for large positive values of a when recombination predominantly occurs into the universal dimer state.

In the recombination process, the molecular binding energy E_b is set free as kinetic energy. The molecule and the third atom receive $E_b/3$ and $2E_b/3$, respectively. Since usually E_b is large compared to the trapping potential depth, both are expelled from the trap, setting $n_l = 3$ in equation (5.18). For large positive values of a , however, the binding energy of the universal dimer state is given by $E_b = \hbar^2/(ma^2)$. Thus, at very large values of the scattering length, E_b may be below the trap depth and the third atom cannot escape. If the potential of the atom trap does not confine the molecule, the dimer is lost and $n_l = 2$. If, however, the molecule is trapped and stays within the atom cloud, it may quickly quench its high vibrational excitation in an inelastic collision with a fourth trapped atom. The large amount of energy released in this situation expels the collision partners, making $n_l = 3$. In either case, the kinetic energy of the remaining atom is distributed in the ensemble, giving rise to recombination heating. In our model, we set $n_l = 3$ for all measurements in order to simplify data analysis. The error incurred by this assumption is discussed in the following section.

Atom loss and temperature rise are modelled by the following set of two coupled non-linear differential equations

$$\frac{dN}{dt} = -\alpha N - \gamma \frac{N^3}{T^3} \quad (5.21)$$

$$\frac{dT}{dt} = \gamma \frac{N^2}{T^3} \frac{(T + T_h)}{3}. \quad (5.22)$$

Here, $\gamma = L_3(m\bar{\omega}^2/2\pi k_B)^3/\sqrt{27}$ relates to the rate of three-body loss (see also Sec. 5.2.1) and $\alpha = 1/\tau$ models the loss due to background gas collisions and off-resonant scattering. The term T_h is introduced to account for recombination heating.

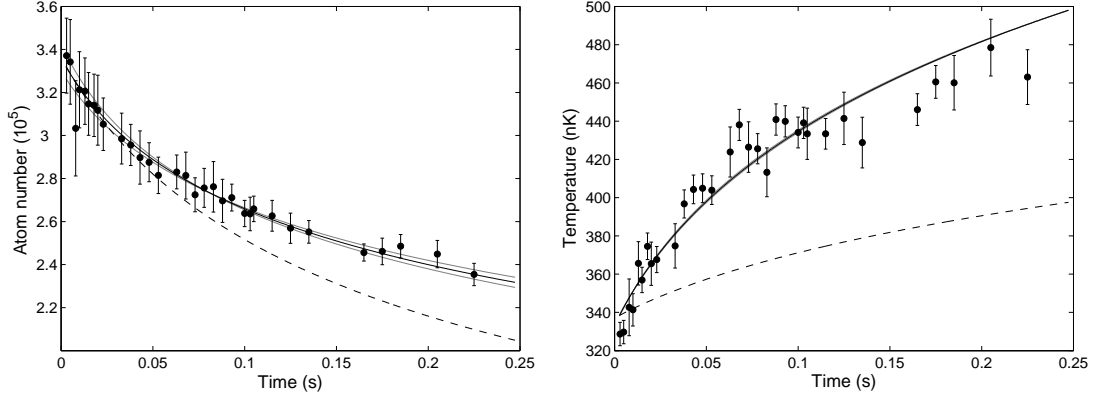


Figure 5.10: L_3 measurement at a magnetic field of 37.7 G, corresponding to $a = 747 a_0$. The plots show atom number (left) and temperature (right) as a function of trapping time. The black lines are best fits of equations 5.21 and 5.22 to the data. The grey lines indicate the variance of L_3 . The error bars are normalized such that $\xi^2 = \text{DoF}$ as is explained in the text. Using the initial conditions of the best fit, we plot Eqs. (5.23) and (5.24), which do not include recombination heating, as dashed lines. The fit gives $T_h = 914$ nK.

We used numerical solutions to this set of equations to fit our experimental data. From these fits together with measurements of the trapping parameters we obtained the rate coefficient L_3 .

Note that with vanishing T_h these equations yield the solution [Eng06]

$$\frac{T}{T_0} = \sqrt[9]{1 + \frac{3\gamma N_0}{T_0^3} \frac{1}{2\alpha} (1 - e^{-2\alpha t})} \quad (5.23)$$

$$\frac{N}{N_0} = \frac{e^{-\alpha t}}{\sqrt[3]{1 + \frac{3\gamma N_0^2}{T_0^3} \frac{1}{2\alpha} (1 - e^{-2\alpha t})}}. \quad (5.24)$$

The model above holds only if firstly two-body losses can be excluded and secondly if the ensemble is in thermal equilibrium at any given time. Regarding inelastic losses, the first condition is easily fulfilled since the energetically lowest internal hyperfine state is used in the experiment. Elastic collisions will not lead to significant evaporative loss if the trap is sufficiently deep. The second condition implies that elastic collisions are faster than three-body loss in the sense that the sample is thermal equilibrium at any given time in spite of the spatially non-uniform three-body loss. For all the measurements on the positive- a side we are well within the regime where the rate of elastic exceeds that of inelastic scattering. However, on the negative- a side for large $|a|$ but in particular on the Efimov resonance the rates of elastic and inelastic scattering are of the same order of magnitude. Thus one cannot speak of a thermal equilibrium state for the atomic ensemble.

5.5.2 Statistical error

Assuming that our measurements are subject to Gaussian statistics the best estimate of the true probability density which governs the distribution of our data is found by following the standard method of least-squares [Bev92]. The detection method is destructive and thus requires one experiment run for every single parameter variation. Our experiment provides one data point per 20 s. This time is determined by the time required for MOT loading and evaporation. With this rate we cannot collect enough data to assign statistically sound uncertainties to each measurement outcome. In order to calculate the variances of the parameters, we take the best estimate of the underlying probability density for the true one. This procedure allows no goodness-of-fit estimate. The best fit is found by minimizing $\xi^2 = \sum_{i=1}^N ((y_i - f(t_i))/\Delta y_i)^2$ [Bev92]. Here, the y_i represent our measured atom number and temperature at time t_i , $f(t_i)$ is the solution of (5.21) and (5.22), and Δy_i is a weight derived from the temperature measurements. For one single temperature measurement, at least three different time-of-flight expansion pictures are taken. In case of atom numbers, Δy_i is simply the arithmetic mean, whereas for temperatures, Δy_i is the temperature variance resulting from the error in determining the cloud widths which is known from other measurements. Note that ξ^2 is not equivalent with the commonly used χ^2 , the difference being that Δy_i does not represent the one- σ standard deviation. Having minimized ξ^2 , the Δy_i are scaled such that ξ^2 equals the number of degrees of freedom (DoF). The variances are then found by calculating the error matrix or, alternatively, by varying one parameter up and down, respectively, to the point where ξ^2 is increased by one, while optimizing the other parameters [Bev92]. Both methods yield similar estimates of the variance of L_3 , which is found to lie typically around 10% and in some cases can reach 50%.

Systematic effects and calibration uncertainty

Depending on trap characteristics, systematic effects differ in origin and impact on the data. An uncertainty of 10% in atom number calibration is common to all data sets. As mentioned earlier in this section, we connect the three-body loss rate coefficient L_3 to α_{rec} by $L_3 = 3\alpha_{rec}$ for all scattering lengths, setting $n_l = 3$ in equation (5.18). Thus, we simplify the fit of the analytic theory to the experimental data at the cost of an inaccuracy which lies well within the uncertainty caused by other systematic effects.

One source of systematic uncertainty is incurred by the two CO₂ lasers. The cooling fluid for the laser heads is temperature-stabilized to within 20 mK. The emitted light is single-mode single-frequency in character but displays a residual slow mode drift in spite of the temperature control. The laser beams form interference patterns with back reflected light, causing corrugations in the light potential, as mentioned in Sec. 4.5. This gives rise to an uncertainty of up to 25% in the trap frequencies. Together with the atom number calibration uncertainty, we conservatively estimate a factor of 2.5 in L_3 for trap setups using CO₂ light. This affects all data taken at an initial temperature of 200 nK.

For data taken with 10 nK samples the inclination of the optical table is a source of systematic error due to the shallow optical trapping potentials used for the BEC production. With a trap depth of less than $100 \text{ nK} \times k_B$, a misalignment of 1 mrad would already spill the trap. Smaller misalignments prove less disastrous but can cause the atom cloud to sample the non-harmonic regions of the light potential. In such a case the actual atom number density is lower than the measured trap frequencies and the measured atom number imply. Over-estimating the atom number density leads to under-estimating L_3 in measurements of $L_3 \langle n^2 \rangle N$. Due to temperature fluctuations in the lab acting on table inclination via its air suspension, the variation of optical table inclination leads to day-to-day fluctuations of L_3 of up to a factor of two.

As indicated in Sec. 5.5.1, the requirement of a thermalised sample is not strictly fulfilled on the Efimov resonance. Taking a typical 10 nK atom cloud with an initial mean density of $5 \times 10^{11} \text{ cm}^{-3}$, the ratio of elastic to inelastic collisions approaches unity in the resonance region around $a = 850a_0$ where L_3 exceeds $2 \times 10^{-22} \text{ cm}^6/\text{s}$. We expect to have underestimated the three-body loss rates on resonance.

For greater clarity we have averaged L_3 coefficients of the same initial temperature of different scattering lengths in Fig. 5.8 if the difference in scattering length was less than $20 a_0$. Again, we can give no statistically sound variance to each data bin. Except for the 10 nK data, the error resulting from quadratically adding the statistical error and the mean deviation in each bin is indicated by the error bars in Fig. 5.8. In order to provide a more realistic impression of the 10 nK-data quality, we have quadratically added the mean deviation of all 10 nK bins to the individual error of the data in each bin.

Note that these error bars do not include the calibration uncertainty inherent to the imaging system which affects all data, nor the error caused by the CO_2 lasers which applies to the 200 nK data only.

CHAPTER 6

Four-body interactions: Dimer-dimer collisions and the observation of Feshbach-like resonances

Little is known about the four-body problem. Numerical solutions can be found only within certain limits. The problem of four interacting particles is formally described by generalizations of the Faddeev equations to the N -body problem.

Numerical solutions to the resulting equations have been found in the case of the bound state problem for four nucleons interacting through a potential, see reference [Bra06] and references therein. The ground and excited state energies of ${}^4\text{He}_N$ clusters with $N \leq 10$ are calculable. Universal properties of four bosons with short-ranged interactions have been studied [Pla04, Yam06]. It is understood that in the case of identical bosons, universal four-body properties must depend on the two-body scattering length a and a three-body parameter which relates to the non-universal binding energy of the first Efimov state. The question if an additional four-body parameter is required is still undecided [Bra06]. There is no Efimov effect for four or more particles [Ama73] in the sense that there is no accumulation point of N -body bound states as the binding energy of the $(N - 1)$ -body subsystem is tuned to zero. There are, however, Efimov-like tetramer states in the dimer-atom-atom system [Bra06].

The low-energy scattering among Feshbach molecules is an experimentally accessible four-body process. Its description involves a multitude of scattering channels, including reactive scattering, collision-induced dissociation and replacement chemical reactions and is basically intractable up to now apart from two exceptions. For the case of four fermions at large atomic scattering length a forming two universal dimers, the dimer scattering length a_{DD} could be shown to obey $a_{DD} = 0.6a$ [Pet04]. If these dimers can form deeply bound diatomic molecules through relaxation during dimer-dimer collisions, the rate constant β_{DD} for this process is shown to obey a universal scaling $\beta_{DD} \propto (a)^{-3.5} \hbar a/m$ [Pet04]. The case of inelastic collisions among universal or non-universal dimers Feshbach-associated from bosonic atoms into an highly excited vibrational state is unknown territory. The experiment tells us that relaxation into deeply bound states during dimer-dimer collisions lead to rapid trap loss with two-body rate coefficients as large as several 10^{-10} cm³/s [Muk04, Chi05, Tho05a, Sya06]. In the universal regime these high rates might be suppressed because the Franck-Condon overlap between the universal halo state with a size proportional to a and the deeply bound states with (constant) sizes proportional to the range of interaction is minimized in the limit of $a \rightarrow \infty$.

A first small step towards exploring dimer-dimer interactions is readily given by

observing the dependence of loss from a trapped molecular vapor on the magnetic field and the internal quantum state. Sec. 6.1 of this chapter is concerned with the preparation of pure samples of ultracold Cs₂ dimers in the reservoir trap. In Sec. 6.2 measurements of trap loss as a function of the magnetic field strength are presented. The measurements show resonance phenomena in trap loss which hint at the presence of a magnetically tuneable Cs₄ tetramer state near the dimer-dimer scattering continuum.

6.1 Preparation of pure samples of trapped ultracold Cs₂ dimers

As outlined in Sec. 3.3, Cs in the $F = 3, m_F = 3$ state offers a multitude of rather narrow Feshbach resonances at magnetic fields up to 150 G which can be used for Feshbach association. In our first successful experiments at Feshbach association we used the 19.8 G resonance [Her03]. We have performed detailed studies on the association process and possible loss mechanisms at this resonance [Mar05] in order to optimize the conversion efficiency. Since then we have performed a number of experiments of which

- Feshbach-association using other Feshbach resonances,
- the coherent transfer of molecules initially in the state used for Feshbach association to other internal states by Landau-Zener tunneling [Lan32, Zen32] through avoided dimer level crossings,
- and micro-wave spectroscopy of dimers in various internal states

will be addressed in the thesis of Michael Mark [Mar07a].

For the present thesis, only Cs dimers created via the 19.8 G resonance will be relevant. The remainder of this section is devoted to the description of Feshbach association via the the 19.8 G resonance, both in the reservoir trap and in free space.

6.1.1 Molecule production

For creation of the molecules we use the closed-channel dominated resonance at 19.84 G, as mentioned above. For the Zeeman diagram of the corresponding molecular state and its neighbors, see Fig. 6.1. The state has a magnetic moment of $\mu = 0.93 \mu\text{B}$ with a small magnetic field dependence [Jul03], and the resonance width is calculated to 5 mG [Jul03].

We found the following parameters to optimize the conversion efficiency. Starting point is a trapped atomic BEC as described in Sec. 4.6. The magnetic field is swept across the resonance from a higher field value (19.88 G) with a constant rate of typically 48 G/s to a final value of 19.74 G. The duration of the sweep is 6 ms. Immediately

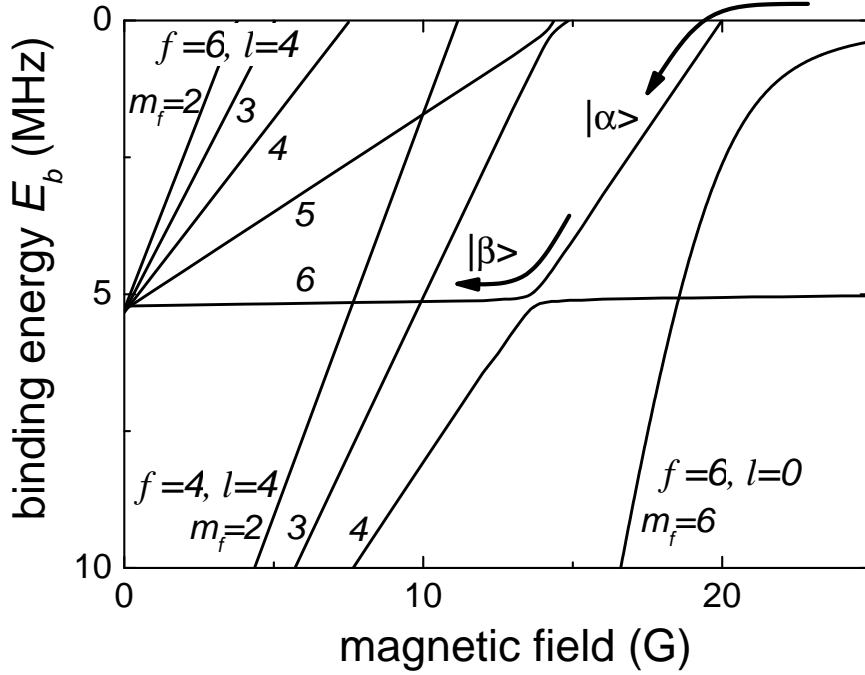


Figure 6.1: Zeeman diagram of the most weakly bound molecular states that couple to the atomic scattering continuum. The data is based on calculations done at NIST [Chi04b]. The dissociation threshold, given by zero binding energy $E_b = 0$, is associated with two Cs atoms in the lowest ground state sublevel $F = 3, m_F = 3$. As a result of the strong indirect spin-spin interaction of Cs atoms (see Sec. 3.3), coupling to molecular states with large orbital angular momentum leads to the complexity of the energy structure. The arrow mark the paths to the molecular states we explore in this work. Included are only molecular states which can couple to the continuum via Feshbach couplings up to g-wave interaction ($l \leq 4, m_f + m_l = 6$ and $m_f \geq 2$). Stable trapping in states $|\alpha\rangle$ and $|\beta\rangle$ is achieved in the reservoir trap.

after the end of the ramp we switch off the dimple trap. Simultaneously, we lower the magnetic field by jumping to a fixed hold field of 17 G to reduce the admixture of the scattering state. Thus, under the influence of the levitation field, the molecules are automatically separated from the atoms due to the difference in the magnetic moment to mass ratios. Using these parameters, the conversion efficiency is maximized for our setup and approaches 12%.

Due to the small resonance width and the magnetic gradient field, the resonance condition is fulfilled only for a certain horizontal slice, $\sim 2 \mu\text{m}$ in width, that is moved through the atomic cloud from below during the sweep. Thus, a vertical velocity spread is imparted across the molecular cloud as gravity accelerates the molecules. Consequently, we measure different expansion energies for the vertical ($\frac{1}{2}k_B \times 40 \text{ nK}$) and horizontal ($\frac{1}{2}k_B \times 2 \text{ nK}$) directions. With the gradient field and gravity acting on the molecules, the net downward acceleration amounts to 0.38 g. Also, the presence of

the gradient field has the disadvantage of inducing a center of mass motion for the resulting molecular cloud even if the gradient is adjusted during the Feshbach sweep in order to levitate the molecules. In trapping experiments, both effects lead to heating of the molecular samples and a reduction of phase space density, see sec. 6.1.3.

To avoid the levitation field during Feshbach association, we adiabatically re-compress the dimple trap after BEC production. With a power of 42 mW in dimple beam D1, we can remove the gradient field within 180 ms without exciting the BEC. We then release the BEC from the trap and experiment on the falling cloud. Instead of the Stern-Gerlach separation technique we use a resonant push beam to remove the remaining atoms. We illuminate the mixed cloud with the imaging beam for 50 μ s together with the MOT re-pumping light. For a detailed study of the dependence of the molecular expansion energy and the conversion efficiency on the initial condensate mean field energy, the reader is referred to [Her05].

6.1.2 Molecule detection

We do not image the dimers directly. Rather, we break the molecules and image the resulting atomic cloud. To do so, we apply a fast magnetic field ramp over the Feshbach resonance. Thereby, the dimers are diabatically swept over the avoided crossing and carried above the atomic scattering continuum. Here, the molecules spontaneously decay into correlated pairs of free atoms with typical decay rates on the order of 100 kHz. The maximum attainable ramp speed is limited by eddy currents in the vacuum chamber and depends on the pair of coils which is used for dissociation. In fact, we just step the current feeding the coils for maximum ramp speeds. For the Feshbach field coils in the aluminium housing, the magnetic field lag limits the maximum ramp speed to about 50 kG/s, whereas with the single fast coil we achieve up to 10^7 G/s. Within this thesis, however, molecule dissociation is performed solely by the Feshbach field coils.

Due to energy conservation, the kinetic energy E of a single reconverted atom resulting from molecule dissociation at given magnetic field strength B is simply $E = \Delta\mu(B - B_{\text{res}})/2$, with B_{res} the position of the resonance and $\Delta\mu$ the difference of the molecular and atomic magnetic moment. Above the resonance, the dimers decay according to Fermi's golden rule [Muk04]. For a linear magnetic field sweep, the probability density for the velocity distribution of a reconverted atomic ensemble is inferred accordingly [Muk04, Dür04b]. This distribution is not Gaussian and provides no analytical expression for the corresponding time-of-flight absorption images. Nevertheless, we fit the atomic cloud resulting from molecule dissociation and a subsequent ballistic expansion with a Gaussian that corresponds to the velocity distribution of a thermal cloud [Web03a]. The mean kinetic energy $\langle E \rangle$ inferred from such a fit has been shown to be a factor of ~ 1.18 too large [Dür04b]. This systematic error lies well within the statistical uncertainty of our time-of-flight measurements and we therefore do not correct for this error. Using the Feshbach field coils (windings in coils (B) in Fig. 4.2) for dissociation, we observe an expansion energy of $\sim 1 \mu\text{K}$ on the resonance at 19.84 G. For this measurement, the electrical current feeding the coils is stepped

6.1 Preparation of pure samples of trapped ultracold Cs₂ dimers

from 2.7 A to 3.6 A, corresponding to 16.5 and 22 G, respectively.

More specifically, the mean kinetic energy $\langle E \rangle$ depends on the magnetic field ramp speed \dot{B} and the coupling matrix element V_{ma} as $\langle E \rangle \propto (\Delta\mu\dot{B}/|V_{ma}|^2)^{2/3}$ [Muk04]. This dependence can be used to distinguish different molecular states within a mixture or superposition by means of a single dissociation ramp. For example, we exploit this effect to determine the contributions to a coherent superposition of the $|f = 6, m_f = 3; l = 8, m_l = 3\rangle$ and the $|f = 4, m_f = 2; l = 4, m_l = 4\rangle$ state [Her05, Mar07a, Kra]. The former hits the atomic scattering threshold at 16.5 G and features an expansion energy which is more than an order of magnitude higher than the latter which is dissociated via the 19.84 G resonance, see previous paragraph.

The molecules do not necessarily decay into an atomic s-wave orbital angular momentum state. Decay into a superposition of several atomic partial waves becomes possible if the dissociation energy $\Delta\mu(B - B_{\text{res}})$ is sufficient to overcome the respective centrifugal barrier, or via tunneling through a shape resonance [Vol05]. The relative phases are determined by the ramp speed with which the molecules are dragged above the scattering continuum [Dür05, Vol05]. For example, the atomic cloud resulting from the dissociation of the aforementioned $|f = 6, m_f = 3; l = 8, m_l = 3\rangle$ state is well fit assuming a superposition of the $Y_{0,0}$ (s-wave) and the $Y_{2,0}$ (d-wave) spherical harmonics.

During the association and dissociation processes, the quantity $m_f + m_l$ is conserved but not the atomic F and L quantum numbers. In terms of molecular quantum numbers, the initial atomic scattering state is described as $|f = 6, m_f = 6; l = 0, m_l = 0\rangle$. The condition for accessible molecular dimer states thus reads $m_f + m_l = 6$. Consequently, since $m_f = 6$ for our reconverted atoms, various partial waves with (an even) $l \neq 0$ can be populated during dissociation as long as the corresponding magnetic projection quantum number m_l equals zero.

6.1.3 Cesium dimers and the reservoir trap

This section highlights how we trap our molecules in the reservoir trap. Via the necessary magnetic field gradient, this trapping scheme depends on the magnetic moment of the dimers, which undergoes strong variations as the magnetic field strength is changed. The relevant molecular energy structure is shown in Fig. 6.1.

As outlined before, we start our experiments with an essentially pure atomic BEC in the dimple trap operating at 1064 nm. The BEC has been described previously in Sec. 4.6. For molecular samples, this laser light leads to rapid loss through optical pumping. Therefore, we load the BEC into the reservoir trap. The corrugation of the CO₂ light and the beam walk caused by ramping the rf power in the CO₂-AO's prevent an adiabatic transfer. We are left with typically 2.0×10^5 atoms in the reservoir trap, of which around 30 % are in the condensed state. We measure a peak atomic density of around $5 \times 10^{13} \text{ cm}^{-3}$.

Trap loading

To create molecules via the 19.8 G resonance for subsequent trapping in the reservoir trap, we adjust the parameters of Sec. 6.1.1. We term the corresponding molecular state $|\alpha\rangle \equiv |f = 4, m_f = 4; l = 4, m_l = 2\rangle$. We ramp the magnetic field from 20.0 to 19.5 G in 8 ms and then quickly change the field to 17 G to decouple the molecules from the atoms. Simultaneously, we ramp the magnetic field gradient from 31 to 50 G/cm. The latter field gradient levitates the molecules and removes the atoms from the trap within 3 ms, leaving a pure sample of typically 10^4 molecules in the reservoir trap. Due to

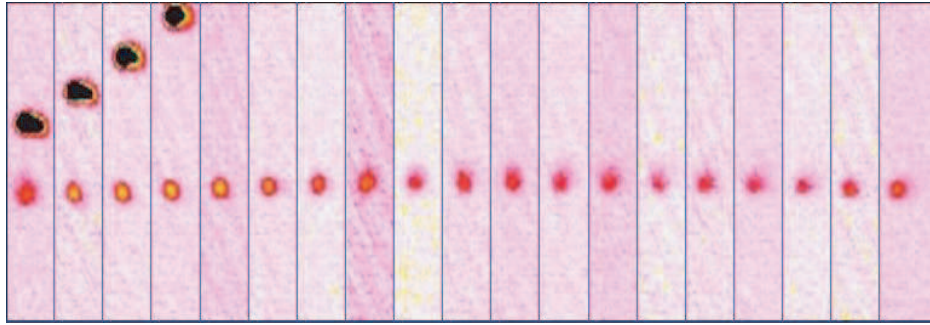


Figure 6.2: Molecules in the reservoir trap. After the Feshbach ramp the molecules are trapped in the CO_2 light in combination with magnetic levitation, while the atomic BEC is accelerated upwards. A small wobbling in the vertical direction due to a temporary gradient mismatch during the Feshbach ramp can be anticipated. The leftmost picture is taken 8 ms after the ramp, the pictures are spaced 2 ms apart.

the finite ramp time and the small resonance width, the magnetic field gradient will deviate from the exact levitation condition during the Feshbach ramps. This leads to a small momentum kick, seen as vertical oscillation in Fig. 6.2, and in consequence to trap heating. The ramp parameters are in fact a compromise between association efficiency and trap excitation. After ~ 100 ms the oscillations are damped out, and the sample is thermalised at a temperature of 250 nK with a peak density of $5 \times 10^{10} \text{ cm}^{-3}$ and a phase space density of somewhere around 10^{-2} and 10^{-3} .

Below 19.84 G, the state $|\alpha\rangle$ is stable against spontaneous dissociation and acquires larger binding energies at lower magnetic fields, see Fig. 6.1. At about 14 G, an avoided crossing to another state $\beta \equiv |f = 6, m_f = 6; l = 4, m_l = 0\rangle$ is induced by the indirect spin-spin coupling. This state features a similar magnetic moment as the scattering continuum. We follow the upper branch of the avoided crossing adiabatically. To stably trap molecules along this path, we need to know the precise value of the molecular magnetic moment as a function of the magnetic field strength.

Measurement of the molecular magnetic moment

The equilibrium position of molecular cloud is a sensitive probe of the imbalance of the magnetic force and gravity. Given a small vertical displacement from the trap cen-

6.1 Preparation of pure samples of trapped ultracold Cs₂ dimers

ter δz for a local magnetic field B and a field gradient B' , the magnetic moment is then $\mu_B = (2m\omega^2\delta z + 2mg)/B'$. Here, $2m$ is the molecular mass, and g is the gravitational acceleration. Another method of determining the magnetic moment relies on a measurement of the residual acceleration of the molecular cloud after release into free space with near-perfect levitation [Her03]. We use this method to independently measure μ_B at 17 G and at 12.08 G. A small vertical displacement from the quadrupole field zero induces a dependence of the local magnetic field at the trap center on the magnetic field gradient. We have characterized this feature by rf calibration of the magnetic field using atomic samples.

The gravitational force on the molecules outreaches that caused by the CO₂ light by far. Thus, the range where the cloud displacement depends linearly on levitation imbalance, i.e. where the harmonic approximation of the light potential is valid, is severely limited. As it turns out, the trap works stably only if the levitation imbalance does not exceed $\sim 8\%$. Before measuring the displacement, we allow 500 ms for equilibration after adjustment of the magnetic fields.

Between 19.8 G and 14 G, a magnetic field gradient of 50 G/cm keeps the molecules near the trap center. We scan this region by tuning the magnetic field within 60 ms to a desired value. The magnetic moment decreases slowly from $0.98 \mu_B$ to $0.93 \mu_B$ as the magnetic field lowered from 19.8 G, see Fig. 6.3. For magnetic fields below ~ 14 G, the magnetic moment's dramatic change requires an adjustment of the field gradient. We stepwise realize this adjustment by subsequently appending small ramps of the field gradient to lower values, accompanied by simultaneous ramps of the magnetic field. In total, we need five of these steps to cover the region below 14 G, given that each step produces sufficient overlap with data from neighboring steps. Below ~ 13 G, a field gradient of 33 G/cm approximately levitates the molecules. The magnetic moment levels off at $1.5 \mu_B$, see Fig. 6.3.

This behavior is readily explained by the avoided crossing at 13.6 G (Figs. 6.1 and 6.3), which transfers the molecules from state $|\alpha\rangle$ with $\mu \approx 0.9\mu_B$ to $|\beta\rangle$ with $\mu \approx 1.5\mu_B$. Below 11.5 G, a new avoided crossing to a very weakly coupled $l = 8$ state occurs. In the measurement depicted in Fig. 6.3, we observe fast loss of the molecules. At that time, we could not generate a sufficient gradient field to support the molecules in this new state against gravity. Since then, we have modified the setup so as to stably trap by CO₂-laser light alone in the elliptic trap, and also to generate higher magnetic field gradients.

Due to some unidentified systematic error, the displacement method yields a value of $1.43(1) \mu_B$ at 12.08 G, whereas the residual acceleration when the cloud is released into free space indicates a value of $1.49(1) \mu_B$. Using another value established by the acceleration method at 17 G [Her03], we correct the displacement data by adding a linear offset such as to match the acceleration data.

By integrating the measured magnetic moment data, we can derive the molecular binding energy. The integration constant is fixed by the fact that the binding energy is zero at the atomic Feshbach resonance at 19.84 G. The result shown in the inset of Fig. 6.3 gives good agreement with the theoretical calculation within the energy

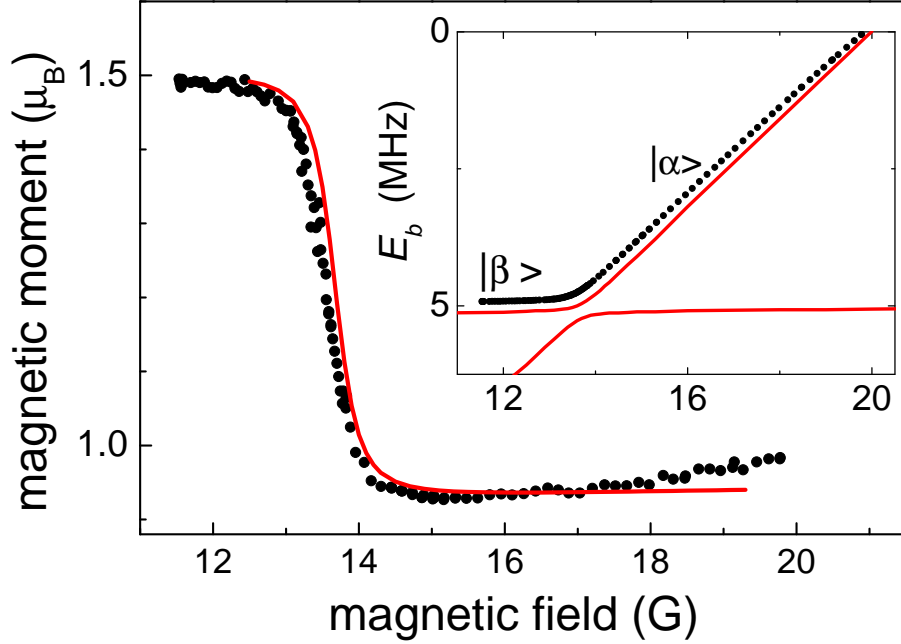


Figure 6.3: Magnetic moment of the Cs dimers. The measured magnetic moment (dots) is compared to the NIST calculation (solid line). The fast change at 13.6 G is associated with an avoided crossing between state $|\alpha\rangle$ and $|\beta\rangle$. In the inset, we derive the molecular binding energy (dots) by integrating the magnetic moment. Also, the NIST calculation of the binding energies for both branches of the avoided crossing is shown (solid line).

uncertainty of 0.25 MHz. By fitting our binding energies to a simple avoided crossing model, we determine the crossing position to be 13.55(4) G and the coupling strength to be $h \times 150(10)$ kHz.

6.2 Observation of resonance phenomena in trap loss

We measure the inelastic collision loss after a trapping time of 300 ms, see Fig. 6.4. The measurement consists of three different data sets, corresponding to states $|\alpha\rangle$ ($14 \text{ G} < B < 19.8 \text{ G}$) and $|\beta\rangle$ ($11.5 \text{ G} < B < 13.6 \text{ G}$) and the avoided crossing region.

For molecules in state $|\alpha\rangle$ the fractional loss is about 40 %. In this molecular state, we do not observe any strong magnetic field dependance. When the magnetic field is tuned near the Feshbach resonance at 19.8 G, molecules dissociate into free atoms, which leave the trap.

In state $|\beta\rangle$, the behavior is different. We observe a weaker background loss of $\sim 20 \%$ and two pronounced resonances with a fractional loss of up to 60 %. An expanded view in the inset of Fig. 6.4 shows that the double-peak structure can be well fit by a sum of two Lorentzian profiles. From the fit, we determine the resonance

6.2 Observation of resonance phenomena in trap loss

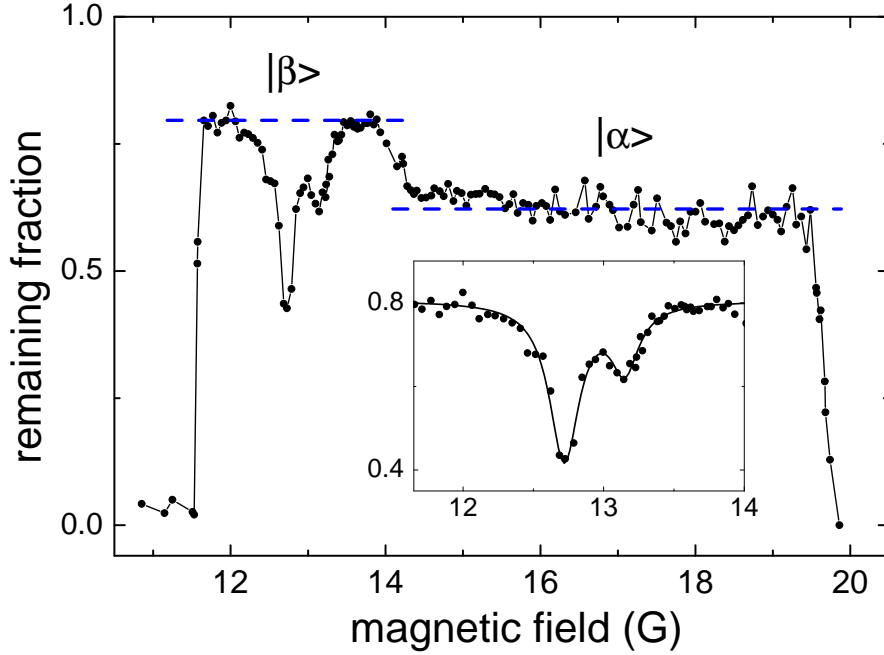


Figure 6.4: Remaining fraction of optically trapped molecules after a storage time of 300 ms. Initially, there are 11000 molecules at a peak density of $6 \times 10^{10} \text{ cm}^3/\text{s}$ and a temperature 250 nK. The dashed lines mark the background loss rates in states $|\alpha\rangle$ and $|\beta\rangle$. The two loss resonances for $|\beta\rangle$ are fit by a sum of two Lorentzian profiles and magnified in the inset.

positions to be 12.72(1) G and 13.52(2) G, with full width of 0.25 G and 0.24 G, respectively. Due to the field gradient the magnetic field inhomogeneity across the sample amounts to 0.15 G in the state $|\beta\rangle$. This suggests that the intrinsic widths of these resonances are less than the observed values.

The observed resonances cannot be explained by single-molecule effects. The Cs_2 energy structure is well known up to partial waves of $l = 12$ and does not support any such scenario. Beyond single-molecule effects, the observed resonance structure suggests that bound states of two Cs_2 molecules, or Cs_4 tetramer states, are tuned into resonance with the scattering state of the dimers and induce Feshbach-like couplings to inelastic decay channels. Other possible decay channels, e.g. coupling to a trimer and a free atom or a dimer and two free atoms, should result in a threshold behavior in the loss spectrum rather than the observed resonance feature.

To confirm that the loss is indeed due to collisions among Cs_2 molecules, we observe the time dependence of molecule loss from the levitation trap. Starting with 11000 molecules prepared at different magnetic fields, we record the molecule number after various wait times, as shown in Fig. 6.5. Three magnetic fields are chosen here: 15.4 G where the molecules are in state $|\alpha\rangle$, 12.1 G where the molecules are in state $|\beta\rangle$ and away from resonance, and 12.7 G where the molecules are on the strong reso-

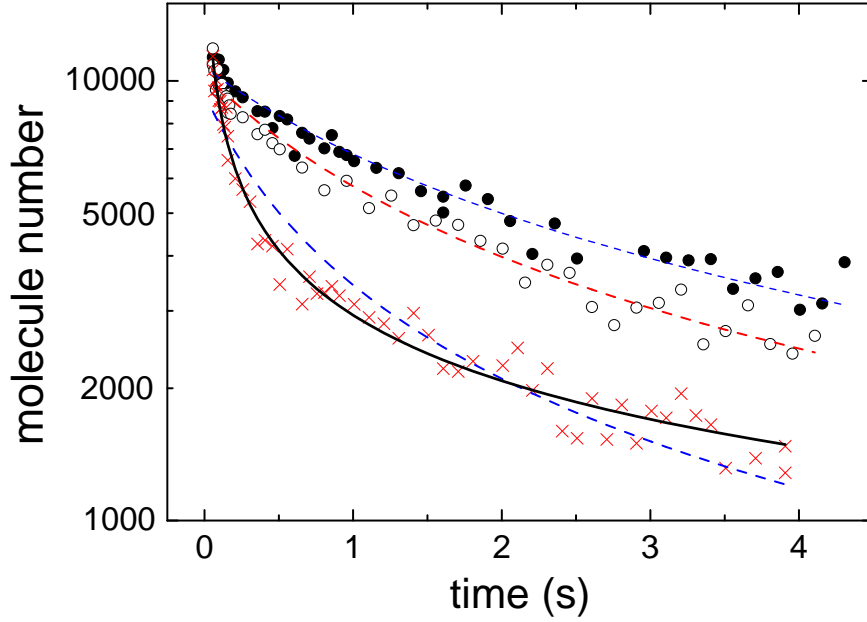


Figure 6.5: Time evolution of the molecule number in the levitation trap for molecules in state $|\alpha\rangle$ at 15.4 G (open circles), in state $|\beta\rangle$ at 12.1 G (off resonance, solid circles) and at 12.7 G (on resonance, crosses). Fits based on two-body loss (dashed lines) work well for 15.4 and 12.1 G. A fit based on three-body loss (solid line) works better for 12.7 G.

nance, see Fig. 6.4. The number of trapped molecules shows a nonexponential decay, which is a clear signature of density-dependent processes.

To further investigate the underlying molecular collision processes, we model the loss based on the two-body or three-body loss equation of Sec. 5.2.1. In our setup, the one-body decay rate is limited by background gas collisions to $\alpha = 1/180 \text{ s}^{-1}$. We fit the measured molecule numbers to Eqs. (5.16) and (5.17), see Fig. 6.5. For 15.4 and 12.1 G, we find that the two-body loss equation Eq. (5.16) provides excellent fits. The two-body loss rate coefficients are $L_2 = 5 \times 10^{-11} \text{ cm}^3/\text{s}$ at 15.4 G and $L_2 = 3 \times 10^{-11} \text{ cm}^3/\text{s}$ at 12.1 G. We cannot, however, rule out the possibility that three-body processes also play a role.

At 12.7 G, where the molecules are on the strong resonance, we find that the three-body equation Eq. (5.17) provides a better fit than the two-body equation. The fit gives a three-body loss coefficient of $L_3 = 6 \times 10^{-20} \text{ cm}^6/\text{s}$. This value, however, is much too high compared to the three-body unitarity limit of $844\hbar^5/(m^3k_B^2T^2) = 2 \times 10^{-23} \text{ cm}^6/\text{s}$. One alternative explanation is that on resonance, the fast two-body decay might leave the molecules insufficient time to reach thermal equilibrium. By fitting only the first 200 ms with the two-body loss model, we determine the loss coefficient to be $L_2 = 2 \times 10^{-10} \text{ cm}^3/\text{s}$, which is indeed close to the two-body unitarity limit of $4 \times 10^{-10} \text{ cm}^3/\text{s}$.

CHAPTER 7

Outlook

The three-body recombination measurements presented in this thesis are a first step towards exploring few-body interactions in ultracold gases. This chapter gives an overview of possible measurements for further studies on Efimov physics in ultracold atomic gases and mixtures of atoms and dimers and dimers and dimers with emphasis on using Cs atoms and dimers in such measurements. Preliminary results from ongoing measurements on atom-dimer mixtures are presented. Possible schemes for direct detection and controlled association of Efimov states and the limitations of detecting Efimov-related scattering phenomena in mono-atomic gases are outlined. Ultracold atomic two-species mixtures might be useful to overcome the limitations associated with mono-atomic gases.

Efimov-related scattering effects in atom-dimer and dimer-dimer collisions

Efimov physics is expected to be visible in *atom-dimer collisions* in the universal regime for positive scattering lengths [Efi79, Bra06]. As outlined in Sec. 5.2, the presence of Efimov states resonantly enhances the scattering cross section for atom-dimer collisions according to Efimov's radial law [Efi79]. Fig.7.1 illustrates the resonance positions using Efimov's scenario which is described in Sec. 5.1.4. The resonant enhancement occurs when Efimov states connect to the universal dimer state for positive scattering length $a = a_{ad}, 22.7a_{ad}, \dots$ and is indicated by the arrows in Fig.7.1. From theory [Bra03, Bra06] one expects $a_- = -0.97a_{ad}$ in the limit $\ell/|a| \rightarrow 0$. Here $a = a_-, 22.7a_- \dots$ are the values of the scattering length for which there are Efimov trimers at the three-atom threshold.

The Efimov effect can also play a role for *dimer-dimer collisions* in the universal regime when two colliding dimers resonantly couple to an Efimov trimer and a free atom. Such couplings might occur when the Efimov trimers intersect the dimer-dimer scattering threshold for $a > 0$. Fig. 7.2 illustrates the intersection points. Note that the threshold $E = 0$ is given by *four* atoms (A+A+A+A). The lines that represent Efimov trimers in the Efimov scenario of Fig. 7.1 now show Efimov trimers and one free atom (ET+A). The grey parabola represents the universal dimer state and two free atoms (D+A+A) and the black parabola shows the scattering threshold of two universal dimers (D+D). The arrows mark the positions of possible dimer-dimer scattering resonances induced by Efimov states. Possible four-body bound states are not shown. In principle dimer-dimer interactions are four-body processes and are largely unknown. In the universal regime, however, four-body bound states due to an Efimov-like effect

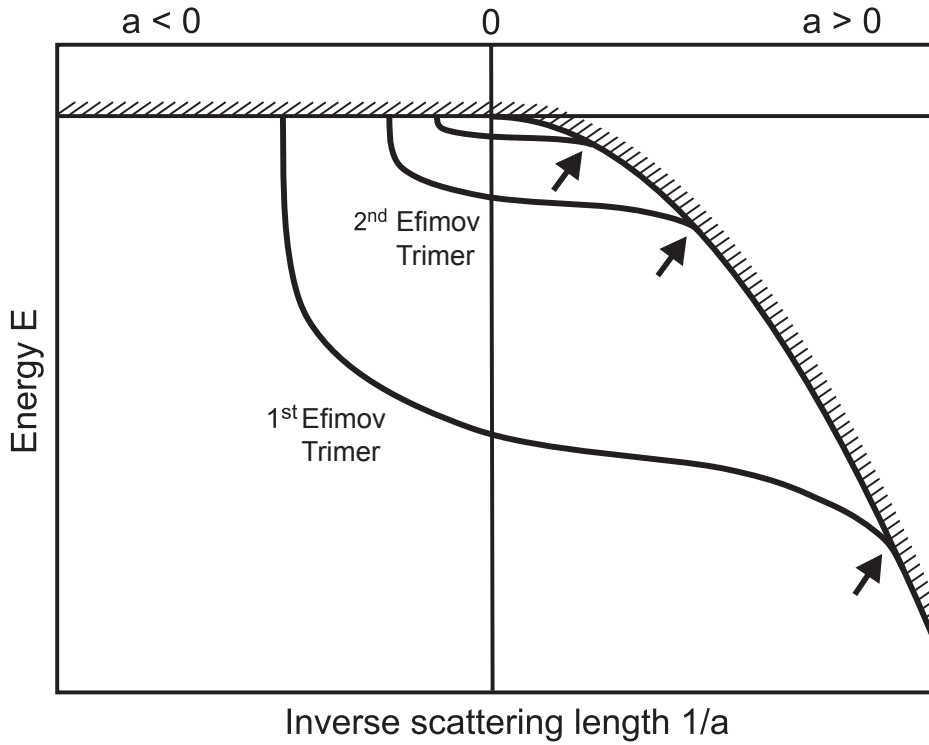


Figure 7.1: Efimov’s scenario as described in Sec. 5.1.4. Resonant enhancement of the atom-dimer collision cross section is expected according to Efimov’s radial law [Efi79] where the Efimov trimers connect to the universal dimer state (indicated by the arrows).

for the dimer-atom-atom system at the points where the (ET+A)-lines connect to the (D+A+A)-parabola are expected [Bra06].

Universal dimer state in Cesium

Experiments aiming at the detection of Efimov-related scattering effects in atom-dimer and dimer-dimer collisions require molecules in a universal dimer state. In a certain magnetic field region such a dimer state exists in Cs.

In Cs, the first dimer state below the $(F_3, m_F = 3) \times (F_3, m_F = 3)$ scattering continuum runs parallel to threshold with a binding energy of ~ 10 kHz for magnetic field strengths B above 30 G. For an illustration of this state see Fig. 3.2 in Sec. 3.3. It is labeled $F_1 F_2(f, \nu) = 33(6, -1)$ and causes a background scattering length of $\sim 2000 a_0$ away from any Feshbach resonances. Dimers in the $33(6, -1)$ -state for $B > 30$ G are universal in the sense that their binding energy follows the universal a^{-2} -scaling. For $30 < B < 50$ G this scaling has been established using micro-wave spectroscopy [Mar07a]. Thus the state $33(6, -1)$ is a promising candidate for observing universal effects in atom-dimer and dimer-dimer scattering. The production of molecules in this state at our experiment is described in Ref. [Mar07a].

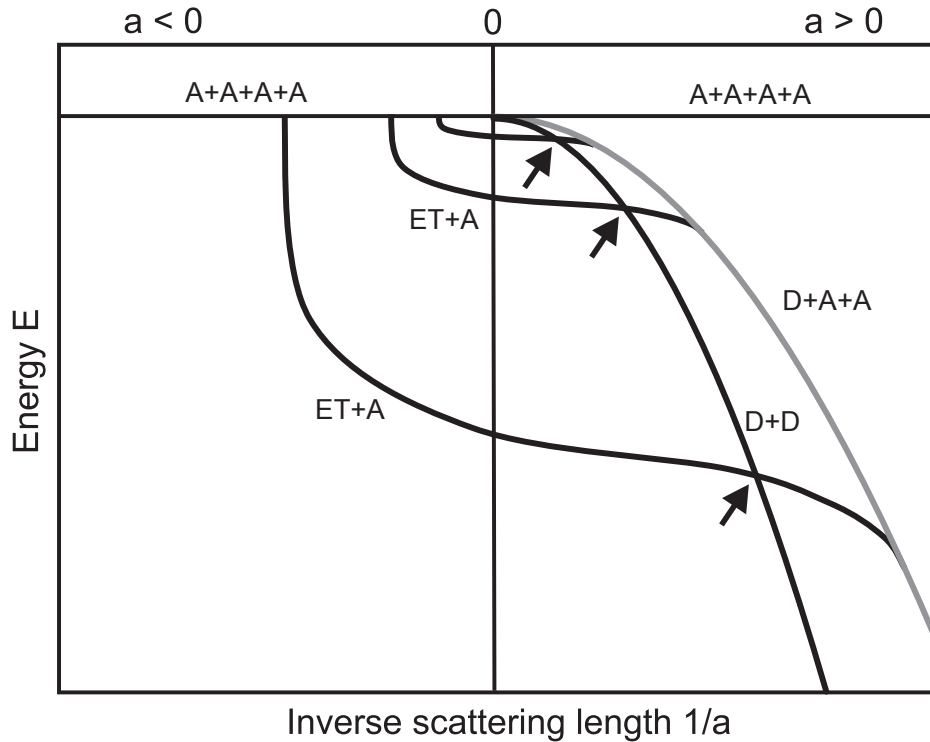


Figure 7.2: Extension of Efimov’s scenario to the case of four atoms. The known universal two-body and three-body bound states are shown. Four-body bound states which might also exist are not depicted. The threshold $E = 0$ is given by four atoms (A+A+A+A). (ET+A): Efimov trimer and one free atom. The grey parabola represents the universal dimer state and two free atoms (D+A+A) and the black parabola shows the scattering threshold of two universal dimers (D+D). The arrows mark the positions of possible dimer-dimer scattering resonances induced by Efimov states.

In ongoing experiments, the atom-dimer collision rate constant is determined. A mixture of atoms and $33(6, -1)$ -dimers is held in an optical trap similar to the elliptic trap without a magnetic field gradient [Mar07a]. Assuming negligible background losses and dimer-dimer collision rates, the atom-dimer collision rate constant is measured via the $1/e$ -decay time of the number of trapped dimers. First results are shown in Fig. 7.3. A significant enhancement of the atom-dimer collision rate is found around a magnetic field value of 25 G which corresponds to $\sim 400 a_0$. From our three-body loss measurements, however, one expects an atom-dimer resonance to appear at $1200 a_0$. The discrepancy is not yet understood but might be due to the fact that the dimers are not strictly in the universal regime ($a \gg \ell$) since $400 a_0 \approx 4\ell$.

Apart from Efimov-related effects, the dimer-dimer system in the universal regime might exhibit a suppression of de-exciting collisions at large scattering lengths. The size of universal dimer halo state is proportional to the atomic scattering length [Köh06]. Quenching collisions might be suppressed at higher values of a due to a

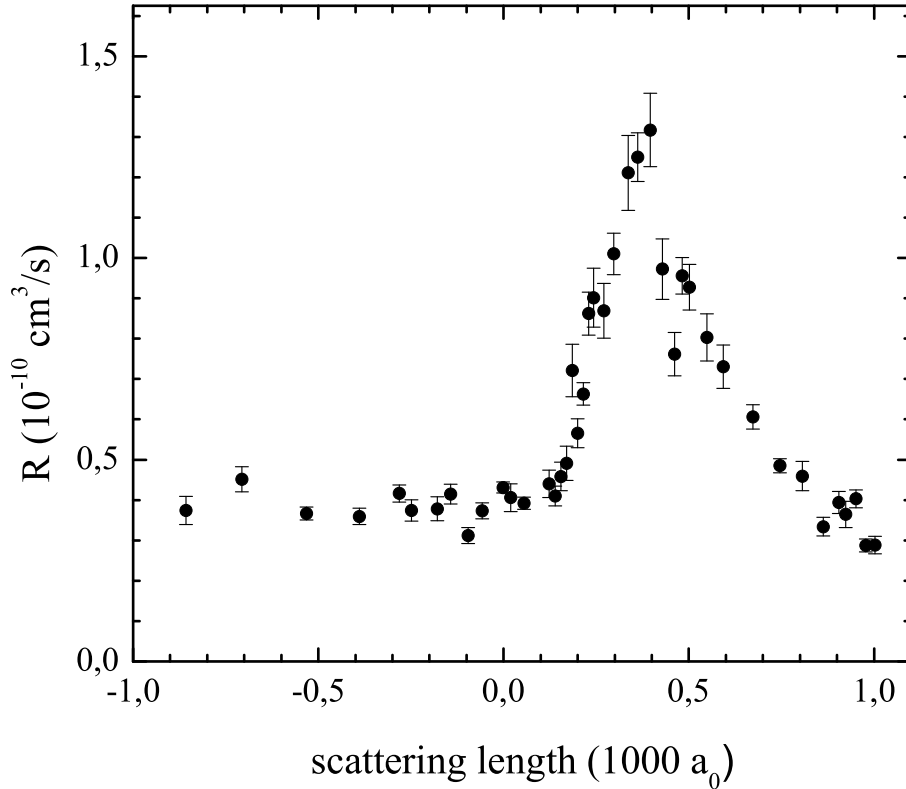


Figure 7.3: Measurement of the atom-dimer collision rate constant as a function of the magnetic field. The dimers are in the weakly bound $33(6, -1)$ -state. The ratio of atom number to dimer number is less than 10^{-2} . The dimer density is less than 10^{-9} cm^{-3} . This ensures that atom-dimer collisions dominate the decay of the dimers. The observed decay times are small compared to those due to background gas collisions and light induced losses [Mar07a]. Thus, significant dimer losses can be directly attributed to atom-dimer collisions.

diminishing Franck-Condon overlap of the universal and the deeply bound molecular wave-functions. Experiments investigating this possibility using the $33(6, -1)$ -state for magnetic fields up to 150 G are under way, and might even lead to the first attainment of stable Thomas-Fermi condensates of dimers made from bosonic atoms.

Cesium tunability

So far, our experiments on Efimov physics were carried out within the magnetic field region between zero and 150 G. The maximally attainable $|a|$ in that region does not allow for the observation of the predicted scaling of Efimov physics because only one Efimov state is supported. Although various other, rather narrow resonances can be found in that region, these are either deep in the closed-channel dominated regime or not sufficiently entrance-channel dominated to strictly fulfil $\eta \ll 1$, see Sec. 2.2 and

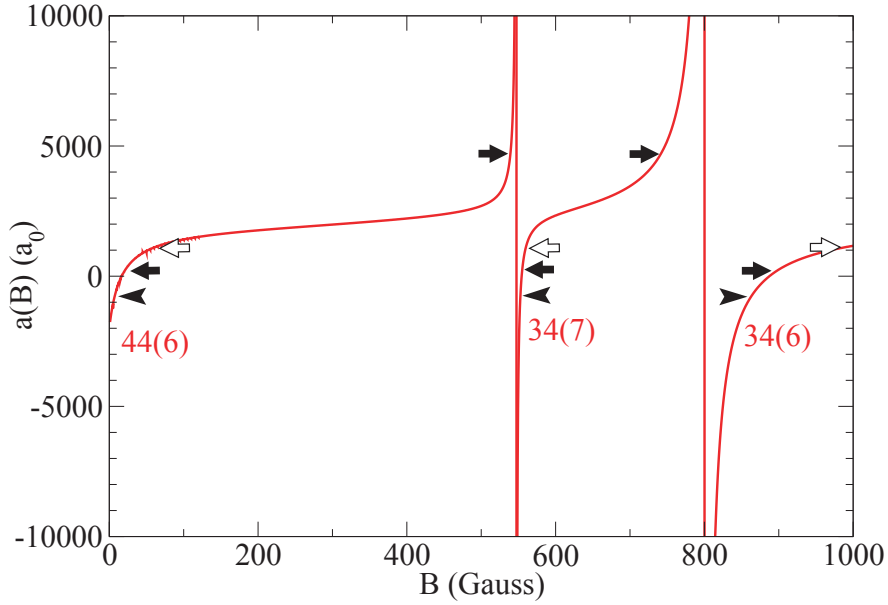


Figure 7.4: Scattering length of the $F = 3, m_F = 3$ state as a function of the magnetic field between zero and 1000 G. The Feshbach resonances result from avoided crossing involving the $33(6, -1)$ -state and are labelled according to the associated molecular channel quantum numbers $F_1 F_2(f)$. The resonances are entrance-channel dominated and are promising candidates for the search for Efimov-related effects. The molecular states causing the resonances have been described in detail in Sec. 3.3. The arrows mark the positions of triatomic Efimov resonances (arrow heads), three-body recombination minima (filled arrows) and atom-dimer scattering resonances (empty arrows). The positions are given by $a_+ = 1060 a_0$, $a_- = 850 a_0$ as determined from our measurements (see Sec. 5.4) and $a_{ad} = 1.1a_+$ (see Sec. 5.2.2 and Ref. [Bra06]) assuming an Efimov periodicity of 22.7. Figure courtesy by E. Tiesinga, NIST.

Eq. 2.6 for definitions.

There are, however, two more entrance-channel dominated Feshbach resonances located around 550 G and 800 G as outlined in Sec. 3.3. Fig. 7.4 shows the resulting scattering length. These resonances facilitate experimental access to large positive and negative scattering lengths. There are several closed-channel dominated resonances in the vicinity of the 500 G-resonance (not shown). Therefore the resonance centered at 800 G might be the more promising candidate for experimental access to the universal regime. The arrows in Fig. 7.4 indicate the values of a_+ and $22.7a_+$ (filled arrows) and a_- (arrow heads) as determined from our three-body recombination measurements. For the definitions of a_+ and a_- see Sec. 5.2.2. The expected positions of atom-dimer scattering resonances $a_{ad} = 1.1a_+ = 1.04a_-$ [Bra03, Bra06] are marked by the empty arrows. Taking full advantage of the tunability of Cs we might be able to detect two three-body scattering features from two adjacent Efimov states.

Perspectives for Efimov physics and cold atoms

Efimov trimers might be associated from atomic clouds by magnetic field modulation in the radio-frequency range. The rf-radiation directly couples three free atoms to an Efimov state similar to the association of dimers using magnetic-field modulation as demonstrated in Ref. [Tho05b]. Direct detection of Efimov states might be achieved by microwave spectroscopy. For Cs a possible microwave transition would couple the Efimov trimer to the $F = 4$ hyperfine manifold and lead to the production of free atoms from dissociation of Efimov trimers.

Association of Efimov trimers by magnetic field sweeps [Sto05] might be achieved using three free atoms in a tightly confining trap. An optical lattice environment might serve this purpose. The lattice might be prepared with exactly three atoms per lattice site. The physical concept underlying the adiabatic association of Efimov trimers in atom traps is analogous to the Feshbach association of dimers [Sto05]. The associated trimers might be stabilized by the suppression of tunneling among lattice sites which leads to suppression of de-exciting trimer-trimer collisions. In consequence long lifetimes of Efimov trimers might be achieved. A similar effect has been observed in the case of Feshbach-associated dimers in Ref. [Tha06].

An experimental confirmation of the Efimov effect would require the observation of the scaling factor $e^{-\pi/s_0}$ and the corresponding logarithmic periodicity. Thus at least three Efimov-related scattering effects have to be detected. To avoid unitary limitation in the observation of three such effects the requirements on atomic sample temperature are very severe. As an example the observation of the third triatomic Efimov resonance for three Cs atoms would require a sample temperature of 10^{-4} nK and access to scattering lengths on the order of $10^6 a_0$. The experimental requirements might be greatly relaxed by using atomic systems which feature a reduced scaling factor. A scaling factor significantly smaller than 22.7 is expected in the case of two heavy and one light particle [Bra06]. Therefore two-species mixtures of heavy and light atoms seem favorable. To ensure that three-body scattering processes involving two heavy and one light atom dominate over those involving two light and one heavy atom, the mixture should be made of heavy bosons and light fermions. Obviously both species should be susceptible to laser-cooling and the heavy-light and heavy-heavy two-body subsystems should both be resonantly interacting. With respect to minimizing the scaling factor a ^{133}Cs - ^6Li mixture seems optimal among the alkali metals featuring a scaling factor of ~ 5 [Bra06]. This factor would be even less for ^{174}Yb - ^6Li mixture.

APPENDIX A

Current control circuit

The circuitry used to stabilize the homogeneous bias field current resembles a PI-controller which actively stabilizes a voltage drop over a shunt resistor in the coil circuit to a given reference voltage. A circuit diagram is shown in Fig. A.1. The $1/e$ -response time to a step in the reference voltage is below $100 \mu\text{s}$. At the heart of the circuit lies a APT20M20JLL high-power MOSFET. The differential amplifiers are INA114, the op-amps OPA27. The shunt resistor is a Vishay foil resistor with an exceptionally low temperature rating of several 10^{-6} Ohms per degree Kelvin. Both the MOSFET and the shunt resistor are mounted on air-cooled heat sinks in order to ensure stable operating conditions. The operating voltages are $V_+ = 15 \text{ V}$ for driving the current, and $\pm V_{cc} = \pm 12 \text{ V}$ for the circuitry. $\pm V_{cc}$ are derived from voltage regulators. An adjustable constant offset voltage can be added to the reference voltage by a manual switch, or, alternatively, by a TTL-signal.

MOSFET Feedback Control

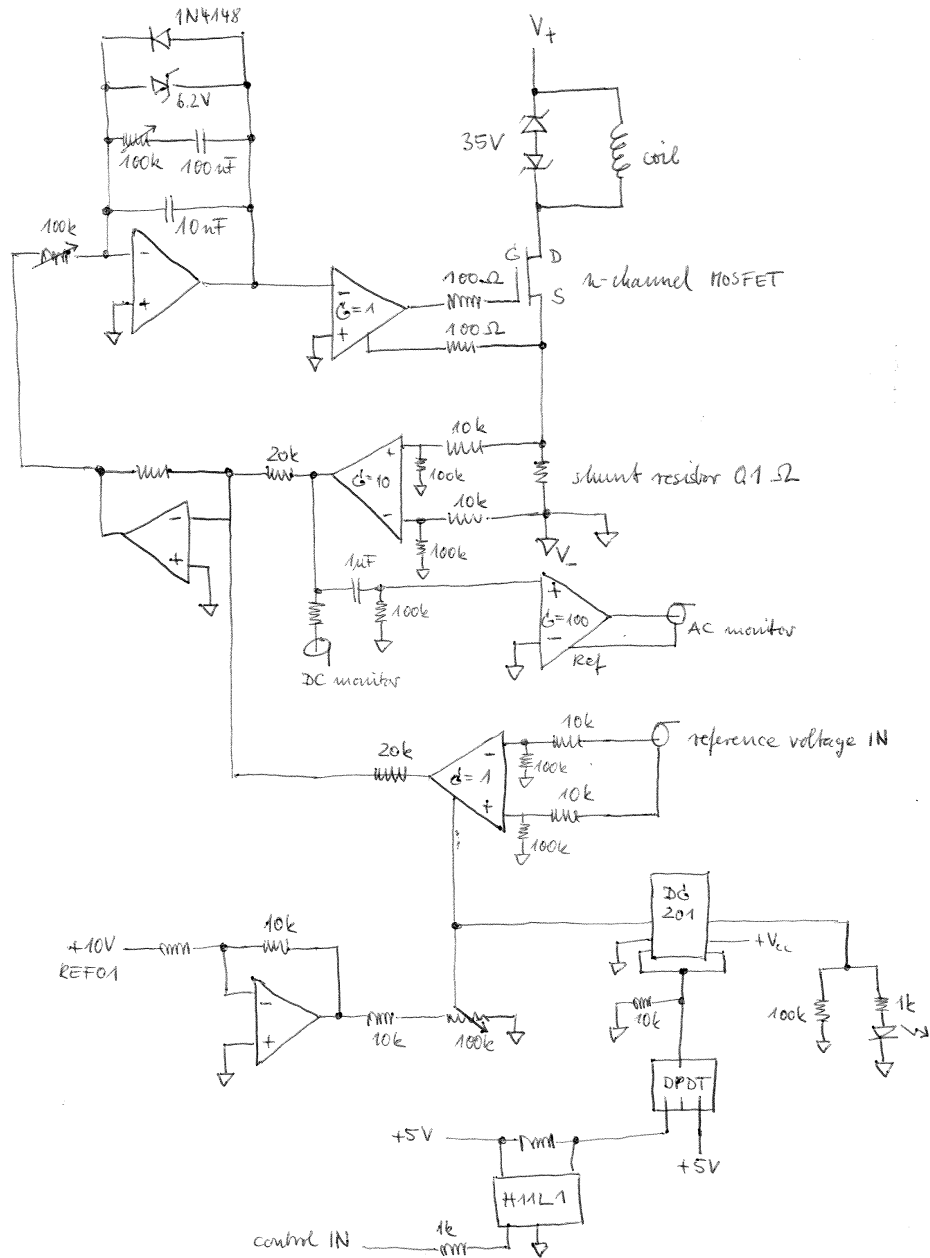


Figure A.1: Precise feedback control for stabilizing the current feeding the homogeneous bias field. For details, see text.

APPENDIX B

Publications

B.1 Preparation of a pure molecular quantum gas

J. Herbig, T. Kraemer, M. Mark, T. Weber, C. Chin, H.-C. Nägerl, and R. Grimm
Science **301**, 1510 (2003); published online 21 Aug 2003 (10.1126/science.1088876)

REPORTS

One additional correction that cannot be added as a σ in quadrature is the LMC rotation. Several young and intermediate-age kinematic tracers have been measured in the LMC, including HII regions, PN, CH stars, Miras, and carbon stars. In the inner regions of the LMC bar, these populations are rotating as a solid body, with 25 km/s per kpc. For a scale of 1 kpc = 1.2°, our fields should not show a rotation component larger than 10 km/s.

In addition, a correction for rotation may not be necessary for the RR Lyrae population, because there is no evidence that this old population follows the LMC rotation. On the basis of the Milky Way RR Lyrae, one might suspect that the LMC RR Lyrae do not rotate like the rest of the stars. However, a composite RR Lyrae population may be present. For example, earlier interpretation of the RR Lyrae number counts indicated an exponential disk distribution (31). Multiple components (halo plus thick disk) cannot be ruled out without rotation measurements. Our fields are not spread out enough to measure the rotation. In order to measure the systemic rotation of the RR Lyrae population, one would need to observe $N \cong 50$ stars per field in fields located $>3^\circ$ away on opposite sides of the bar. We estimate the correction in two ways: with the use of the velocities from HI maps (32) and with the use of the mean rotation fits of the disk (22, 24). This correction does not change at all the LMC RR Lyrae velocity dispersion.

The large RR Lyrae velocity dispersion $\sigma_{\text{true}} = 53$ km/s implies that metal-poor old stars are distributed in a halo population. The velocity dispersion for the old RR Lyrae stars is higher than that for the old LMC clusters, although there are too few old clusters to measure the kinematics in the LMC. The presence of a kinematically hot, old, and metal-poor halo in the LMC suggests that galaxies like the Milky Way and small galaxies like the LMC have similar early formation histories (33).

The stellar halo traced by the RR Lyrae amounts only to 2% of the mass of the LMC, which is akin to the Milky Way halo (1, 22). Consequently, its contribution to the microlensing optical depth should not be important (26, 34). The ongoing Supermacho experiment will discover an order of magnitude more microlensing events toward the LMC (35), allowing us to test this prediction.

References and Notes

1. T. D. Kinman *et al.*, *Publ. Astron. Soc. Pac.* **103**, 1279 (1991).
2. M. Feast, in *Variable Stars and Galaxies*, Brian Warner, Ed. [Astronomical Society of the Pacific (ASP) Conference Series 30, San Francisco, 1992], p. 143.
3. E. W. Olszewski, N. B. Suntzeff, M. Mateo, *Annual Rev. Astron. Astrophys.* **34**, 511 (1996).
4. D. Minniti, *Astrophys. J.* **459**, 175 (1996).
5. A. Layden, in *Galactic Halos*, D. Zaritsky, Ed. (ASP Conference Series 136, San Francisco, 1998), p. 14.
6. L. Searle, R. Zinn, *Astrophys. J.* **225**, 358 (1978).
7. O. Eggen, D. Lynden-Bell, A. Sandage, *Astrophys. J.* **136**, 748 (1962).
8. D. Minniti, A. A. Zijlstra, *Astrophys. J.* **467**, L13 (1996).
9. D. R. Alves, M. Rejkuba, D. Minniti, K. H. Cook, *Astrophys. J.* **573**, L51 (2002).
10. K. C. Freeman, G. Illingworth, A. Oemler, *Astrophys. J.* **272**, 488 (1983).
11. R. A. Schommer, E. W. Olszewski, N. B. Suntzeff, H. C. Harris, *Astron. J.* **103**, 447 (1992).
12. C. Alcock *et al.*, *Astrophys. J.* **490**, L59 (1997).
13. C. Alcock *et al.*, *Astrophys. J.* **482**, 89 (1997).
14. C. Alcock *et al.*, *Astrophys. J.* **542**, 257 (2000).
15. The MACHO RR Lyrae data are available online at the MACHO Project home page (www.macho.mcmaster.ca/). These RR Lyrae are classified on the basis of the MACHO light curves, with RRab being fundamental pulsators; RRc, first overtones; and RRe, double mode pulsators.
16. H. A. Smith, *The RR Lyrae Stars* (Cambridge Univ. Press, Cambridge, 1995).
17. C. M. Clement *et al.*, *Astron. J.* **122**, 2587 (2001).
18. M. Mayor *et al.*, *Astron. Astrophys.* **114**, 1087 (1997).
19. J. Kaluzny *et al.*, *Astron. Astrophys. Suppl. Ser.* **122**, 471 (1997).
20. J. E. Norris, K. C. Freeman, M. Mayor, P. Seitzer, *Astrophys. J.* **487**, 187 (1997).
21. D. S. Graff, A. Gould, N. B. Suntzeff, R. Schommer, E. Hardy, *Astrophys. J.* **540**, 211 (2000).
22. D. R. Alves, C. A. Nelson, *Astrophys. J.* **542**, 789 (2001).
23. E. Hardy, D. R. Alves, D. S. Graff, N. B. Suntzeff, R. A. Schommer, *Astrophys. J. Suppl. Ser.* **277**, 471 (2001).
24. R. P. van der Marel, D. R. Alves, E. Hardy, N. B. Suntzeff, *Astron. J.* **124**, 2639 (2002).
25. S. M. G. Hughes, P. R. Wood, I. N. Reid, *Astron. J.* **101**, 1304 (1991).
26. G. Gyuk, N. Dalal, K. Griest, *Astrophys. J.* **535**, 90 (2000).
27. We eliminated a low-velocity star, discrepant by more than 4σ from the mean, which could be a misidentified foreground star.
28. G. Clementini, R. Megghi, C. Cacciari, C. Gouiffes, *Mon. Not. R. Astron. Soc.* **267**, 83 (1994).
29. I. Skillen, J. A. Fernley, R. S. Stobie, R. F. Jameson, *Mon. Not. R. Astron. Soc.* **265**, 301 (1993).
30. We adopt a conservative error of 10 km/s for this quantity on the basis of uncertainties in the control samples.
31. C. Alcock *et al.*, *Astron. J.* **119**, 2194 (2000).
32. K. Rohlf, J. Kreitschmann, B. C. Siegelman, J. V. Feitzinger, *Astron. Astrophys.* **137**, 343 (1984).
33. The sample is not large enough and the velocities are not accurate enough to (i) detect tidal streams in front or behind the LMC and (ii) measure the systemic rotation of the halo RR Lyrae population. However, from a sample of this size, and with velocities measured to this accuracy, there is no difficulty in measuring the velocity dispersion and thus distinguishing a disk population from a halo population in the LMC.
34. C. Alcock *et al.*, *Astrophys. J.* **542**, 281 (2000).
35. C. Stubbs, in *The Galactic Halo*, B. K. Gibson, T. S. Axelrod, M. E. Putman, Eds. (ASP Conference Series 165, San Francisco, 2000), p. 503.
36. We gratefully acknowledge suggestions from E. Olszewski, A. Drake, M. Catelan, and C. Alcock and support by the Fondap Center for Astrophysics 15010003; by the U.S. Department of Energy National Nuclear Security Administration to University of California's Lawrence Livermore National Laboratory under contract W-7405-Eng-48; and by the Bilateral Science and Technology Program of the Australian Department of Industry, Technology, and Regional Development; and by ESO Program 70.B-0547.

27 June 2003; accepted 11 August 2003

Preparation of a Pure Molecular Quantum Gas

Jens Herbig, Tobias Kraemer, Michael Mark, Tino Weber, Cheng Chin, Hanns-Christoph Nägerl, Rudolf Grimm*

An ultracold molecular quantum gas is created by application of a magnetic field sweep across a Feshbach resonance to a Bose-Einstein condensate of cesium atoms. The ability to separate the molecules from the atoms permits direct imaging of the pure molecular sample. Magnetic levitation enables study of the dynamics of the ensemble on extended time scales. We measured ultralow expansion energies in the range of a few nanokelvin for a sample of 3000 molecules. Our observations are consistent with the presence of a macroscopic molecular matter wave.

Rapid progress in controlling ultracold atomic gases, culminating in the creation of atomic Bose-Einstein condensates (BECs) and opening the door to the realm of coherent matter-wave physics (1–3), has raised the question of whether a similar level of control is possible with molecular samples. Molecules, in contrast to atoms, have a much richer internal structure and can possess permanent vector or tensor properties, such as electric dipole moments, rotational angular momentum, and

even chirality. Molecule-atom and molecule-molecule interactions are at least three- and four-body processes in nature, posing new challenges to our theoretical understanding. Exquisite control over the internal and external degrees of freedom of molecules could allow the experimental study of a new coherent chemistry (4), where matter-wave interference, quantum tunneling, and bosonic stimulation dominate the dynamics and where the interaction properties can be externally controlled and engineered with electromagnetic fields. Quantum degenerate molecular gases with permanent dipole moments are also prime candidates for the precise investigation of strongly correlated quantum

Institut für Experimentalphysik, Universität Innsbruck, Technikerstraße 25, 6020 Innsbruck, Austria.

*To whom correspondence should be addressed. E-mail: rudolf.grimm@uibk.ac.at

systems and for the study of novel quantum phase transitions (5).

Several avenues have been investigated to cool and trap molecules. Slowing of a supersonic jet of polar molecules in time-varying electric fields (6) and buffer gas loading and trapping (7) in either electrostatic or magnetic traps both permit large molecular populations with temperatures in the mK range. Alternatively, creation of molecules by photoassociation of precooled atoms has led to molecular samples with temperatures in the μK range (8). For all these techniques, however, the resulting molecular phase-space density is still many orders of magnitude away from quantum degeneracy.

Starting with a sample of ultracold atoms, controlled production of molecules can be realized by the coherent coupling of an atom pair state to a molecular state. For example, a two-photon Raman transition has successfully been applied to produce molecules within an atomic BEC (9). Similarly, the coherent nature of atomic scattering can be exploited on a Feshbach resonance to transfer colliding atoms into molecules, which has been predicted to convert an atomic BEC into a molecular BEC (10–12). A Feshbach resonance occurs when the energy of the atomic scattering state is tuned into degeneracy with that of a bound molecular state (13). Experimentally, Feshbach resonances can be induced by an external magnetic field when both states feature different Zeeman shifts. Consequently, the atom-molecule coupling can be resonantly enhanced at a particular magnetic field value, and a sweep of the field near or across the resonance can convert the atoms into molecules in a single molecular quantum state. Existence of molecules created through atomic Feshbach resonances has been reported previously in a BEC of ^{85}Rb atoms (14), in thermal samples of ^{133}Cs (15), and in degenerate Fermi gases of ^{40}K (16) and ^6Li (17). These studies demonstrate the quantum coherence of the Feshbach coupling (14) and the ability to detect molecules within the atomic sample by means of laser-induced (15) or radiofrequency-induced (16) dissociation. However, the resulting molecular samples could not be spatially distinguished from the atoms, nor could the molecular clouds be directly imaged and analyzed. Here, we report the observation of pure molecular quantum matter, achieved by applying a Feshbach sweep to an atomic Cs BEC (18) with immediate spatial Stern-Gerlach separation of the two species. By monitoring the evolution of the coupled-out molecular cloud, we measure ultralow kinetic expansion energies that are consistent with the presence of a coherent molecular matter wave.

The starting point of our experiment was a pure BEC of up to 6×10^4 Cs atoms in an optical trap (19) with a radial Thomas-Fermi

radius of $8.6 \mu\text{m}$ and an axial Thomas-Fermi radius of $26.5 \mu\text{m}$. The atoms were in the hyperfine ground state with total angular momentum $F = 3$ and magnetic quantum number $m_F = 3$. As the optical trap was by far too weak to support the atoms against gravity during the evaporative cooling process, a magnetic field gradient of 30.9 G/cm was applied to levitate the atoms (20). This levitation is very sensitive to the magnetic moment of the trapped particles, and a small change of 1% in either the gradient or in the magnetic moment of the trapped particles is sufficient to render the trap unstable. The state $F = 3$, $m_F = 3$ features a narrow Feshbach resonance near 20 G (21) with an estimated resonance width of 5 mG (22). According to an analysis of the Cs scattering properties (23, 24), the corresponding molecular state (25) has a predicted magnetic moment of $\mu = 0.93 \mu_B$, where μ_B is Bohr's magneton, with a small magnetic field dependence (22). We produced molecules from the atomic BEC by sweeping the magnetic field across the resonance from a higher field value with a constant rate of typically 50 G/s (Fig. 1). The duration of the sweep was 3 ms . To turn off the Feshbach coupling, the field was then quickly lowered to a hold field at 17 G for a variable hold time while the optical trap was shut off (20). Because of the large magnetic field gradient along the vertical direction and the narrow resonance width of 5 mG , the Feshbach resonance occurred only within a $2\text{-}\mu\text{m}$ -thin horizontal layer. The conversion

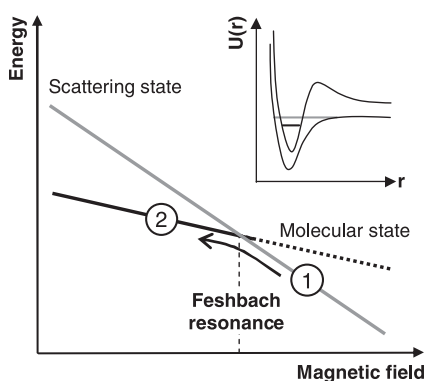


Fig. 1. Energy diagram for the atomic scattering state and the molecular bound state. The Feshbach resonance condition occurs near 20 G , where the Zeeman energy of the atomic scattering state becomes equal to that of a molecular bound state because of the difference in magnetic moments. Molecules at (2) are created from the BEC at (1) by a downward sweep of the magnetic field across the resonance. For detection, a reversed sweep brings the molecules above the dissociation limit. The inset schematically shows the molecular potential that corresponds to the open channel (lower curve) and the molecular potential that supports the bound state (upper curve). U , potential energy; r , interatomic distance.

zone swept through the condensate from below at a speed of $15 \mu\text{m/ms}$, or equivalently, in 1.3 ms . The newly created molecules immediately started falling with an acceleration of $0.38g$ due to their reduced magnetic moment. The molecular cloud was then completely separated from the atoms within 3 ms . By raising the magnetic field gradient quickly at the end of the sweep to about 50 G/cm , we levitated the molecules. In this case, the atoms accelerated upward at $0.61g$. Rapid molecule-atom separation and subsequent levitation permit long observation times for studying the dynamics of the molecular sample.

To image the molecular cloud, we applied a reversed field sweep across the Feshbach resonance. The reversed sweep brought the molecules above the scattering continuum, and they quickly dissociated into free atoms. An immediate absorption image of the reconverted atoms thus reveals the spatial distribution of the molecules. A resolution limit of about $10 \mu\text{m}$ was caused by an energy on the order of $k_B \times 1 \mu\text{K}$ released in the dissociation process (20), where k_B is the Boltzmann constant. We applied a fit to the image to determine the center position, the size of the spatial distribution, and the number of molecules. The evolution of the molecular cloud was recorded by variation of the hold time.

The complete atom-molecule separation is clearly visible in absorption images (Fig. 2). For reference, the image of a levitated BEC after 12 ms of expansion time is given in Fig. 2A. In Fig. 2, B and C, a Feshbach sweep has been applied to the BEC. In Fig. 2B, a coupled-out molecular cloud with ~ 3000 molecules can be seen below the atomic BEC. The number of atoms in the remaining BEC is reduced by 50% from those shown in Fig. 2A, to $\sim 25,000$. The molecular cloud is falling, because the magnetic field gradient needed to levitate the atoms was maintained. For Fig. 2C, the magnetic field gradient was

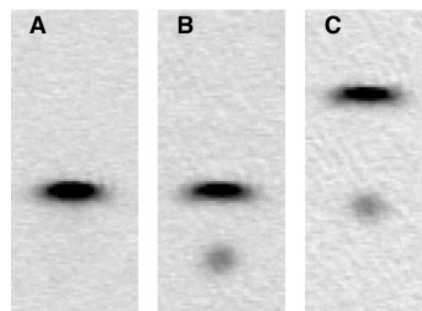


Fig. 2. Absorption images of (A) the levitated BEC without the Feshbach sweep, (B) the levitated BEC after the Feshbach sweep with a falling molecular cloud below, and (C) the levitated molecular cloud with an upward-rising BEC above. In (B) and (C), 3000 molecules are produced at a sweep rate of 50 G/s . The separation between the atoms and the molecules is $150 \mu\text{m}$ in (B) and $240 \mu\text{m}$ in (C).

REPORTS

raised after the Feshbach sweep in order to levitate the molecules. Hence, the atomic BEC accelerates upward and can be seen at the top of the image above the molecules. Careful adjustment of the magnetic field gradient to null the molecular acceleration allowed a precise determination of the molecular magnetic moment. We find that $\mu = 0.930(5) \mu_B$ (20), which is in good agreement with the theoretical calculation (22).

We investigated the atom-molecule conversion as a function of the end value B_f of the creation ramp. The ramp speed was kept constant at 50 G/s by variation of B_f together with the duration of the ramp. We have checked that for final values of B_f well above the resonance, the rapid jump over the resonance to the hold field after the end of the creation ramp did not produce any molecules. As Fig. 3 shows, molecules were created in a steplike manner. Simultaneously, the atomic population in the BEC is reduced. The transition value agrees well with the resonance position of 19.83(2) G as determined from three-body recombination loss measurements (26). From the plot of the atom number, it can be seen that up to 50% of the atoms were lost from the condensate, corresponding to $\sim 25,000$ atoms for this experiment. Hence, for a detected number of 3000 molecules, only about 24% of the lost atoms reappeared as partners in molecule formation. Also, we varied the speed of the downward magnetic field ramp across the Feshbach resonance and found that for decreasing ramp speed, the number of detected molecules saturated at a value of ~ 3000 molecules for speeds less than 50 G/s. The missing atoms and the saturation suggest that collisional relaxation into other molecular states occurs during the creation phase (27). After separation from the atoms, however, we did not detect any substantial loss.

We observed ultralow expansion energies for the molecular cloud in both the vertical and the horizontal directions. This was done in time-of-flight expansion measurements by variation of the hold time and hence the total ex-

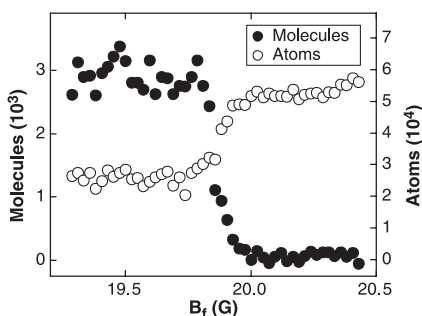


Fig. 3. Creation of molecules (solid circles) and simultaneous loss of atoms (open circles) as a function of the final value of the magnetic field ramp B_f for a fixed ramp speed of 50 G/s.

pansion time. We plotted the vertical and horizontal root-mean-square (rms) widths of the reconverted atomic cloud as a function of total expansion time (Fig. 4, A and B). An apparent anisotropy of the expansion can be seen. The faster vertical expansion corresponds to a mean kinetic energy of $E_z = \frac{1}{2} k_B \times (40 \pm 3 \pm 2)$ nK (20), where the first one-standard-deviation error is statistical and the second one is systematic. The origin of this vertical energy was identified as the velocity dispersion of the molecules during the creation phase. The dispersion was caused by the fact that the conversion zone passes through the condensate at a finite speed from below. Hence, molecules created earlier acquire a larger velocity, and those created later acquire a smaller velocity, as a result of the gravity pulling. When the size of the BEC was taken into account, the vertical expansion energy as a result of the velocity dispersion was calculated to be about $\frac{1}{2} k_B \times 30$ nK for the molecular cloud, largely explaining the observed energy. In fact, vertical compression of the BEC did lead to a smaller vertical energy spread. By increasing the dipole trap depth to decrease the vertical extent of the BEC by a factor of 1.3, we found that the measured molecular kinetic energy was reduced in the expected way to a value of $E_z = \frac{1}{2} k_B \times (19 \pm 2 \pm 1)$ nK.

The horizontal expansion shown in Fig. 4B was unaffected by the velocity dispersion effect. However, a repulsive force due to the curvature of the levitation field acted on the molecules. This force resulted in an expansion of the cloud that follows a cosine hyperbolic function and has been characterized previously (18). When the resolution limit due to the dissociation and the cosine hyperbolic expansion dynamics (20) is incorporated, the fit in Fig. 4B yields an extremely

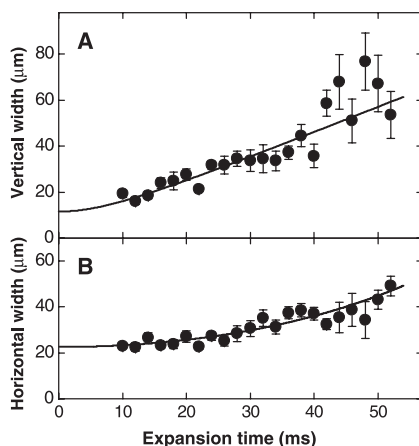


Fig. 4. (A) Vertical rms width and (B) horizontal rms width of the molecular cloud as a function of expansion time. From (A), a vertical expansion energy of $E_z = \frac{1}{2} k_B \times (40 \pm 3 \pm 2)$ nK and an imaging resolution of 11(3) μm is obtained. The fit in (B) then yields an initial horizontal expansion energy of $E_x = \frac{1}{2} k_B \times (2 \pm 2 \pm 3)$ nK.

low kinetic energy of $E_x = \frac{1}{2} k_B \times (2 \pm 2 \pm 3)$ nK in the horizontal direction.

The slow expansion of the molecules is consistent with the behavior of a macroscopic matter wave, as the horizontal expansion showed vanishing release energy and the vertical expansion was dominated by the dispersive gravity pulling effect, which is coherent in its nature. In view of a possible quantum degeneracy of the molecular ensemble, we first estimated the peak molecular density right after creation to $1 \times 10^{12} \text{ cm}^{-3}$, assuming 3000 molecules with a spatial density profile that reflects that of the atomic BEC (28). Given the free-space degeneracy condition, the critical temperature is 6 nK. Comparing this value to the observed horizontal energy spread that corresponds to $(2 \pm 2 \pm 3)$ nK, we raise the question whether a molecular cloud with macroscopic coherence has been created. Our capability to monitor the spatial distribution of the molecules should allow us to detect interference patterns (29) and thus to investigate the macroscopic coherence of the molecular matter wave.

To create molecules coherently with high efficiency, it will be advantageous to load the atomic BEC into an optical lattice (30), which allows the preparation of a Mott insulator phase (31) with exactly two atoms per lattice site. Molecules created by a subsequent Feshbach sweep will therefore be individually isolated and immune to collisional losses. After the creation of a pure molecular matter wave, one might be able to coherently transfer the molecules to low-lying molecular states by two-photon Raman transitions. Hence, a complete and coherent control over the dynamics of molecular quantum matter can be envisaged.

References and Notes

1. E. A. Cornell, C. E. Wieman, *Rev. Mod. Phys.* **74**, 875 (2002).
2. W. Ketterle, *Rev. Mod. Phys.* **74**, 1131 (2002).
3. Nature Insight on Ultracold Matter, *Nature* **416**, 205 (2002).
4. D. J. Heinzen, R. Wynar, P. D. Drummond, K. V. Kheruntsyan, *Phys. Rev. Lett.* **84**, 5029 (2000).
5. K. Góral, L. Santos, M. Lewenstein, *Phys. Rev. Lett.* **88**, 170406 (2002).
6. H. L. Bethlem *et al.*, *Nature* **406**, 491 (2000).
7. J. D. Weinstein, R. deCarvalho, T. Guillet, B. Friedrich, J. M. Doyle, *Nature* **395**, 148 (1998).
8. N. Vanhaecke, W. de Souza Melo, B. L. Tolra, D. Comparat, P. Pillet, *Phys. Rev. Lett.* **89**, 063201 (2002).
9. R. Wynar, R. S. Freeland, D. J. Han, C. Ryu, D. J. Heinzen, *Science* **287**, 1016 (2000).
10. F. A. van Abeelen, B. J. Verhaar, *Phys. Rev. Lett.* **83**, 1550 (1999).
11. E. Timmermans, P. Tommasini, M. Hussein, A. Kerman, *Phys. Rep.* **315**, 199 (1999).
12. F. H. Mies, E. Tiesinga, P. S. Julienne, *Phys. Rev. A* **61**, 022721 (2000).
13. S. Inouye *et al.*, *Nature* **392**, 151 (1998).
14. E. A. Donley, N. R. Claussen, S. T. Thompson, C. E. Wieman, *Nature* **417**, 529 (2002).
15. C. Chin, A. J. Kerman, V. Vuletić, S. Chu, *Phys. Rev. Lett.* **90**, 033201 (2003).
16. C. A. Regal, C. Ticknor, J. L. Bohn, D. S. Jin, *Nature* **424**, 47 (2003).

17. C. Salomon, talk presented at the Quantum Electronics and Laser Science Conference, Baltimore, MD, 5 June 2003.
18. T. Weber, J. Herbig, M. Mark, H.-C. Nägerl, R. Grimm, *Science* **299**, 232 (2003); published online 5 Dec 2002 (10.1126/science.1079699).
19. The optical trap has a depth of $k_B \times 45$ nK with a radial trap frequency of 18 Hz and an axial trap frequency of 6 Hz. The axial direction of the BEC is oriented in the horizontal plane. At 20 G, the Cs scattering length is $a = 163 a_0$, with a_0 denoting Bohr's radius. The resulting chemical potential for the BEC is $k_B \times 7$ nK.
20. Materials and methods are available as supporting material on *Science* Online.
21. V. Vuletić, C. Chin, A. J. Kerman, S. Chu, *Phys. Rev. Lett.* **83**, 943 (1999).
22. P. S. Julienne, E. Tiesinga, private communication (2003).
23. C. Chin, V. Vuletić, A. J. Kerman, S. Chu, *Phys. Rev. Lett.* **85**, 2717 (2000).
24. P. J. Leo, C. J. Williams, P. S. Julienne, *Phys. Rev. Lett.* **85**, 2721 (2000).
25. The molecular state was identified as a high-lying rovibrational state with internal angular momentum $f = 4$, magnetic quantum number $m_f = 4$, molecular orbital angular momentum $L = 4$, and angular momentum projection $m_L = 2$.
26. T. Weber, J. Herbig, M. Mark, H.-C. Nägerl, R. Grimm, *Phys. Rev. Lett.*, in press (available at <http://arXiv.org/abs/physics/0304052>).
27. V. A. Yurovsky, A. Ben-Reuven, P. S. Julienne, C. J. Williams, *Phys. Rev. A* **62**, 043605 (2000).
28. This is a reasonable assumption, because no molecules can be created in the absence of atoms.
29. M. R. Andrews *et al.*, *Science* **275**, 637 (1997).
30. D. Jaksch, V. Venturi, J. I. Cirac, C. J. Williams, P. Zoller, *Phys. Rev. Lett.* **89**, 040402 (2002).

31. M. Greiner, O. Mandel, T. Esslinger, T. W. Hänsch, I. Bloch, *Nature* **415**, 39 (2002).
32. We thank P. S. Julienne for very helpful discussions. Supported by the Austrian Science Fund (FWF) within Spezialforschungsbereich 15 (project part 16) and by the European Union through the Cold Molecules Training and Mobility of Researchers Network under contract no. HPRN-CT-2002-00290.

Supporting Online Material

www.sciencemag.org/cgi/content/full/1088876/DC1
Materials and Methods
Figs. S1 to S3

7 July 2003; accepted 11 August 2003

Published online 21 August 2003;

10.1126/science.1088876

Include this information when citing this paper.

Cooling Bose-Einstein Condensates Below 500 Picokelvin

A. E. Leanhardt,* T. A. Pasquini, M. Saba, A. Schirotzek, Y. Shin, D. Kielpinski, D. E. Pritchard, W. Ketterle

Spin-polarized gaseous Bose-Einstein condensates were confined by a combination of gravitational and magnetic forces. The partially condensed atomic vapors were adiabatically decompressed by weakening the gravito-magnetic trap to a mean frequency of 1 hertz, then evaporatively reduced in size to 2500 atoms. This lowered the peak condensate density to 5×10^{10} atoms per cubic centimeter and cooled the entire cloud in all three dimensions to a kinetic temperature of 450 ± 80 picokelvin. Such spin-polarized, dilute, and ultracold gases are important for spectroscopy, metrology, and atom optics.

The pursuit of lower temperatures is motivated by the quest to observe phenomena that occur on very low energy scales, in particular, phase transitions to new forms of matter. The achievement of temperatures near 1 K in solids and in liquids led to the discoveries of superconductivity (1) and superfluidity (2), respectively. The advent of laser cooling resulted in microkelvin temperature atomic vapors (3–5), subsequently cooled to nanokelvin temperatures by evaporative cooling to form dilute Bose-Einstein condensates (6, 7) and quantum degenerate Fermi gases (8). Collectively, these low-temperature systems have a host of applications, including superconducting quantum interference devices (SQUIDs) (9), superfluid gyroscopes (10, 11), and atomic clocks (12).

Temperature is a quantity that parameterizes how energy is distributed across the available states of a system, and effective temperatures can be defined for decoupled degrees of freedom or subsets of particles. For example, nuclear spins isolated from the

kinetic motion of their respective atoms have been cooled by adiabatic demagnetization to an effective temperature of 280 pK (13). Spin ensembles have a finite number of available states, such that a spin-polarized sample, as in our work, would be characterized by zero effective temperature. In contrast, the motion of free particles is subject to a continuum of states, and the kinetic temperature of an ensemble can only asymptotically approach absolute zero.

Effective temperatures in atomic vapors are defined by the widths of velocity distributions, which can be much smaller than the mean velocity of the sample. Raman cooling (14, 15) and velocity-selective coherent population trapping (VSCPT) (16) have generated velocity distributions with very narrow peaks, corresponding to nanokelvin and picokelvin effective temperatures. However, these temperatures were associated with the motion of only a subset of the atoms in the cloud and/or with atomic motion in only one dimension.

For trapped, partially condensed atomic vapors, the condensate fraction has zero entropy and the kinetic temperature of the sample is determined by the velocity distribution of the thermal (noncondensed) component. When released, the condensate fraction expands more slowly than the thermal compo-

nent and has been characterized by picokelvin effective temperatures for anisotropic (17) and noninteracting (18) gases.

Cooling the atomic motion of entire ensembles in all three dimensions has proven difficult. To date, kinetic temperatures of a few hundred nanokelvin have been achieved with adiabatic and optical cooling (19, 20), and evaporative cooling techniques have produced condensates with temperatures of 3 nK (21). By adiabatic expansion and subsequent evaporation, we have cooled partially condensed atomic vapors to picokelvin kinetic temperatures.

Our thermometry is calibrated by the Bose-Einstein condensation (BEC) phase transition temperature, T_c , which in the thermodynamic limit for a harmonically trapped ideal Bose gas is (22)

$$k_B T_c = \hbar \bar{\omega} \left(\frac{N}{\zeta(3)} \right)^{1/3} \approx 0.94 \hbar \bar{\omega} N^{1/3} \quad (1)$$

where k_B is Boltzmann's constant, \hbar is Planck's constant h divided by 2π , $\zeta(n)$ is the Riemann Zeta function, $\bar{\omega} = (\omega_x \omega_y \omega_z)^{1/3}$ is the geometric mean of the harmonic trap frequencies, and N is the total number of atoms, both condensed and noncondensed. Thus, the atom number and the trap frequencies set an upper limit for the temperature of a confined Bose-Einstein condensate. In our work, adiabatically weakening the trapping potential to a mean frequency of $\bar{\omega} = 2\pi \times (1.12 \pm 0.08)$ Hz guaranteed that partially condensed atomic vapors with $N \leq 8000$ atoms had picokelvin temperatures ($T_c \leq 1$ nK).

Bose-Einstein condensates containing more than 10^7 ^{23}Na atoms were created in the weak field seeking $|F = 1, m_F = -1\rangle$ state in a magnetic trap, captured in the focus of an optical tweezers laser beam, and transferred into an auxiliary "science" chamber as described in (23). In the science chamber, condensates containing 2×10^6 to 3×10^6 atoms were transferred from the optical tweezers into a gravito-magnetic trap (Fig. 1A). A small coil carrying current I_S generated a vertical bias field B_z and supported the condensates against gravity with a vertical magnetic field gradient, $B'_z = 2$ mg/

Department of Physics, MIT-Harvard Center for Ultracold Atoms, and Research Laboratory of Electronics, Massachusetts Institute of Technology, Cambridge, MA 02139, USA.

*To whom correspondence should be addressed. E-mail: ael@mit.edu

B.2 Optimized production of a cesium Bose-Einstein condensate

T. Kraemer, J. Herbig, M. Mark, T. Weber, C. Chin, H.-C. Nägerl, and R. Grimm
Appl. Phys. B **79**, 1013 (2004). cond-mat/0408268

T. KRAEMER¹
J. HERBIG¹
M. MARK¹
T. WEBER¹
C. CHIN¹
H.-C. NÄGERL^{1,✉}
R. GRIMM^{1,2}

Optimized production of a cesium Bose–Einstein condensate

¹ Institut für Experimentalphysik, Universität Innsbruck, Technikerstraße 25, 6020 Innsbruck, Austria
² Institut für Quantenoptik und Quanteninformation, Österreichische Akademie der Wissenschaften, 6020 Innsbruck, Austria

Received: 11 August 2004

Published online: 6 October 2004 • © Springer-Verlag 2004

ABSTRACT We report on the optimized production of a Bose–Einstein condensate of cesium atoms using an optical trapping approach. Based on an improved trap loading and evaporation scheme we obtain more than 10^5 atoms in the condensed phase. To test the tunability of the interaction in the condensate we study the expansion of the condensate as a function of scattering length. We further excite strong oscillations of the trapped condensate by rapidly varying the interaction strength.

PACS 03.75.Kk; 32.80.Pj

1 Introduction

Much of the present work in the field of quantum gases relies on optical trapping techniques and on the ability to tune atomic interactions. Optical approaches have been recently employed in several atomic Bose–Einstein condensation experiments [1–5] and in experiments on the production of ultracold molecular samples [6–10] and on molecular Bose–Einstein condensates [11, 12]. The major advantages in optical traps are the possibility to trap atoms in any sub-level of the electronic ground state and the ease to adjust the interaction strength using magnetically induced Feshbach resonances.

The cesium atom is very attractive for experiments with tunable atomic interactions. The lowest internal quantum state of Cs features a unique combination of wide and narrow Feshbach resonances which are easily accessible at low magnetic fields [13]. This results in a great flexibility for tuning the atomic scattering properties. In particular, magnetic tuning of the interaction strength has recently allowed the first realization of a Bose–Einstein condensate (BEC) with Cs atoms [4] and the realization of a two-dimensional condensate very close to a dielectric surface [5]. The tunability of the atomic interaction can be exploited in experiments where one might wish to adjust or to dynamically change the mean-field interaction of the condensate. Also, the Feshbach resonances can be used to produce molecules from an atomic BEC [8–10, 14]

and to study the transition from an atomic BEC to a molecular BEC. In this context, a quantum phase transition with an essentially topological character has been predicted [15, 16]. For such and many other intriguing experiments it is desirable to have a large BEC of Cs atoms as a starting point.

In this paper we report on the optimized production of an essentially pure Cs BEC in the lowest internal quantum state with more than 10^5 atoms. Since this state cannot be trapped by purely magnetic means, the path to condensation relies on a sequence of optical traps. We discuss the loading and transfer from one trap to the next and give a detailed description of the evaporation path and of the resulting condensate. As a demonstration for tunability, we measure the expansion energy as a function of scattering length in time-of-flight experiments. In particular, we show the ultra-slow expansion of the condensate after release from the trap for nearly vanishing scattering length. The release energy corresponds to ~ 50 pK. Finally, we present first results when the scattering length is suddenly stepped and the condensate then starts to oscillate freely in the trap.

2 Cesium scattering properties and Feshbach resonances

Early experiments [17, 18] towards condensation of cesium focused on samples in magnetic traps polarized either in the upper hyperfine ground state $F = 4$, magnetic sub-level $m_F = 4$, or in the lower hyperfine state $F = 3$, $m_F = -3$. Here, F denotes the total angular momentum and m_F the magnetic quantum number. The spin relaxation rates were measured to be several orders of magnitude higher than expected [19–21]. It was later understood that this is caused by the dipolar relaxation process induced by the second-order spin–orbit interaction [22]. The maximum phase-space density in a small sample of Cs atoms was a factor of about four away from condensation [23].

The problem of the strong inelastic two-body losses can be overcome by using the lowest internal state of cesium, $F = 3$, $m_F = 3$ [24–27]. In this state, all inelastic two-body processes are endothermic and are thus fully suppressed at sufficiently low temperature. This state requires optical trapping since it cannot be captured in a magnetic trap. Optically trapped atoms can only be efficiently evaporated by lowering the total potential depth. This process weakens the confine-

✉ Fax: +43-512-507-2921, E-mail: christoph.naegerl@uibk.ac.at

ment of the trapped sample and thus makes it difficult to achieve sufficiently high elastic collision rates for effective evaporation. Hence, adjustability of the collisional properties is very helpful for a fast evaporation strategy.

The success in condensing Cs [4] largely relies on the fact that the s -wave scattering length for the $F = 3, m_F = 3$ state can be tuned to moderate and positive values by the application of relatively low dc magnetic fields [13]. As Fig. 1 shows, an external magnetic field allows for precise tuning of the atomic scattering length a from negative to positive values. Positive scattering lengths in the range between zero and one thousand a_0 are attained for magnetic fields of a few ten Gauss; a_0 denotes Bohr's radius. In particular, there is a gentle zero-crossing of the scattering length near 17 G [25]. Here, the interaction of atoms in a BEC is effectively switched off. Several narrow higher-order Feshbach resonances [13], caused by coupling to d - and g -wave molecular states, enable very rapid control of the atomic scattering properties. With the magnetic field being a free parameter in our optical trapping approach, we can take full advantage of this tunability of the s -wave scattering length.

For Cs in the $F = 3, m_F = 3$ ground state the process of three-body recombination is the dominant loss and heating mechanism [28]. In a recombination process, three atoms collide, two of them form a molecule, and the third atom takes away two thirds of the binding energy according to energy and momentum conservation. The atoms that form the molecule are usually lost, and the third atom is either lost or it deposits its share of the binding energy in the sample. Heating of the sample is the combination of "anti-evaporation" and recombination heating [28]. To a good approximation, the three-body recombination rate scales with the fourth power of the scattering length. Unfortunately, the prefactor in this scaling law is measured to be relatively large [28]. To minimize this heating, the recombination products should be removed quickly from the trap. It is thus important to assure that the sample is not operated too deeply in the hydrodynamic regime and that the evaporation is efficient in all directions. Arbitrarily increasing the scattering length to speed up the forced evaporation is therefore not possible without

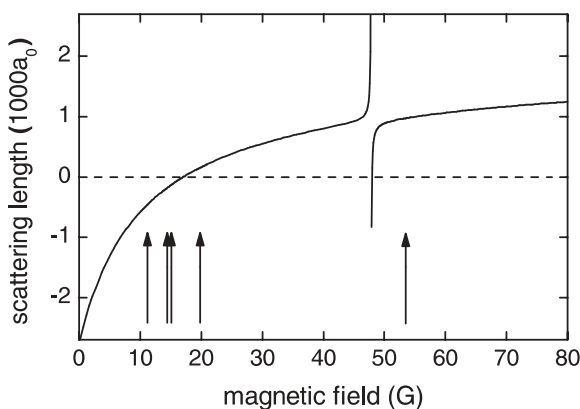


FIGURE 1 Scattering length as a function of magnetic field for the state $F = 3, m_F = 3$. There is a relatively broad Feshbach resonance at 48.0 G due to coupling to a d -wave molecular state. The arrows indicate several very narrow resonances at 11.0, 14.4, 15.0, 19.9 and 53.5 G, which result from coupling to g -wave molecular states. The data are taken from [13]

sacrificing cooling efficiency. Within these limits, tuning the scattering length allows for an optimization of the evaporation for given trap parameters. For example, for the low initial densities in a large reservoir trap the evaporation may be sped up by increasing the scattering length. In a later trapping stage with a higher atomic density the scattering length should be reduced to optimize the ratio of good to bad collisions.

3 BEC production

3.1 Overview of experimental strategy

For producing large condensates in optical dipole traps, it is necessary to independently optimize both trap loading and evaporative cooling. For initial loading of as many atoms as possible, an optical trap with large volume is needed which, in view of limited laser power, implies a shallow trapping potential. For subsequent forced evaporative cooling, however, high densities and fast elastic collisions require much tighter confinement. These two requirements in general demand dynamical changes of the trapping potential. A possible way to implement this is a spatial compression of the optical trap using e.g., a zoom-lens system [29]. Our approach is based on an alternative way where a sequence of optical trapping schemes is used to provide optimized loading together with optimized evaporative cooling.

We first use a shallow, large volume CO₂-laser trap as a "reservoir" for collecting the atoms before forced evaporative cooling is implemented in a tighter trap. The reservoir trap can be efficiently loaded with atoms that are precooled by Raman-sideband cooling [30]. This approach allows for the collection of atoms at moderate densities with little loss from three-body collisions and with negligible heating from either photon scattering or trap vibrations. It serves as a good starting point for the final transfer into a tighter optical trap. The tighter trap is adiabatically increased and adds a "dimple" to the trapping potential of the reservoir. Collisional loading of this dimple already yields a significant enhancement of the local number and phase-space density [31]. After turning off the reservoir trap excellent conditions for further forced evaporative cooling are obtained.

The different trap stages of optical trapping used in our experiments are illustrated in Fig. 2. An overview of the evolution of phase-space density and particle number for the various trapping stages is shown in Fig. 3.

The use of relatively weak optical trapping necessitates the implementation of magnetic "levitation" where a magnetic field gradient along the vertical direction compensates for the gravitational force. This levitation turns out to be very useful in two ways: First, in the limit of very weak optical trapping only one spin state is held in the trap. This assures perfect spin polarization of the sample¹. Further, efficient evaporation can be performed without the effect of gravitational sag in the trap. The dc magnetic field offset remains a free parameter for flexible tuning of the scattering length.

¹ This Stern–Gerlach separation technique also allows for radio-frequency evaporation along the vertical direction. Although one-dimensional, this type of evaporation has been applied to produce ultracold Cs atoms for studying three-body collisions [28].

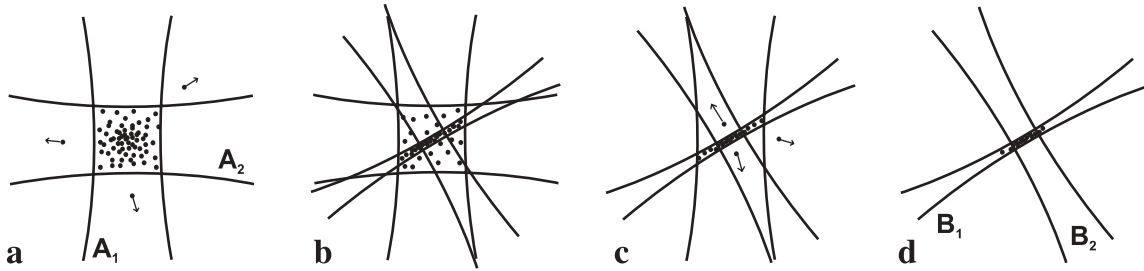


FIGURE 2 Illustration of the various stages of trap loading and evaporative cooling as seen from above. **(a)** Plain evaporation in a crossed CO₂-laser trap generated by beams A₁ and A₂ at a scattering length of $a = 1215 a_0$. **(b)** 1.5 s of ramping and collisional loading into a crossed 1064-nm fibre laser trap generated by beams B₁ and B₂ with a final scattering length $a = 210 a_0$. **(c)** Forced evaporative cooling after switching off CO₂-laser beam A₂. The power of all remaining lasers is ramped down, and the power in CO₂-laser beam A₁ is reduced to zero. **(d)** Final configuration of the crossed 1064-nm trap. Imaging is done in the horizontal plane at an angle of 30° with respect to the long axis of the cigar-shaped atomic cloud

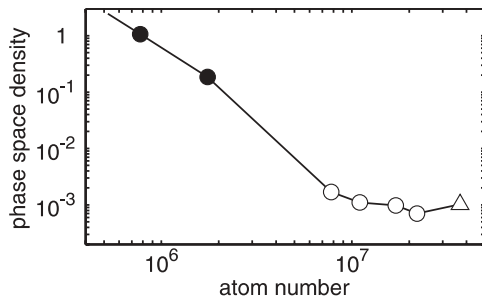


FIGURE 3 Peak phase space density as function of atom number. The path of evaporation proceeds from right to left. The *triangle* shows the atomic ensemble immediately after lattice cooling. The *open circles* show the ensemble in the reservoir trap after 0.08, 0.22, 0.64, and 2.0 s. The *filled circles* correspond to the sample in dimple trap right after loading and after 1.5 s of evaporation. The phase transition occurs after 2 s of forced evaporation with $\sim 5 \times 10^5$ atoms left in the dimple trap

3.2 Laser cooling

The initial collection and cooling of Cs atoms is achieved by conventional techniques. In a stainless steel vacuum chamber [32] atoms are loaded into a magneto-optical trap (MOT) from a Zeeman slowed atomic beam with up to 3×10^8 atoms after about 6 s. The MOT is operated on the $6^2S_{1/2}$, $F = 4$ to $6^2P_{3/2}$, $F' = 5$ transition. The ultra-high vacuum of less than 1×10^{-11} mbar gives 200 s for the $1/e$ -lifetime of the MOT. The MOT light is derived from a high power laser diode² referenced via beat-lock to a grating-stabilized master diode laser. Standard absorption imaging is used to determine particle numbers and temperatures.

We compress the atomic cloud by ramping up the magnetic field gradient in the MOT by a factor of five to 33 G/cm within 40 ms. Simultaneously we linearly change the detuning of the MOT laser from around 10 MHz to 30 MHz. At the end of the ramp, we switch off the MOT light and the magnetic field gradient. To cool the compressed cloud, we then apply degenerate Raman-sideband cooling [30] in an optical lattice to further cool and to polarize the atoms in the desired $F = 3$, $m_F = 3$ state. We have adapted the technique as described in [33] to our setup. This cooling scheme is particularly suited for polarizing atoms in the $F = 3$, $m_F = 3$ state because this is a dark state for which photon scattering is suppressed. Four laser beams derived from an injection

locked slave laser resonant with the $F = 4$ to $F' = 4$ transition produce a three-dimensional optical lattice, drive Raman-sideband transitions and repump out of the $F = 4$ ground state manifold. The total power of all the four beams is 65 mW and their $1/e^2$ -beam radii are about 1 mm. The oscillation frequency in the lattice is on the order of 100 kHz. A small magnetic field offset of several hundred mG is applied to induce the Raman-sideband cooling. We succeed in polarizing 90% of the atoms. The ensemble is then adiabatically released from the lattice after 6 ms of cooling time. If the atomic cloud is released into free space, the temperature of the ensemble with up to 4×10^7 atoms is about 0.7 μ K. For our typical atomic densities this corresponds to a phase space density of 1×10^{-3} .

3.3 Reservoir trap

We generate the large reservoir trap by horizontally crossing two CO₂-laser beams A₁ and A₂ at right angles as shown in Fig. 2a. At the same time we apply a magnetic gradient field in the vertical direction to levitate the atoms against gravity. The delivered powers in laser beams A₁ and A₂ are 90 W and 65 W, respectively. The light comes from two separate, highly stable linearly polarized single-frequency CO₂-lasers³. Switching of the beams is done by external acousto-optical modulators⁴ (AOMs). A₁ is downshifted in frequency by 40 MHz, whereas A₂ is upshifted by 40 MHz to prevent any interference. To avoid mode-hops the cooling water for the lasers needs to be stabilized to better than ± 20 mK. Still, a slow mode drift changes the power of the lasers by a few percent over the time scale of minutes. At the crossing point the $1/e^2$ -beam radii of the two lasers are (605 ± 35) μ m and (690 ± 35) μ m.

The magnetic fields for levitation and for Feshbach tuning are generated by two pairs of coils aligned with their axes parallel to the vertical direction. One pair in anti-Helmholtz configuration produces the vertical magnetic field gradient near 31.3 G/cm to levitate the atoms in the $F = 3$, $m_F = 3$ state. Another pair in Helmholtz configuration provides a variable bias field B₀ of up to 200 G. The combined field results in a weak outward directed force $F(\varrho) = m\alpha^2\varrho$ depend-

² SDL-5712-H1

³ Coherent-DEOS GEM-100L

⁴ Intraaction AGM-408BB1M

ing on the horizontal distance ϱ from the vertical symmetry axis. For perfect levitation of our atoms the constant $\alpha = g\sqrt{m/(3\mu_B B_0)}$ describes the curvature of the parabolic anti-trapping potential. The levitation field thus slightly reduces the trap depth along the horizontal direction. Here, m is the mass of Cs, g is the gravitational acceleration, and μ_B is Bohr's magneton. At $B_0 = 17$ G we have $\alpha = 2\pi \times 3.4$ Hz. The horizontal trap frequencies $\omega_{x,y}$ are reduced according to $\omega'_{x,y} = \sqrt{\omega_{x,y}^2 - \alpha^2}$. This is usually a very small effect for all but the lowest trap frequencies. Note that levitation also affects the horizontal motion of free atoms after the optical trap is shut off. The horizontal motion follows $\varrho(t) = \varrho_0 \cosh(\alpha t) + \alpha^{-1} v_0 \sinh(\alpha t)$ for initial position ϱ_0 and initial velocity v_0 . The vertical motion is not affected.

We excite vertical trap oscillations by briefly changing the vertical magnetic field gradient and hence tilting the trap. For exciting horizontal trap oscillations we shift the equilibrium position of the atoms by adding a horizontal magnetic field component. In both cases we monitor the center-of-mass oscillation of the atomic cloud after 50 ms time-of-flight. The geometrically averaged trap frequency $\bar{\nu}$ is calculated to be (12.6 ± 1.5) Hz which is in good agreement with the experimental value of (13.2 ± 0.2) Hz. Together with the levitation and the magnetic bias field the lasers provide an effective trap depth of about $k_B \times 7$ μ K. This trap depth is given by the weaker of the two CO₂-lasers as the atoms can escape along the direction of the stronger beam.

For transfer of the precooled atoms into the reservoir trap, we leave the light of the two CO₂-lasers on during the entire pre-cooling phase. This is because the CO₂-lasers show strong variations in beam pointing and beam shape as a function of radio-frequency power to the AOMs. We have checked that the small light shift introduced by the lasers does not affect the initial loading and cooling efficiency. The reservoir trap is then activated by ramping up the magnetic field and its gradient. The 1/e-rise time of the magnetic fields is limited to 1.5 ms because of eddy currents in the stainless steel chamber. We, therefore, do not expect the transfer to be fully adiabatic.

We find that the atoms are heated to about 2.2 μ K by the transfer into the reservoir trap. A clear measurement on the trapped sample is only possible after about 50 ms since the system initially is not in thermal equilibrium and since the untrapped atoms need to disappear from the field of view. We largely attribute the heating to imperfect phase space matching. In fact, the atomic cloud after Raman-sideband cooling to 0.7 μ K has a 1/e-radius of ~ 350 μ m. In comparison, an equilibrium distribution in the reservoir trap at 0.7 μ K would have a 1/e-radius of ~ 100 μ m. Potential energy is thus gained which is then turned into kinetic energy, effectively heating the cloud of atoms. Subsequently, the hot atoms evaporate out of the trap. For this phase of plain evaporation we set the magnetic bias field to 73.5 G. The scattering length is then 1215 a_0 . The temperature is reduced to less than 1 μ K within 10 s. After this time, we measure more than 4×10^6 atoms, corresponding to a peak phase space density of 2×10^{-3} .

3.4 Dimple trap

We proceed with loading of the dimple trap after 2 s of plain evaporation in the reservoir trap. At this point

the atom number is 7.8×10^6 and the phase space density is 1.7×10^{-3} (see Fig. 3). The dimple trap is generated by horizontally intersecting one tightly focused laser beam B₁ with 34- μ m waist and another less focused beam B₂ with 260- μ m waist at right angles, rotated by 30° in the horizontal plane with respect to the CO₂-laser beams as shown in Fig. 2d. This is different from our earlier work [4] where we have used CO₂-laser beam A₂ for axial confinement. We introduce the B₂ beam because some weak back reflections of the CO₂-laser beams led to a slight undesirable corrugation of the optical potential. This complicated the quantitative analysis of the BEC. Beams B₁ and B₂ are derived from a broadband fiber laser⁵ at 1064 nm. The powers in these beams are ramped up within 1.5 s to a maximum power of 70 mW for B₁ and 270 mW for B₂. The trapping in the dimple is now briefly done by all four laser beams with B₁ providing most of the radial and A₁ most of the axial confinement. After switching off beam A₂, we measure the radial and axial trap frequencies in the dimple to (221.2 ± 1.6) Hz and (14.2 ± 0.1) Hz, respectively. During the ramping up phase of B₁ and B₂ we reduce the magnetic field offset to 23 G and thus the scattering length to 300 a_0 in order to reduce losses from three-body recombination [28]. The trap now contains about 1.7×10^6 atoms at a peak phase space density of approximately 0.13.

3.5 Forced evaporation towards BEC

We start forced evaporative cooling by ramping down the power in all three remaining beams. Simultaneously we remove the reservoir by switching off the CO₂-laser A₂ that is not responsible for axial confinement. To assure a well-defined ramp over a large intensity range we control the light power of the near-infrared beam B₁ by means of a logarithmic photodiode and a servo loop. The power in CO₂-laser beam A₁ is ramped to zero within 5.5 s so that B₂ at the end of evaporation exclusively assures axial confinement. The change in beam pointing for A₂ does not affect the evaporation. For B₁ we approximately follow an exponential ramp over 5.5 s. The power in beam B₂ is only slightly reduced. The final power in B₁ and B₂ is 0.5 mW and 220 mW. We find and optimize this ramp by extending the ramp in discrete time steps of a few hundred milliseconds at the beginning and up to one second towards the end of the ramp.

At each step we search for a maximum in evaporation efficiency $\gamma = \log(D'/D)/\log(N/N')$ as a function of the trap depth and scattering length [34]. Here, D and D' are the phase-space densities at the beginning and end of each step, N and N' denote the respective particle numbers. Maximizing γ at each step results in an overall optimization of the evaporation path. We find that a magnetic field value of 21 G with scattering length $a = 210 a_0$ is optimal during the forced evaporation phase. As can be seen from Fig. 3 the efficiency γ lies around 3 during the forced evaporation ramp. We attribute this high efficiency to the fact that atoms can escape the trap into almost all directions because of the levitation field.

We observe the phase transition after 2 s of forced evaporative cooling with about 5×10^5 atoms at a temperature of (200 ± 10) nK. At this point the power in beams B₁ and B₂ is

⁵ IPG Laser PYL-10

8.7 mW and 250 mW. The duration of the ramp is relatively short. Our evaporation proceeds close to the hydrodynamic regime. Thus, significant improvement of the evaporation is not to be expected.

Further evaporation leaves a cigar-shaped condensate with the long axis in the horizontal plane. In Fig. 4 we show vertical density profiles of expanding condensates. The tunability of the scattering length allows us to explore different regimes of expansion. For Fig. 4a we expand the condensate at the creation scattering length of $210 a_0$. This is the usual type of self-similar expansion in which the condensate in the Thomas–Fermi regime retains its parabolic shape [35]. For Fig. 4b we step the scattering length to zero at the moment of release from the trap. The mean-field interaction thus vanishes and the rate of expansion is greatly reduced. This exposes a small thermal component, for which a bimodal fit reveals a temperature of around 10 nK. The critical temperature at these trapping conditions is 24 nK; therefore, the expected condensate fraction agrees well with the measured value of 91%. From the fit to the data in Fig. 4 we obtain that there are up to 1.1×10^5 atoms in the condensate with a 20% calibration error. The error does not come from the fit but from the overall uncertainty in determining the atom number. Usually, the error from absorption imaging alone is around 50%, but we can calibrate the atom number from measurements on the chemical poten-

tial, see Sect. 4.1. For this particular experiment we measure the final trap frequencies to (4.3 ± 0.2) Hz and (21.1 ± 0.2) Hz along the axial and radial direction, respectively. We thus infer for the initial Thomas–Fermi sizes $R_r^{\text{TF}} = (8.7 \pm 0.3)$ μm and $R_a^{\text{TF}} = (42.5 \pm 1.2)$ μm along the radial and axial directions at a scattering length of $a = 210 a_0$. The peak density of the condensate is $n_0 = (2.1 \pm 0.1) 10^{13}$ cm^{-3} .

4 Tunable quantum gas

We now test the tunability of the condensate interaction. We first study the condensate expansion as a function of scattering length [36] in two different ways. We then specialize to the case when the interaction energy is switched off and present improved results on the ultra-slow expansion of the condensate in comparison with earlier measurements in [4]. Finally, we excite compression oscillations of the trapped condensate by suddenly stepping the scattering length to a lower value.

4.1 Expansion energy as a function of scattering length

We measure the release energy of the condensate for slow and fast changes of the scattering length. When we slowly vary the scattering length the wave function of the trapped condensate can follow adiabatically and the condensate remains in equilibrium. The release energy is proportional to the chemical potential of the condensate at the given value of the scattering length. The situation is different when we rapidly switch the scattering length at the moment of condensate release. The condensate then expands from a non-equilibrium state because the wave function has not had time to adjust to the change in interaction energy. This leads to strong changes for the rate of condensate expansion in comparison to the expansion from equilibrium.

We first consider a condensate in the Thomas–Fermi regime for which we adiabatically ramp the scattering length to a new value. For such a condensate, the release energy E_{rel} directly corresponds to the chemical potential μ_{TF} through $\frac{7}{2} E_{\text{rel}} = \mu_{\text{TF}}$ [35], which is given by

$$\mu_{\text{TF}} = \frac{\hbar \bar{\nu}}{2} \left(\frac{15N}{a_{\text{ho}}} \right)^{2/5} a^{2/5}. \quad (1)$$

Here, $\bar{\nu}$ is the geometric average of the trap frequencies, N is the particle number in the condensate, and $a_{\text{ho}} = \sqrt{\hbar/(m2\pi\bar{\nu})}$ is the oscillator length. For the experiment we produce a condensate with $N = 8.5 \times 10^4$ atoms at a creation scattering length of $a_c = 210 a_0$. We then slowly ramp the magnetic field to a value between 20 and 35 G, setting the scattering length to a value between about 200 and 700 a_0 . The slow ramping excludes values below the Feshbach resonance at 19.9 and above the one at 48.0 G because of strong loss⁶. The condensate is then released from the trap and we measure the release energy. The results are shown in Fig. 5. Here we assume that the magnetic field strength translates into scattering length according to Fig. 1. The data is well fit by a function of the

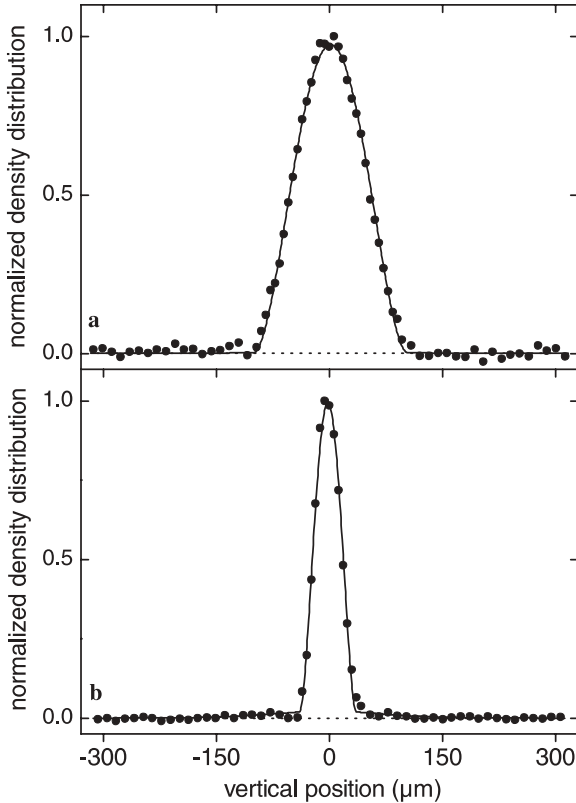


FIGURE 4 Vertical density profiles of Cs condensates after 100 ms of free expansion in the levitation field. The *solid curves* are fits to the data for the Thomas–Fermi profiles which include possible thermal components. For better distinction the baseline is dashed. **(a)** Expansion with no change in scattering length. The total number of atoms in the condensate is $N = 1.1 \times 10^5$. **(b)** Expansion near zero scattering length under the same conditions reveals a small thermal component with a temperature of about 10 nK

⁶ A combination of slow ramping and quick jumping at the Feshbach resonances would allow access to the full range of values for the scattering length.

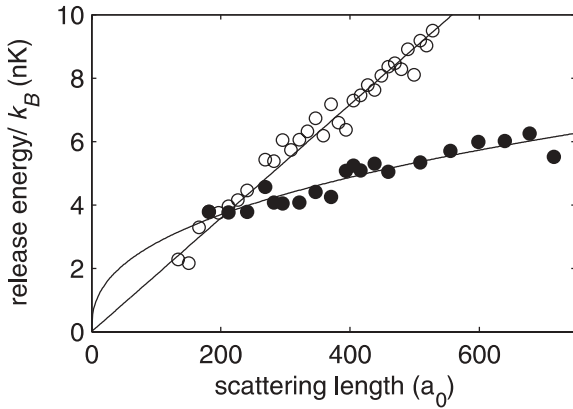


FIGURE 5 Release energy of the condensate as a function of scattering length a . The *filled circles* represent experimental data for the case of adiabatic ramping of a trapped condensate. The data, corresponding to $2/7$ of the chemical potential at a given value of the scattering length, are fit by $C a^{2/5}$. The *open circles* represent data for rapid switching at the moment of condensate release. As discussed in the text, the straight line is not a fit. It connects the origin with the fitted value of the release energy at the creation scattering length

form $Ca^{2/5}$ according to (1). From the fit parameter C we can deduce an independent estimate of the particle number $N = (8.2 \pm 1.3) \times 10^4$. The error is dominated by the error in determining the trap frequencies.

For a sudden change of the scattering length the condensate wave function has no time to react. For example, for an increase of the scattering length the density distribution is too narrow in comparison to the equilibrium density distribution at the new value of the scattering length. The condensate thus expands more rapidly than a condensate in equilibrium at this new value. Since the mean-field interaction energy of the condensate scales linearly with the scattering length for a given density profile [35], we expect a linear behavior of the release energy as a function of the final scattering length a . In Fig. 5 we thus compare the data for the measured release energy to a straight line $Ca_c^{2/5} a/a_c$ given by the origin and the fitted value of the release energy at the creation scattering length $a_c = 210 a_0$. We find good agreement with the linear dependence.

4.2 Ultra-slow condensate expansion

We now study the expansion of the condensate near the zero-crossing of the scattering length. At the moment of condensate release, we rapidly switch the magnetic field from the creation field near 20 G to (17.17 ± 0.05) G, corresponding to $a = (3.4 \pm 3.0) a_0$. The error in determining the precise magnetic field at the position of condensate requires that we choose a slightly positive value of the scattering length to assure that no weakly attractive interactions modify the condensate expansion. The levitation field remains on, allowing for an extended observation period because the atoms then do not fall under gravity. Figure 6 shows the vertical and horizontal extent of a BEC with 1.2×10^5 atoms as a function of time after release from the trap. We only show the data after 75 ms of expansion when the optical density of the atomic cloud is sufficiently reduced to allow for reliable absorption imaging. The horizontal expansion is dominated by the magnetic

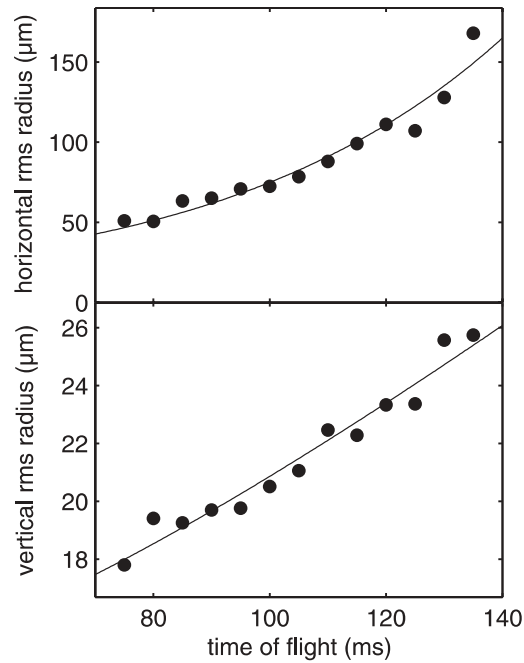


FIGURE 6 Expansion of the non-interacting condensate. The data points show the horizontal (above) and vertical (below) rms radius of the BEC as a function of expansion time near the zero crossing of scattering length. Note the different scales. The fit to the residual vertical expansion reveals a release energy of $k_B \times (51 \pm 3)$ pK. For the horizontal expansion the data are fit by $A \cosh(\alpha t)$ with $\alpha = 2\pi \times (3.20 \pm 0.23)$ Hz

anti-trapping potential which derives from the presence of the levitation field and which magnifies the atomic cloud according to the cosine hyperbolic function, see Sect. 3.3. The measured rate of expansion $2\pi \times (3.20 \pm 0.23)$ Hz agrees reasonably well with the expected rate constant $\alpha = 2\pi \times 3.4$ Hz. The vertical expansion corresponds to a release energy of $k_B \times (51 \pm 3)$ pK. Note that this is much lower than the kinetic energy of the ground state $\hbar\omega_r/4 = k_B \times 253$ pK given by a radial trap frequency of $\omega_r = 2\pi \times 21.1$ Hz. It is remarkable that the release energy is less than the zero-point energy of the ground state. Since the spatial extent of the condensate is much larger than the size of the ground state wave function of the harmonic oscillator, the momentum spread, limited by the uncertainty of the wave function of the initial condensate, is lower than that of the ground state.

4.3 Condensate oscillations

By rapidly ramping the scattering length it is possible to excite oscillations of the condensate in the trap [37]. In fact, in the limit of a cigar shaped condensate one expects radial “compression” or “expansion oscillations” at twice the trap frequency. Compression oscillations can be seen in Fig. 7 where we plot the vertical radius of the released condensate as a function of hold time t_h in the trap. To excite the oscillation we step the scattering length from a value of $a = 363 a_0$ ($B = 24.4$ G) to $a = 25 a_0$ ($B = 17.6$ G) at time t_0 . The condensate is then allowed to oscillate in the trap for a variable hold time t_h at the final value of the scattering length. We release the condensate at time $t_0 + t_h$ and take an image after 80 ms of free expansion. We fit the data

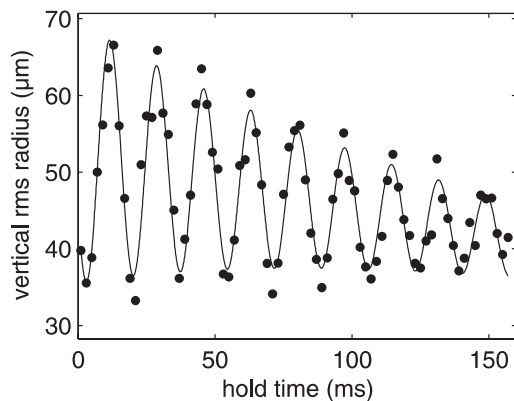


FIGURE 7 Condensate oscillations after rapid switching of the scattering length. The *filled circles* show the vertical rms radius of an expanding BEC with 7×10^4 atoms after 80 ms of free expansion as a function of hold time in the trap. The scattering length has been switched rapidly from $363 a_0$ to $25 a_0$. The *solid curve* is a fit to the data giving an oscillation frequency of (58.3 ± 0.2) Hz. We independently measure the radial trap frequency to (28 ± 1) Hz

by a sinusoidal function. The measured compression oscillation frequency of (58.3 ± 0.2) Hz agrees well with twice the radial trap frequency of $2 \times (28 \pm 1)$ Hz at the given trapping power. To account for the damping we have to introduce an exponential decay of the amplitude and of the offset value. The damping of the amplitude has a time constant of 126 ms. We have not yet identified the origin of this damping. Possibly the BEC samples different trapping frequencies due to the large amplitude of the oscillation, which would lead to an apparent damping. Also, damping might be caused by the interaction with a residual thermal cloud or by parametric processes [38].

5 Conclusion

We have shown that essentially pure Cs condensates can be produced with more than 10^5 atoms. In our optical trap it is possible to flexibly change the atomic scattering properties. The atomic condensate can now be used as the starting point for experiments where a tuning and ramping of the scattering properties can be exploited. It will be interesting to study the case of a non-interacting condensate at the zero-crossing of the scattering length. Such a condensate might be used in atom interferometers where one wishes to suppress any mean-field effects [39]. On the other hand, tuning to large values of the scattering length might allow the investigation of effects beyond the mean-field approximation [35]. Also, modulation of the scattering length could be used as an alternative tool to probe the excitation spectrum of the condensate. Finally, ultracold Cs_2 molecules can be created by ramping across one of the Feshbach resonances [8] and the transition from an atomic to a molecular condensate could then be studied.

ACKNOWLEDGEMENTS This work is supported by the Austrian ‘‘Fonds zur F6rderung der wissenschaftlichen Forschung’’ (FWF) within SFB 15 (project part 16) and by the European Union in the frame of the Cold Molecules TMR Network under Contract No. HPRN-CT-2002-00290. M.M. is supported by DOC [Doktorandenprogramm der 6sterreichischen

Akademie der Wissenschaften]. C.C. is supported by a Lise-Meitner-Fellowship from the FWF.

REFERENCES

- 1 M. Barrett, J. Sauer, M. Chapman: Phys. Rev. Lett. **87**, 010404 (2001)
- 2 Y. Takasu, K. Maki, K. Komori, T. Takano, K. Honda, M. Kumakura, T. Yabuzaki, Y. Takahashi: Phys. Rev. Lett. **91**, 040404 (2003)
- 3 G. Cennini, G. Ritt, C. Geckeler, M. Weitz: Phys. Rev. Lett. **91**, 240408 (2003)
- 4 T. Weber, J. Herbig, M. Mark, H.-C. N6agerl, R. Grimm: Science **299**, 232 (2003)
- 5 D. Rychtarik, B. Engeser, H.-C. N6agerl, R. Grimm: Phys. Rev. Lett. **92**, 173003 (2004)
- 6 C. Chin, A.J. Kerman, V. Vuletić, S. Chu: Phys. Rev. Lett. **90**, 033201 (2003)
- 7 C.A. Regal, C. Ticknor, J.L. Bohn, D.S. Jin: Nature **424**, 47 (2003)
- 8 J. Herbig, T. Kraemer, M. Mark, T. Weber, C. Chin, H.-C. N6agerl, R. Grimm: Science **301**, 1510 (2003)
- 9 S. D6urr, T. Volz, A. Marte, G. Rempe: Phys. Rev. Lett. **92**, 020406 (2004)
- 10 K. Xu, T. Mukaiyama, J.R. Abo-Shaeer, J.K. Chin, D.E. Miller, W. Ketterle: Phys. Rev. Lett. **91**, 210402 (2003)
- 11 S. Jochim, M. Bartenstein, A. Altmeyer, G. Hendl, S. Riedl, C. Chin, J. Hecker Denschlag, R. Grimm: Science **302**, 2101 (2003)
- 12 M. Greiner, C.A. Regal, D.S. Jin: Nature **426**, 537 (2003)
- 13 C. Chin, V. Vuletić, A.J. Kerman, S. Chu, E. Tiesinga, P.J. Leo, C.J. Williams: Phys. Rev. A **70**, 032701 (2004)
- 14 E.A. Donley, N.R. Claussen, S.T. Thomson, C.E. Wieman: Nature **417**, 529 (2002)
- 15 L. Radzihovsky, J. Park, P.B. Weichman: Phys. Rev. Lett. **92**, 160402 (2004)
- 16 M.W.J. Romans, R.A. Duine, S. Sachdev, H.T.C. Stoof: Phys. Rev. Lett. **93**, 020405 (2004)
- 17 J. S6oding, D. Gu6ry-Odelin, P. Desbiolles, G. Ferrari, J. Dalibard: Phys. Rev. Lett. **80**, 1869 (1998)
- 18 J. Arlt, P. Bance, S. Hopkins, J. Martin, S. Webster, A. Wilson, K. Zetie, C.J. Foot: J. Phys. B **31**, L321 (1998)
- 19 D. Gu6ry-Odelin, J. S6oding, P. Desbiolles, J. Dalibard: Europhys. Lett. **44**, 26 (1998)
- 20 D. Gu6ry-Odelin, J. S6oding, P. Desbiolles, J. Dalibard: Optics Express **2**, 323 (1998)
- 21 S.A. Hopkins, S. Webster, J. Arlt, P. Bance, S. Cornish, O. Marag6, C.J. Foot: Phys. Rev. A **61**, 032707 (2000)
- 22 P.J. Leo, E. Tiesinga, P.S. Julienne, D.K. Walter, S. Kadlecsek, T.G. Walker: Phys. Rev. Lett. **81**, 1389 (1998)
- 23 A.M. Thomas, S. Hopkins, S.L. Cornish, C.J. Foot: J. Opt. B **5**, S107 (2003)
- 24 H. Perrin, A. Kuhn, I. Bouchoule, C. Salomon: Europhys. Lett. **42**, 395 (1998)
- 25 V. Vuletić, A.J. Kerman, C. Chin, S. Chu: Phys. Rev. Lett. **82**, 1406 (1999)
- 26 M. Hammes, D. Rychtarik, V. Druzhinina, U. Moslener, I. Manek-H6nninger, R. Grimm: J. Mod. Opt. **47**, 2755 (2000)
- 27 D.-J. Han, M.T. DePue, D.S. Weiss: Phys. Rev. A **63**, 023405 (2001)
- 28 T. Weber, J. Herbig, M. Mark, H.-C. N6agerl, R. Grimm: Phys. Rev. Lett. **91**, 123201 (2003)
- 29 D.-J. Han, M.T. DePue, D.S. Weiss: Phys. Rev. A **63**, 023405 (2001)
- 30 A.J. Kerman, V. Vuletić, C. Chin, S. Chu: Phys. Rev. Lett. **84**, 439 (2000)
- 31 D.M. Stamper-Kurn, H.-J. Miesner, A.P. Chikkatur, S. Inouye, J. Stenger, W. Ketterle: Phys. Rev. Lett. **81**, 2194 (1998)
- 32 T. Weber: PhD thesis, Univ. Innsbruck 2003
- 33 P. Treutlein, K.Y. Chung, S. Chu: Phys. Rev. A **63**, 051401 (2001)
- 34 W. Ketterle, N.J. Van Druten: Adv. At. Mol. Opt. Phys. **37**, 181 (1996)
- 35 L. Pitaevskii, S. Stringari: *Bose–Einstein Condensation* (Clarendon Press, Oxford 2003)
- 36 S.L. Cornish, N.R. Claussen, J.L. Roberts, E.A. Cornell, C.E. Wieman: Phys. Rev. Lett. **85**, 1795 (2000)
- 37 Y. Kagan, E.L. Surkov, G.V. Shlyapnikov: Phys. Rev. Lett. **79**, 2604 (2001)
- 38 F. Chevy, V. Bretin, P. Rosenbusch, K.W. Madison, J. Dalibard: Phys. Rev. Lett. **88**, 250402 (2002)
- 39 S. Gupta, K. Dieckmann, Z. Hadzibabic, D.E. Pritchard: Phys. Rev. Lett. **89**, 140401 (2002)

B.3 Efficient creation of molecules from a cesium Bose-Einstein condensate

M. Mark, T. Kraemer, J. Herbig, C. Chin, H.-C. Nägerl, and R. Grimm
Europhys. Lett. **69**, 706 (2005). cond-mat/0409737

Efficient creation of molecules from a cesium Bose-Einstein condensate

M. MARK¹, T. KRAEMER¹, J. HERBIG¹, C. CHIN¹,
H.-C. NÄGERL¹ and R. GRIMM^{1,2}

¹ *Institut für Experimentalphysik, Universität Innsbruck
Technikerstraße 25, 6020 Innsbruck, Austria*

² *Institut für Quantenoptik und Quanteninformation
Österreichische Akademie der Wissenschaften - 6020 Innsbruck, Austria*

received 29 September 2004; accepted in final form 12 January 2005

published online 2 February 2005

PACS. 03.75.-b – Matter waves.

PACS. 34.50.-s – Scattering of atoms and molecules.

PACS. 32.80.Pj – Optical cooling of atoms; trapping.

Abstract. – We report a new scheme to create weakly bound Cs₂ molecules from an atomic Bose-Einstein condensate. The method is based on switching the magnetic field to a narrow Feshbach resonance and yields a high atom-molecule conversion efficiency of more than 30%, a factor of three higher than obtained with conventional magnetic-field ramps. The Cs₂ molecules are created in a single g -wave rotational quantum state. The observed dependence of the conversion efficiency on the magnetic field and atom density shows scattering processes beyond two-body coupling to occur in the vicinity of the Feshbach resonance.

The newly emerging field of quantum-degenerate molecules provides intriguing possibilities for controlled studies of multicomponent matter-wave systems. Chemical reactions are expected to show effects of coherence, matter-wave interference, quantum tunneling, and bosonic stimulation. Recently, coherent atom-molecule couplings [1] have been observed in a Bose-Einstein condensate (BEC), and molecular quantum gases [2,3] and molecular BECs [4] have been realized. The key ingredient in these experiments has been the presence of magnetically induced Feshbach resonances [5]. These resonances provide the variable coupling between atoms and molecules as a function of an external magnetic field and allow the conversion of atoms to molecules and vice versa.

In the previous experiments on the creation of ultracold Cs₂, Na₂ and Rb₂ molecules from the corresponding atomic BECs [2,3,6] the molecules are formed by ramping the magnetic field through a Feshbach resonance; see illustration in fig. 1. It is expected that during the ramping process the ground-state atom population in the trap is adiabatically and efficiently converted into molecules in a weakly bound state [7]. However, the reported efficiencies using this method are relatively low: Typically 5%–10% are observed, whereas up to 50% to 70% of the atoms are lost during the ramping process. The missing fraction, the lost atoms which are not converted into weakly bound molecules, is generally believed to result from the creation

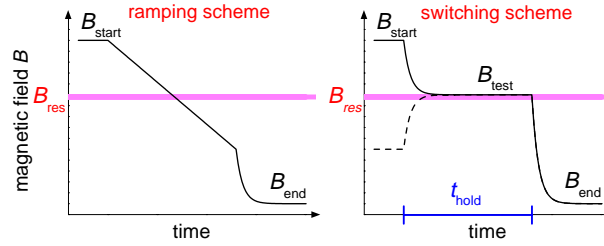


Fig. 1 – Schemes for molecule creation near a Feshbach resonance, located at B_{res} . In the ramping scheme, we linearly ramp the magnetic field from B_{start} , well above the resonance, to some value well below the resonance, and then quickly to B_{end} . In the switching scheme, we first switch from B_{start} to B_{test} . After a hold time t_{hold} , we switch the field to B_{end} . The switching scheme also works for B_{start} below the resonance (dashed line). The finite response time of the magnetic field in our experiment is due to eddy currents in the stainless-steel vacuum chamber.

of molecules in states which cannot be detected by the conventional imaging method, or to consist of “hot” atoms which quickly leave the trap [2,8].

In this paper, we report a high atom-molecule conversion efficiency in excess of 30% from an atomic BEC based on a novel switching scheme. This scheme is illustrated in fig. 1. The magnetic field is quickly switched from an off-resonant value B_{start} to a field B_{test} , near the resonance position B_{res} . After a variable hold time t_{hold} , the magnetic field is quickly lowered well below the resonance B_{end} , where atoms and molecules decouple and can be independently measured. Our new scheme works for initial magnetic fields B_{start} both well above or well below the resonance. In the latter case, the creation of molecules cannot be explained in terms of the two-body adiabatic conversion picture [7]. An investigation on the atom loss and molecule creation efficiencies suggests that different scattering processes are involved near the narrow Feshbach resonance.

The cesium molecules we create are of special interest since they have a large orbital angular momentum ($l = 4$). Coupling from ultracold atoms in an s -wave scattering state to the g -wave molecular states is observed only for cesium atoms due to the large indirect spin-spin coupling [9]. Many narrow Feshbach resonances of this kind were observed at low magnetic fields for cesium atoms polarized in the lowest internal state $|F = 3, m_F = 3\rangle$ [10], where F is the total angular momentum and m_F is the magnetic quantum number. Based on these narrow resonances, the formation of thermal molecules was investigated [11] and a pure molecular quantum gas was created from an atomic BEC [2].

Our experiments start with a pure BEC of cesium with up to 2.2×10^5 atoms in the ground state $|F = 3, m_F = 3\rangle$ [12,13]. The magnetic field is set to 21 G, corresponding to an atomic scattering length of $210a_0$, where a_0 is the Bohr radius. The magnetic field gradient is set to 31.3 G/cm for levitation of the atoms [12]. The condensate is confined in a crossed dipole trap formed by two horizontally intersecting laser beams, which are derived from a broad-band Yb fiber laser at 1064 nm. One tightly focused beam with a waist of $35 \mu\text{m}$ and a power of 0.5 mW essentially provides the radial confinement; the other beam with a waist of $300 \mu\text{m}$ and power of 350 mW essentially provides the axial confinement. The radial and axial trap frequencies are $\omega_r/2\pi = 17.5 \text{ Hz}$ and $\omega_z/2\pi = 4.7 \text{ Hz}$, respectively. The chemical potential is $k_B \times 11 \text{ nK}$, where k_B is Boltzmann’s constant.

Before we start the molecule creation, we first compress the condensate by adiabatically increasing the power of the tightly focused laser in 0.7 s to 40 mW. The higher laser power provides a stronger trapping force and allows us to turn off the levitation field. The absence

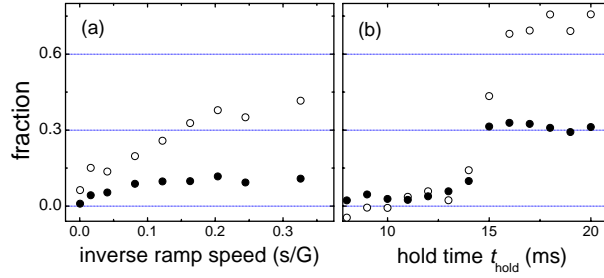


Fig. 2 – Comparison of the two schemes of molecule creation. Molecule fraction (solid circles) and atom loss fraction (open circles) are shown for (a) the ramping scheme, where the fractions are measured for different ramp speeds, and for (b) the switching scheme for different hold times t_{hold} . In (b), B_{test} is set right on resonance.

of the magnetic field gradient is crucial to ensure that all atoms experience the same magnetic field and can simultaneously participate in the molecule formation process. In the compressed trap, the trap frequencies are $\omega_r/2\pi = 170$ Hz and $\omega_z/2\pi = 6.5$ Hz, the chemical potential is $k_B \times 86$ nK and the peak density is 1.7×10^{14} cm $^{-3}$. We then slowly change the magnetic field in 200 ms to a starting value of B_{start} , typically 0.5 G above the Feshbach resonance B_{res} . Note that this 0.5 G offset is much larger than the resonance width of a few mG. The condensate at B_{start} is not influenced by the resonance. We then switch off the dipole trap and release the atoms into free space and, at the same time, tune the magnetic field toward the Feshbach resonance to create molecules. At the end of the molecule formation phase, we quickly lower the magnetic field down to $B_{\text{end}} \approx 18$ G to decouple the molecules and atoms.

The resulting molecule and atom numbers can be determined independently by absorption imaging [2]. The atoms are directly imaged at 18 G. We verify that the molecules are insensitive to the imaging beam at this magnetic field. To detect the molecules, we first blast away the atoms at 18 G with a resonant beam [3], and then ramp the magnetic field back above the resonance to 21 G. The weakly bound molecular state is then above the continuum and the molecules quickly dissociate into free atoms [14]. By imaging the cloud of the resulting atoms, we can determine the molecule number. We define the corresponding molecule fraction as the number of atoms detected after dissociation normalized to the initial atom number. This is then, by definition, equal to the atom-molecule conversion efficiency.

We employ both the ramping scheme and the switching scheme for molecule production (see fig. 1) and compare their performances. In the ramping scheme, we tune the magnetic field across the resonance with a constant ramping speed. Based on the resulting molecule number and the loss in atomic number, we calculate the conversion fractions, shown in fig. 2(a). A maximum molecule fraction of 10% is observed when the ramps are slower than 10 G/s. The atom loss for these ramps is about 40%, which indicates a missing fraction of about 30%. This result is similar to all previous experiments using the same method [2,3,6]. For the switching scheme, we quickly tune the magnetic field onto the Feshbach resonance $B_{\text{test}} \approx B_{\text{res}}$, wait for various hold times t_{hold} , and quickly lower the magnetic field to $B_{\text{end}} = 18$ G. Due to the finite response time of the magnetic field, the field approaches the Feshbach resonance after about 12 ms [15]. At this time, the peak density of the expanding condensate reduces to 1.1×10^{12} cm $^{-3}$ [16]. For hold times $t_{\text{hold}} > 15$ ms, molecule fractions of 30 ~ 35% and atom loss fractions of ~ 70% are reached as shown in fig. 2(b). The conversion efficiency is by more than a factor of three higher than obtained from the ramping scheme. Note that in order

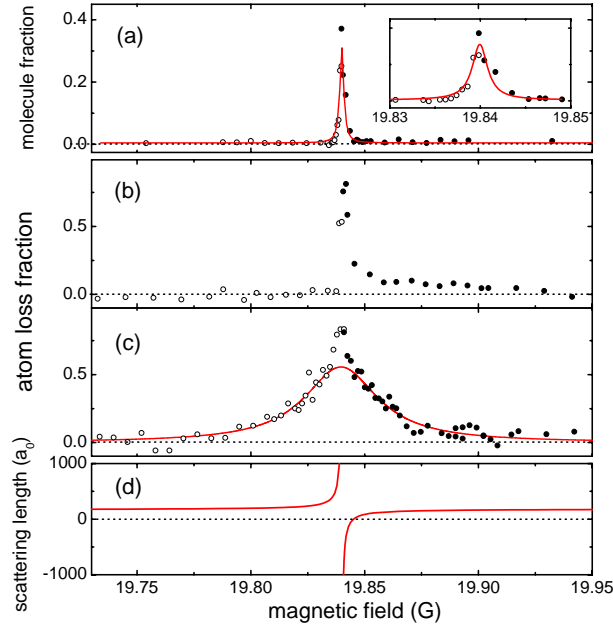


Fig. 3 – Molecule creation and atom loss near the Feshbach resonance. Based on the switching scheme, molecule increase in $t_{\text{hold}} = 18$ ms (a) and atom loss in 18 ms (b) are measured for various test fields B_{test} . The inset shows the expanded view of the molecule signal. For comparison, the atom trap loss in the compressed trap is shown in (c). The scattering length is shown in (d) for reference. Solid circles (open circles) show the measurements above (below) the resonance. In (a), a Lorentzian fit (solid line) yields a width of 2.1 mG and the resonance position of $B_{\text{res}} = 19.840$ G, subject to a calibration uncertainty of 4 mG. Fitting both wings in (c) gives a Lorentzian width of 40(2) mG.

to precisely set the magnetic field right on the narrow Feshbach resonance, we synchronize the experiment with the 50 Hz line voltage to reduce the effects of the ambient magnetic-field ripple, for which we measure an amplitude of 4 mG. This suppresses uncontrolled magnetic-field variations to about 1 mG.

To understand the different performance of the two schemes, we study the atom loss and molecule increase at different magnetic fields B_{test} based on the switching scheme, see fig. 3(a) and (b). For comparison, we also show the atom loss in the compressed trap in fig. 3(c), where the initial peak density is $1.9 \times 10^{14} \text{ cm}^{-3}$ [17]. The calculated scattering length is shown in fig. 3(d) [18]. For all measurements with B_{test} above the resonance, we prepare the condensate as previously described at $B_{\text{start}} = B_{\text{res}} + 0.5$ G. For B_{test} below the resonance, we prepare the condensate at a magnetic field below the resonance by quickly switching the magnetic field from the initial value to $B_{\text{res}} - 0.5$ G. No appreciable atom loss, molecule formation or condensate excitation is observed in this process. We then follow the same experimental procedure, but approach the resonance from below. These two different preparation procedures for magnetic fields above and below the resonance are necessary to avoid a slow field-sweep across the resonance, which can lead to systematic atom loss or molecule increase.

In the molecule creation spectrum (fig. 3(a)) we observe a very narrow linewidth of 2.1 mG, which is consistent with the predicted resonance width. Notably, our molecule creation scheme also works for B_{start} below the resonance, which suggests that coupling beyond the adiabatic

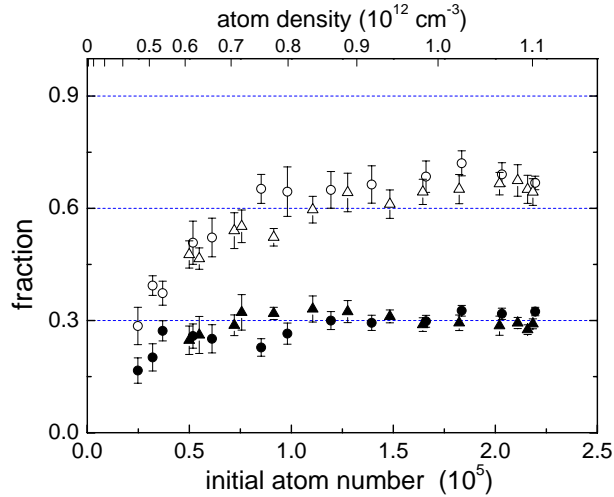


Fig. 4 – Density dependence of the atom loss fraction (open symbols) and molecule fraction (solid and open circles). The atom number in the BEC is varied by either adjusting optical cooling efficiencies (solid and open circles) or the loading efficiencies into the crossed dipole trap (solid and open triangles). The corresponding atomic density of the sample right before the molecule formation (after 12 ms expansion in free space) is given on the top axis.

conversion model plays an important role in the creation process. In the adiabatic passage picture, molecules cannot be created when the creation field is below the resonance. The atom loss, shown in fig. 3(b), is asymmetric and seems to include two components, a narrow peak on resonance and a much broader and weaker loss feature for magnetic fields above the resonance. The narrow peak has a similar width as in the molecule production spectrum in fig. 3(a), and is clearly related to the observed molecule formation. The broad and weak feature on the high magnetic-field side has a width of 80(20) mG as determined from a one-sided Lorentzian fit. To obtain further information about the atom loss process, we measure the atom loss in the compressed trap, where the atom density is higher by a factor of ~ 170 than in fig. 3(a) and (b). The result shown in fig. 3(c) displays a wide and symmetric loss feature. By fitting the two wings to a Lorentzian profile, we find a width of 40(2) mG.

The different lineshapes suggest that different scattering processes are involved near the Feshbach resonance. The molecule formation width is close to the predicted width of the Feshbach resonance and can be interpreted in terms of the two-body Feshbach coupling. The asymmetric loss feature in fig. 3(b) and the trap loss may be due to three-body recombination or many-body effects. These broad atom loss features are puzzling, since they are a factor of 20 or more wider than the Feshbach resonance width of 2 mG. The physical origin of the associated loss mechanisms requires further investigation.

The large width of the atom loss feature, however, does provide a qualitative explanation why the switching scheme is more efficient than the ramping scheme. In a linear ramp, atoms sample all magnetic fields near the resonance which, for a large fraction of time, leads to atom loss without molecule increase. With the switching scheme, the atoms spend more time in the magnetic-field range where the molecules can be created.

To further investigate and differentiate the physical mechanisms that are responsible for the missing fraction and for the molecule increase, we measure the dependence of the atom loss

fraction and molecule fraction on the atom number in the condensate, as shown in fig. 4. Atom numbers ranging from 2.5×10^4 to 2.2×10^5 correspond to peak densities of $7.9 \times 10^{13} \text{ cm}^{-3}$ to $1.9 \times 10^{14} \text{ cm}^{-3}$ in the compressed trap and to $4.6 \times 10^{11} \text{ cm}^{-3}$ to $1.1 \times 10^{12} \text{ cm}^{-3}$ in free space at the moment the molecules are created. For the calculation of the densities in free space, we take into account the 12 ms expansion of the condensate in the Thomas-Fermi regime after the dipole trap is turned off.

Several interesting features show up in the density dependence. The molecule fraction grows and saturates to $\sim 30\%$ at densities higher than $5 \times 10^{11} \text{ cm}^{-3}$. The saturation of the molecule fraction resembles observations in a thermal gas [11, 19], where a thermal equilibrium is reached with a constant molecule fraction in the sample [20]. The missing fraction is very small at low densities and continues to grow up to a density of $8 \times 10^{12} \text{ cm}^{-3}$. The stronger density dependence of the missing fraction suggests that scattering processes involved in the atom loss are of higher order than for the molecule increase. Similar enhancement of the collision loss near the Feshbach resonance was also observed in a ^{85}Rb condensate [21] and in a thermal Cs gas [22]. A further analysis on the scattering dynamics and the possible thermal equilibrium condition is necessary.

In conclusion, we show that an atom-molecule conversion fraction of more than 30% can be reached based on a magnetic-field switching scheme. The performance of this scheme is superior to the conventional linear magnetic-field ramping scheme since the molecules are created only within the narrow Feshbach resonance width of 2 mG, while the atoms are lost over a much large range of ~ 40 mG. The density dependence of both the missing fraction and the molecule fraction suggests that in our scheme the molecules are created via Feshbach coupling, while the missing fraction comes from higher-order scattering processes. Based on the new creation scheme, we are now able to obtain samples with up to 40000 ultracold molecules. This provides a good starting point to investigate the trapping, the interactions, and the matter-wave nature of ultracold molecules.

* * *

We acknowledge support by the Austrian Science Fund (FWF) within SFB 15 (project part 16) and by the European Union in the frame of the Cold Molecules TMR Network under Contract No. HPRN-CT-2002-00290. MM is supported by DOC (Doktorandenprogramm der Österreichischen Akademie der Wissenschaften). CC is a Lise-Meitner research fellow of the FWF.

REFERENCES

- [1] DONLEY E. A., CLAUSSEN N. R., THOMPSON S. T. and WIEMAN C., *Nature*, **412** (2002) 295.
- [2] HERBIG J., KRAEMER T., MARK M., WEBER T., CHIN C., NÄGERL H.-C. and GRIMM R., *Science*, **301** (2003) 1510.
- [3] XU K., MUKAIYAMA T., ABO-SHAEER J. R., CHIN J. K., MILLER D. E. and KETTERLE W., *Phys. Rev. Lett.*, **91** (2003) 210402.
- [4] JOCHIM S., BARTENSTEIN M., ALTMAYER A., HENDL G., RIEDL S., CHIN C., HECKER DEN-SCHLAG J. and GRIMM R., *Science*, **302** (2003) 2101; published online November 13, 2003 (10.1126/science.1093280); GREINER M., REGAL C. A. and JIN D. S., *Nature*, **426** (2003) 537; ZWIERLEIN M. W., STAN C. A., SCHUNCK C. H., RAUPACH S. M. F., GUPTA S., HADZIBABIC Z. and KETTERLE W., *Phys. Rev. Lett.*, **91** (2003) 250401.
- [5] TIESINGA E., VERHAAR B. J. and STOOF H. T. C., *Phys. Rev. A*, **47** (1993) 4114; INOUE S., ANDREWS M., STENGER J., MIESNER H.-J., STAMPER-KURN S. and KETTERLE W., *Nature*, **392** (1998) 151.

- [6] DÜRR S., VOLZ T., MARTE A. and REMPE G., *Phys. Rev. Lett.*, **92** (2004) 020406.
- [7] KOKKELMANS S. J. J. M. F., VISSERS H. M. J. and VERHAAR B. J., *Phys. Rev. A*, **63** (2001) 031601(R); VAN ABEELLEN F. A. and VERHAAR B. J., *Phys. Rev. Lett.*, **83** (1999) 1550; TIESINGA E., WILLIAMS C. J., MIES F. H. and JULIENNE P. S., *Phys. Rev. A*, **61** (2000) 063416.
- [8] REGAL C. A., TICKNOR C., BOHN J. L. and JIN D. S., *Nature*, **424** (2003) 47.
- [9] MIES F. H., WILLIAMS C. J., JULIENNE P. S. and KRAUSS M., *J. Res. Natl. Inst. Stand. Technol.*, **101** (1996) 521.
- [10] CHIN C., VULETIĆ V., KERMAN A. J., CHU S., TIESINGA E., LEO P. and WILLIAMS C. J., *Phys. Rev. A*, **70** (2004) 032701.
- [11] CHIN C., VULETIĆ V., KERMAN A. J. and CHU S., *Phys. Rev. Lett.*, **90** (2003) 033201.
- [12] WEBER T., HERBIG J., MARK M., NÄGERL H.-C. and GRIMM R., *Science*, **299** (2003) 232.
- [13] KRAEMER T., HERBIG J., MARK M., WEBER T., CHIN C., NÄGERL H.-C. and GRIMM R., *Appl. Phys. B*, **79** (2004) 1013. For the present experiment, we have improved the atom number in the BEC by another factor two using the higher power from a new Yb fiber laser.
- [14] MUKAIYAMA T., ABO-SHAER J. R., XU K., CHIN J. K. and KETTERLE W., *Phys. Rev. Lett.*, **92** (2004) 180402; DÜRR S., VOLZ T. and REMPE G., *Phys. Rev. A*, **70** (2004) 031601(R).
- [15] The response time of $t_{1/e} = 1.54$ ms for the magnetic field is limited by the eddy currents from the vacuum chamber. Starting from 500 mG above the resonance, we estimate the magnetic field will take $\ln(500 \text{ mG}/2 \text{ mG})t_{1/e} \approx 9$ ms to settle within the resonance width. This result is close to the measured delay time of 12 ms.
- [16] We observe that the expansion rate of the molecules is very close to that of the expanding condensate.
- [17] This value is slightly higher than the value given before because of the reduced scattering length.
- [18] The calculated resonance position is 20.1 G. To reflect the correct resonance position, we shift the numerical data by centering the resonance at our observed value of 19.84 G.
- [19] JOCHIM S., BARTENSTEIN M., ALTMAYER A., HENDL G., CHIN C., HECKER DENSCHLAG J. and GRIMM R., *Phys. Rev. Lett.*, **91** (2003) 240402.
- [20] CHIN C. and GRIMM R., *Phys. Rev. A*, **69** (2004) 033612.
- [21] ROBERTS J. L., CLAUSSEN N. R., CORNISH S. L. and WIEMAN C. E., *Phys. Rev. Lett.*, **85** (2000) 728.
- [22] WEBER T., HERBIG J., MARK M., NÄGERL H.-C. and GRIMM R., *Phys. Rev. Lett.*, **91** (2003) 123201.

B.4 Observation of Feshbach-Like Resonances in Collisions between Ultracold Molecules

C. Chin, T. Kraemer, M. Mark, J. Herbig, P. Waldburger, H.-C. Nägerl, and R. Grimm
Phys. Rev. Lett. **94**, 123201 (2005) . cond-mat/0411258

Observation of Feshbach-Like Resonances in Collisions between Ultracold Molecules

C. Chin,^{1,*} T. Kraemer,¹ M. Mark,¹ J. Herbig,¹ P. Waldburger,¹ H.-C. Nägerl,¹ and R. Grimm^{1,2}

¹*Institut für Experimentalphysik, Universität Innsbruck, Technikerstraße 25, 6020 Innsbruck, Austria*

²*Institut für Quantenoptik und Quanteninformation, Österreichische Akademie der Wissenschaften, 6020 Innsbruck, Austria*

(Received 10 November 2004; published 1 April 2005)

We observe magnetically tuned collision resonances for ultracold Cs₂ molecules stored in a CO₂-laser trap. By magnetically levitating the molecules against gravity, we precisely measure their magnetic moment. We find an avoided level crossing which allows us to transfer the molecules into another state. In the new state, two Feshbach-like collision resonances show up as strong inelastic loss features. We interpret these resonances as being induced by Cs₄ bound states near the molecular scattering continuum. The tunability of the interactions between molecules opens up novel applications such as controlled chemical reactions and synthesis of ultracold complex molecules.

DOI: 10.1103/PhysRevLett.94.123201

PACS numbers: 34.50.-s, 05.30.Jp, 32.80.Pj, 67.40.Hf

The synthesis of ultracold molecules from ultracold atoms has opened up new possibilities for studies on molecular matter waves [1–3], strongly interacting superfluids [4], high-precision molecular spectroscopy [5] and coherent molecular optics [6]. In all these experiments, control of the interatomic interaction by magnetic fields plays an essential role in the association process. When a two-atom bound state is magnetically tuned near the quantum state of two scattering atoms, coupling from the atomic to the molecular state can be resonantly enhanced. This is commonly referred to as a Feshbach resonance [7].

The success in controlling the interaction of ultracold atoms raises the question whether a similar level of control can be achieved for ultracold molecules. Resonant interactions between molecules may lead to synthesis of complex objects beyond atomic dimers. Furthermore, scattering processes for molecules involve many novel reactive channels in comparison to the atomic counterpart, e.g., collision induced dissociation, rearrangement, or displacement chemical reactions. Magnetic tunability of the molecular interactions, similar to that resulting from atomic Feshbach resonances, will lead to exciting perspectives for investigating these chemical processes in regimes where quantum statistics and quantum coherence play an important role.

In this Letter, we report the observation of magnetically tuned collision resonances in an ultracold gas of Cs₂ molecules. The ultracold dimers are created from an atomic Bose-Einstein condensate (BEC) by use of a Feshbach ramp [1] and are trapped in a CO₂-laser trap. We precisely measure the magnetic moment of the molecules and observe an avoided crossing [8] which allows us to transfer the molecules into another state. In the new state, we discover two narrow inelastic collision resonances. The resonance structure suggests that bound states of two cesium molecules, or equivalently Cs₄ states, induce the resonant scattering of molecules. These resonances, which we interpret as Feshbach resonances for ultracold molecules, may open the door to the synthesis of more complex molecules and to the control of their chemical reactions.

The relevant molecular energy structure shown in Fig. 1 is based on calculations done at NIST [9,10]. The dissociation threshold, providing the energy reference $E_b = 0$, is associated with two Cs atoms in the lowest ground state sublevel $|F = 3, m_F = 3\rangle$, where F and m_F are the quantum number of the atomic angular momentum and its projection, respectively. As a result of the strong indirect spin-spin interaction of Cs atoms [11], coupling to molecular states with large orbital angular momentum $l = 4$ [10,12] leads to the complexity of the energy structure shown in Fig. 1. This type of coupling is generally referred to as g -wave Feshbach coupling.

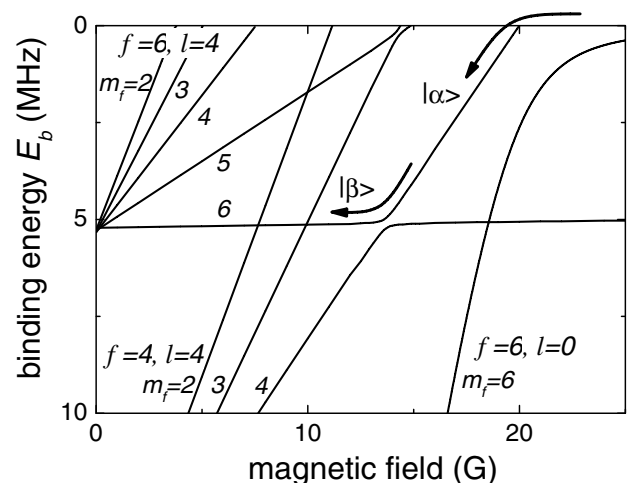


FIG. 1. Molecular energy structure below the scattering continuum of two cesium atoms in the $|F = 3, m_F = 3\rangle$ state. The energy of the dissociation threshold corresponds to $E_b = 0$. The arrows mark the paths to the molecular states we explore, which include the creation of the molecules in $|\alpha\rangle$ via the atomic Feshbach resonance at 19.84 G [1,19] and an avoided crossing to $|\beta\rangle$ at ~ 13.6 G. Included are only molecular states which can couple to the continuum via Feshbach couplings up to g -wave interaction ($l \leq 4$, $m_f + m_l = 6$ and $m_f \geq 2$).

We create the molecules in the bound state $|\alpha\rangle \equiv |f = 4, m_f = 4; l = 4, m_l = 2\rangle$ via g -wave Feshbach coupling at 19.84 G [1]; see Fig. 1. Here, f is the internal angular momentum of the molecule, and m_f and m_l are the projections of f and l , respectively. The molecular state $|\alpha\rangle$ is stable against spontaneous dissociation for magnetic fields below 19.84 G and acquires larger binding energies at lower magnetic fields. This is due to the small magnetic momentum of $\sim 0.95\mu_B$ of this state as compared to the atomic scattering continuum with $\sim 1.5\mu_B$. At about 14 G, an avoided crossing to another state $|\beta\rangle \equiv |f = 6, m_f = 6; l = 4, m_l = 0\rangle$ is induced by the indirect spin-spin coupling. In this work, we ramp the magnetic field adiabatically and explore the upper branch of the avoided crossing.

Our experiment starts with an essentially pure atomic BEC with up to 2.2×10^5 atoms in a crossed dipole trap formed by two CO₂ laser beams [13,14]. We apply a magnetic field of 20 G, slightly above the Feshbach resonance, and a magnetic field gradient of 31 G/cm to levitate the atoms [15]. The CO₂-laser trap is roughly spherically symmetric with a trapping frequency of $\omega \approx 2\pi \times 20$ Hz and a trap depth of 7 μ K. The atomic density is 6×10^{13} cm⁻³ and the chemical potential is $k_B \times 20$ nK, where k_B is Boltzmann's constant.

To create the molecules, we first ramp the magnetic field from 20.0 to 19.5 G in 8 ms and then quickly change the field to 17 G to decouple the molecules from the atoms. Simultaneously, we ramp the magnetic field gradient from 31 up to 50 G/cm. The latter field gradient levitates the molecules [1] and removes all the atoms from the trap in 3 ms. As a consequence, we obtain a pure molecular sample in the CO₂-laser trap with typically 10^4 molecules. The magnetic field ramping process also leads to a small momentum kick on the molecules, which start oscillating in the trap. After ~ 100 ms, the oscillations are damped out and the sample comes to a new equilibrium at a temperature of 250 nK with a peak density of 5×10^{10} cm⁻³ and a phase space density of 10^{-2} to 10^{-3} . To measure the molecule number, we dissociate the molecules into free atoms by reversely ramping the magnetic field back above the resonance to 21 G. We then image the resulting atoms [1].

A key parameter for a perfect levitation of the Cs₂ molecules is the precise value of their magnetic moment [1]. The levitation field is crucial because the gravitational force is much stronger than the trapping force of the CO₂ lasers. In contrast to ground state atoms with only slowly-varying magnetic moment, the magnetic moment of the molecules can sensitively depend on the magnetic field as a result of the complex interactions between molecular states; see Fig. 1. Therefore, the prerequisite to perform Cs₂ molecule experiments at different magnetic fields is the knowledge of the molecular magnetic moment for an accurate setting of the levitation field.

We map out the magnetic moment of the molecules over the range of 11.5 to 19.8 G. This is realized by a two-step

process: First, we slowly tune the magnetic field in 60 ms to a desired value and find a corresponding magnetic field gradient which can approximately keep the molecules near the center of the CO₂-laser trap. Second, after a hold time of 500 ms needed for the ensemble to come to an equilibrium, we measure the position of the cloud. The location of the molecular cloud provides a very sensitive probe to the residual imbalance of the magnetic force and gravity. Given a small vertical displacement of the molecules relative to the trap center δz for a local magnetic field B and a field gradient B' , the magnetic moment is then $\mu(B) = (2m\omega^2\delta z + 2mg)/B'$. Here $2m$ is the molecular mass, and g is the gravitational acceleration. Independent measurements based on releasing the molecules into free space [1] confirm the accuracy of the above method to $0.01\mu_B$.

The measured magnetic moments of the molecules show the expected behavior in the range of 11.5 to 19.8 G; see Fig. 2. We find that the magnetic moment slowly decreases from $0.98\mu_B$ to $0.93\mu_B$ as the magnetic field is lowered from 19.8 G. For magnetic fields below ~ 14 G, the magnetic moment quickly rises and levels off at $1.5\mu_B$. This behavior is readily explained by the avoided crossing at 13.6 G (Figs. 1 and 2), which transfers the molecules from state $|\alpha\rangle$ with $\mu \approx 0.9\mu_B$ to $|\beta\rangle$ with $\mu \approx 1.5\mu_B$. Below 11.5 G, a new avoided crossing to a very weakly coupled $l = 8$ molecular state occurs [16]. We observe fast loss of the molecules since our current apparatus cannot produce a sufficient levitation field to support the molecules against gravity in this new state.

Our measurement agrees excellently with the NIST calculation [9,10] within the 200 mG uncertainty from the multichannel calculation; see Fig. 2. We evaluate the

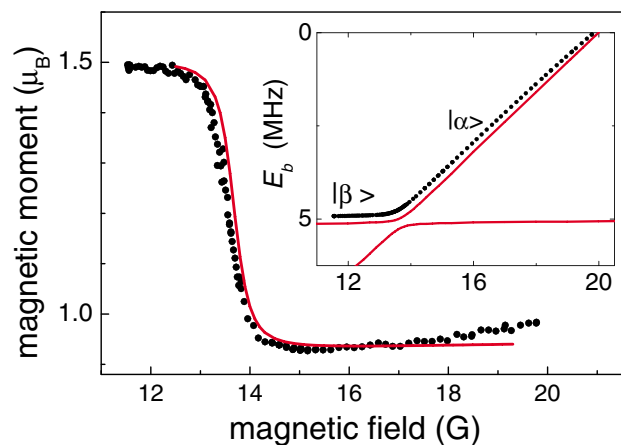


FIG. 2 (color online). Magnetic moment of the Cs₂ molecules. The measured magnetic moment (solid circles) is compared to the NIST calculation (solid line). The fast change at ~ 13.6 G is associated with an avoided crossing. In the inset, we derive the molecular binding energy (solid circles) by integrating the measured magnetic moment. Binding energies from the NIST calculation (solid lines) for both branches of the avoided crossing between state $|\alpha\rangle$ and state $|\beta\rangle$ are shown; see also Fig. 1.

molecular binding energy based on integrating the measured magnetic moments. Here the integration constant is fixed by the fact that the molecular binding energy is zero at the atomic Feshbach resonance $B = 19.84$ G. The result shown in the inset of Fig. 2 gives very good agreement with the theoretical calculation within the energy uncertainty of 0.25 MHz [9]. By fitting our binding energies to a simple avoided crossing model, we determine the crossing to be $B_{\text{cross}} = 13.55(4)$ G and the coupling strength, half the energy splitting between the two eigenstates at B_{cross} , to be $h \times 150(10)$ kHz. Here h is Planck's constant.

To investigate the interactions between molecules, we measure the inelastic collision loss after a trapping time of 300 ms (Fig. 3). For molecules in state $|\alpha\rangle$ ($14 \text{ G} < B < 19.8 \text{ G}$), the fractional loss is about $\sim 40\%$. In this molecular state, we do not see any strong magnetic field dependence. When the magnetic field is tuned near the Feshbach resonance at 19.8 G, molecules dissociate into free atoms, which leave the trap.

In state $|\beta\rangle$ ($11.5 \text{ G} < B < 13.6 \text{ G}$), the behavior of the molecules is strikingly different. We observe a weaker background loss of $\sim 20\%$ and two pronounced resonances with a fractional loss of up to 60%. An expanded view in the inset of Fig. 3 shows that the “double peak” structure can be well fit by a sum of two Lorentzian profiles. From the fit, we determine the resonance positions to be 12.72(1) and 13.15(2) G with full widths of 0.25 and 0.24 G, respectively. Note that due to the levitation gradient field, the inhomogeneity across the molecular sample is as large as 0.15 G in state $|\beta\rangle$, which suggests that the intrinsic widths of these resonances are less than the observed values.

The observed resonances cannot be explained by single-molecule effects based on the Cs_2 energy structure, which is precisely known to very high partial waves [9,10].

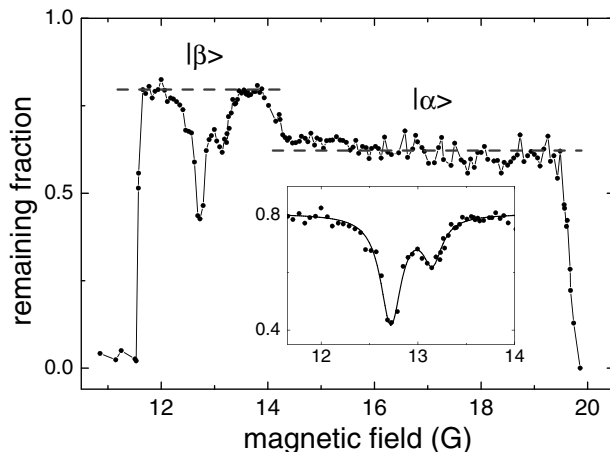


FIG. 3. Remaining fraction of optically trapped molecules after a storage time of 300 ms. Initially, there are 11 000 molecules at a peak density of $6 \times 10^{10} \text{ cm}^{-3}$ and a temperature of 250 nK. The dashed lines mark the background loss rates in state $|\alpha\rangle$ and in state $|\beta\rangle$. The two loss resonances for $|\beta\rangle$ are fit by a sum of two Lorentzian profiles (inset).

Beyond single-molecule effects, the observed resonance structure strongly suggests that bound states of two Cs_2 molecules (Cs_4 tetramer states) are tuned in resonance with the scattering state of the molecules and induce Feshbach-like couplings to inelastic decay channels. Other possible scattering processes, e.g., direct coupling to a trimer and an atom or a dimer and two atoms, should result in a threshold behavior in the loss spectrum instead of the observed resonance structure. For Cs_2 molecules, the appearance of Cs_4 bound states near the scattering continuum is not surprising considering the complexity of interaction between Cs atoms and the additional rotational and vibrational degrees of freedom.

To confirm that the loss is indeed due to collisions between molecules, we observe the decay of the molecular population in the CO_2 -laser trap. Starting with 11 000 molecules prepared at different magnetic fields, we record the molecule number after various wait times, as shown in Fig. 4. Three magnetic field values are chosen here: 15.4 G where the molecules are in state $|\alpha\rangle$, 12.1 G where the molecules are in state $|\beta\rangle$ and are away from the resonance, and 12.7 G where the molecules are on the strong molecular resonance; see Fig. 4. The number of trapped molecules shows a nonexponential decay, which provides a clear signature of the density-dependent processes.

To further investigate the underlying molecular collision processes, we model the loss based on a two-body or a three-body loss equation. Assuming a Gaussian distribution for the thermal ensemble in a harmonic trap with a constant temperature and that the collision loss rate is slow compared to the thermalization rate, we fit the measured molecule numbers to the two-body and three-body decay equation; see in Fig. 4. For 15.4 and 12.1 G, we find that the two-body equation provides excellent fits. The two-body

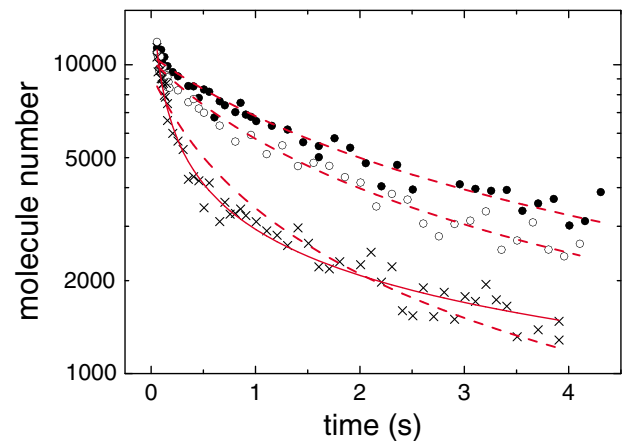


FIG. 4 (color online). Time evolution of the molecule number in the CO_2 -laser trap for molecules in state $|\alpha\rangle$ at 15.4 G (open circles), in state $|\beta\rangle$ at 12.1 G (off resonance, solid circles) and at 12.7 G (on resonance, crosses). Fits based on two-body loss (dashed lines) work well for 15.4 and 12.1 G. A fit based on three-body loss (solid line) works better for 12.7 G.

coefficients are 5×10^{-11} cm³/s at 15.4 G and 3×10^{-11} cm³/s at 12.1 G. We cannot, however, rule out the possibility that three-body processes also play a role. The measured collision rate coefficients are similar to the measurements from the MIT group on Na₂ [17], and are an order of magnitude below the unitarity limit of $2h/mk = 4 \times 10^{-10}$ cm³/s, where k is the characteristic collision wave number associated with the temperature of the sample.

At 12.7 G, where the molecules are on the strong resonance, we find that the three-body equation actually provides a better fit than the two-body fit with a three-body loss coefficient at 6×10^{-20} cm⁶/s; see Fig. 4. This value, however, is much too high compared to the three-body unitarity limit of $96\pi h/mk^4 = 2 \times 10^{-23}$ cm⁶/s [18]. One alternative explanation is that on resonance, the fast collision loss rate might leave the molecules insufficient time to reach thermal equilibrium. By fitting the resonance data in the first 200 ms with the two-body loss model, we determine the two-body loss coefficient to be 2×10^{-10} cm³/s, which indeed approaches the unitarity limit of 4×10^{-10} cm³/s.

In conclusion, we have observed magnetically tuned collision resonances in a trapped ultracold sample of Cs₂ dimers. The density-dependent inelastic decay and the resonance structure strongly suggest a resonant coupling to Cs₄ tetramer states. Our observations are reminiscent of Feshbach resonances in atom-atom scattering. The controlled use of such resonances for interaction tuning and molecule formation in atomic ensembles has opened up new avenues in research on ultracold quantum gases. Our observation of magnetically tuned Feshbach-like resonances in molecule-molecule scattering brings in fascinating prospects for a controlled synthesis of ultracold tetramers in a single four-body quantum state in analogy to the formation of ultracold dimers near atomic Feshbach resonances. The tunability of the interactions in molecular quantum gases can potentially open up the door to few-body physics beyond simple atoms and diatomic molecules and to a new ultracold chemistry.

We greatly thank E. Tiesinga and P.S. Julienne for stimulating discussions, and, in particular, for providing us with the theoretical calculation on the Cs₂ energy structure. We acknowledge support by the Austrian Science Fund (FWF) within SFB 15 and the Lise Meitner program, and by the European Union in the frame of the Cold Molecules TMR Network under Contract No. HPRN-CT-2002-00290. M.M. is supported by DOC [Doktorandenprogramm der Österreichischen Akademie der Wissenschaften].

*Present address: Department of Physics and James Franck Institute, University of Chicago, Chicago, IL 60637, USA.

[1] J. Herbig, T. Kraemer, M. Mark, T. Weber, C. Chin, H.-C. Nägerl, and R. Grimm, *Science* **301**, 1510 (2003).

- [2] K. Xu, T. Mukaiyama, J.R. Abo-Shaer, J.K. Chin, D.E. Miller, and W. Ketterle, *Phys. Rev. Lett.* **91**, 210402 (2003).
- [3] S. Jochim, M. Bartenstein, A. Altmeyer, G. Hendl, S. Riedl, C. Chin, J. Hecker Denschlag, and R. Grimm, *Science* **302**, 2101 (2003); M. Greiner, C.A. Regal, and D.S. Jin, *Nature (London)* **426**, 537 (2003); M.W. Zwierlein, C.A. Stan, C.H. Schunck, S.M.F. Raupach, S. Gupta, Z. Hadzibabic, and W. Ketterle, *Phys. Rev. Lett.* **91**, 250401 (2003).
- [4] M. Bartenstein, A. Altmeyer, S. Riedl, S. Jochim, C. Chin, J. Hecker Denschlag, and R. Grimm, *Phys. Rev. Lett.* **92**, 120401 (2004); C.A. Regal, M. Greiner, and D.S. Jin, *Phys. Rev. Lett.* **92**, 040403 (2004); M.W. Zwierlein, C.A. Stan, C.H. Schunck, S.M.F. Raupach, A.J. Kerman, and W. Ketterle, *Phys. Rev. Lett.* **92**, 120403 (2004); T. Bourdel, L. Khaykovich, J. Cubizolles, J. Zhang, F. Chevy, M. Teichmann, L. Tarruell, S.J.J.M.F. Kokkelmans, and C. Salomon, *Phys. Rev. Lett.* **93**, 050401 (2004).
- [5] M. Bartenstein, A. Altmeyer, S. Riedl, R. Geursen, S. Jochim, C. Chin, J. Hecker Denschlag, R. Grimm, A. Simoni, E. Tiesinga, C.J. Williams, and P.S. Julienne, *Phys. Rev. Lett.* **94**, 103201 (2005); *cond-mat/0408673*.
- [6] J.R. Abo-Shaer, D.E. Miller, J.K. Chin, K. Xu, T. Mukaiyama, and W. Ketterle, *Phys. Rev. Lett.* **94**, 040405 (2005).
- [7] E. Tiesinga, B.J. Verhaar, and H.T.C. Stoof, *Phys. Rev. A* **47**, 4114 (1993); S. Inouye, M. Andrews, J. Stenger, H.-J. Miesner, S. Stamper-Kurn, and W. Ketterle, *Nature (London)* **392**, 151 (1998).
- [8] S. Dürr, T. Volz, A. Marte, and G. Rempe, *Phys. Rev. Lett.* **92**, 020406 (2004).
- [9] E. Tiesinga and P.S. Julienne (private communication).
- [10] C. Chin, V. Vuletić, A.J. Kerman, S. Chu, E. Tiesinga, P.J. Leo, and C.J. Williams, *Phys. Rev. A* **70**, 032701 (2004).
- [11] F.H. Mies, C.J. Williams, P.S. Julienne, and M. Krauss, *J. Res. Natl. Inst. Stand. Technol.* **101**, 521 (1996).
- [12] C. Chin, A.J. Kerman, V. Vuletić, and S. Chu, *Phys. Rev. Lett.* **90**, 033201 (2003).
- [13] T. Kraemer, J. Herbig, M. Mark, T. Weber, C. Chin, H.-C. Nägerl, R. Grimm, *Appl. Phys. B* **79**, 1013 (2004).
- [14] We adiabatically transfer the atomic BEC from a near-infrared laser trap, where the atomic BEC is formed [13], to the CO₂-laser trap by simultaneously reducing the near-infrared laser power to zero and ramping the CO₂ lasers to full power in 1 s.
- [15] T. Weber, J. Herbig, M. Mark, H.-C. Nägerl, and R. Grimm, *Science* **299**, 232 (2003).
- [16] This $l = 8$ state, not shown in Fig. 1, is very weakly coupled to the state $|\beta\rangle$. Investigations on this state are currently in progress.
- [17] T. Mukaiyama, J.R. Abo-Shaer, K. Xu, J.K. Chin, and W. Ketterle, *Phys. Rev. Lett.* **92**, 180402 (2004).
- [18] H. Suno, B.D. Esry, and C.H. Greene, *Phys. Rev. Lett.* **90**, 053202 (2003).
- [19] M. Mark, T. Kraemer, J. Herbig, C. Chin, H.-C. Nägerl, and R. Grimm, *Europhys. Lett.* **69**, 706 (2005); *cond-mat/0409737*.

B.5 Evidence for Efimov quantum states in an ultracold gas of caesium atoms

T. Kraemer, M. Mark, P. Waldburger, J. G. Danzl, C. Chin, B. Engeser, A. D. Lange, K. Pilch, A. Jaakkola, H.-C. Nägerl and R. Grimm
Nature **440**, 315-318 (16 March 2006), cond-mat/0512394

Evidence for Efimov quantum states in an ultracold gas of caesium atoms

T. Kraemer¹, M. Mark¹, P. Waldburger¹, J. G. Danzl¹, C. Chin^{1,2}, B. Engeser¹, A. D. Lange¹, K. Pilch¹, A. Jaakkola¹, H.-C. Nägerl¹ & R. Grimm^{1,3}

Systems of three interacting particles are notorious for their complex physical behaviour. A landmark theoretical result in few-body quantum physics is Efimov's prediction^{1,2} of a universal set of bound trimer states appearing for three identical bosons with a resonant two-body interaction. Counterintuitively, these states even exist in the absence of a corresponding two-body bound state. Since the formulation of Efimov's problem in the context of nuclear physics 35 years ago, it has attracted great interest in many areas of physics^{3–8}. However, the observation of Efimov quantum states has remained an elusive goal^{3,5}. Here we report the observation of an Efimov resonance in an ultracold gas of caesium atoms. The resonance occurs in the range of large negative two-body scattering lengths, arising from the coupling of three free atoms to an Efimov trimer. Experimentally, we observe its signature as a giant three-body recombination loss^{9,10} when the strength of the two-body interaction is varied. We also detect a minimum^{9,11,12} in the recombination loss for positive scattering lengths, indicating destructive interference of decay pathways. Our results confirm central theoretical predictions of Efimov physics and represent a starting point with which to explore the universal properties of resonantly interacting few-body systems⁷. While Feshbach resonances^{13,14} have provided the key to control quantum-mechanical interactions on the two-body level, Efimov resonances connect ultracold matter¹⁵ to the world of few-body quantum phenomena.

Efimov's treatment of three identical bosons^{1,2} is closely linked to the concept of universality⁷ in systems with a resonant two-body interaction, where the *s*-wave scattering length *a* fully characterizes the two-body physics. When $|a|$ greatly exceeds the characteristic range ℓ of the two-body interaction potential, details of the short-range interaction become irrelevant because of the long-range nature of the wavefunction. Universality then leads to a generic behaviour in three-body physics, reflected in the energy spectrum of weakly bound Efimov trimer states. Up to now, in spite of their great fundamental importance, these states could not be observed experimentally. An observation in the realm of nuclear physics, as originally proposed by Efimov, is hampered by the presence of the Coulomb interaction, and only two-neutron halo systems with a spinless core are likely to feature Efimov states³. In molecular physics, the helium trimer is predicted to have an excited state with Efimov character⁴. The existence of this state could not be confirmed⁵. A different approach to experimentally studying the physics of Efimov states is based on the unique properties of ultracold atomic quantum gases. Such systems¹⁵ provide an unprecedented level of control, enabling the investigation of interacting quantum systems. The ultralow collision energies allow us to explore the zero-energy quantum limit. Moreover, two-body interactions can be precisely tuned on the basis of Feshbach resonances^{13,14}.

Efimov's scenario^{1,2,7} can be illustrated by the energy spectrum of the three-body system as a function of the inverse scattering length $1/a$ (Fig. 1). Let us first consider the well-known weakly bound dimer state, which only exists for large positive *a*. In the resonance regime, its binding energy is given by the universal expression $E_b = -\hbar^2/(ma^2)$, where *m* is the atomic mass and \hbar is Planck's constant divided by 2π . In Fig. 1, where the resonance limit corresponds to $1/a \rightarrow 0$, the dimer energy E_b is represented by a parabola for $a > 0$. If we now add one more atom with zero energy, a natural continuum threshold for the bound three-body system (hatched line in Fig. 1) is given by the three-atom threshold ($E = 0$) for negative *a* and by the dimer-atom threshold (E_b) for positive *a*. Energy states below the continuum threshold are necessarily three-body bound states. When $1/a$ approaches the resonance from the negative-*a* side, a first Efimov trimer state appears in a range where a weakly bound two-body state does not exist. When passing through the resonance the state connects to the positive-*a* side, where it finally intersects with the dimer-atom threshold. An infinite series of such Efimov states is found when scattering lengths are increased and binding energies are decreased in powers of universal scaling

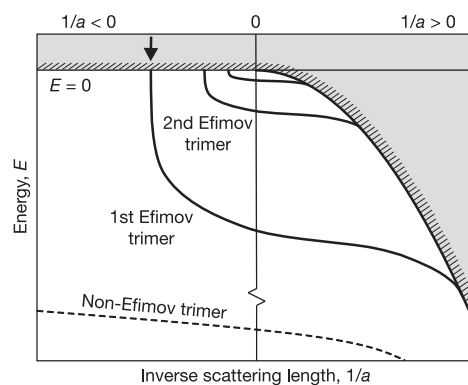


Figure 1 | Efimov's scenario. Appearance of an infinite series of weakly bound Efimov trimer states for resonant two-body interaction. The binding energy is plotted as a function of the inverse two-body scattering length $1/a$. The shaded region indicates the scattering continuum for three atoms ($a < 0$) and for an atom and a dimer ($a > 0$). The arrow marks the intersection of the first Efimov trimer with the three-atom threshold. To illustrate the series of Efimov states, we have artificially reduced the universal scaling factor from 22.7 to 2. For comparison, the dashed line indicates a tightly bound non-Efimov trimer³⁰, which does not interact with the scattering continuum.

¹Institut für Experimentalphysik, Universität Innsbruck, Technikerstraße 25, A-6020 Innsbruck, Austria. ²James Franck Institute, Physics Department of the University of Chicago, 5640 S. Ellis Avenue Chicago, Illinois 60637, USA. ³Institut für Quantenoptik und Quanteninformation der Österreichischen Akademie der Wissenschaften, Otto-Hittmair-Platz 1, A-6020 Innsbruck, Austria.

factors^{1,2,7} $e^{\pi/s_0} \approx 22.7$ and $e^{-2\pi/s_0} \approx 1/515$ (where $s_0 = 1.00624$), respectively.

Resonant scattering phenomena arise as a natural consequence of Efimov's scenario¹⁶. When an Efimov state intersects with the continuum threshold at negative scattering lengths a , three free atoms in the ultracold limit resonantly couple to a trimer. This results in a triatomic Efimov resonance. At finite collision energies, the phenomenon evolves into a triatomic continuum resonance¹⁷. Another type of Efimov resonance¹⁸ is found at positive values of a for collisions between a free atom and a dimer, when Efimov states intersect with the dimer-atom threshold. While the latter type of Efimov resonance corresponds to Feshbach resonances in collisions between atoms and dimers¹⁸, triatomic Efimov resonances can be interpreted as a three-body generalization to Feshbach resonances⁸.

Striking manifestations of Efimov physics have been predicted for three-body recombination processes in ultracold gases with tunable two-body interactions^{7,9-12,19}. Three-body recombination leads to losses from a trapped gas with a rate proportional to the third power of the atomic number density. These losses are commonly described²⁰ in terms of a loss rate coefficient L_3 . In the resonant case ($|a| \gg \ell$), it is convenient to express this coefficient in the form $L_3 = 3C(a)\hbar a^4/m$, separating a general a^4 -scaling^{20,21} from an additional dependence^{9,10,12} $C(a)$. Efimov physics is reflected in a logarithmically periodic behaviour $C(22.7a) = C(a)$, corresponding to the scaling of the infinite series of weakly bound trimer states. For negative scattering lengths, the resonant coupling of three atoms to an Efimov state opens up fast decay channels into deeply bound dimer states plus a free atom.

Triatomic Efimov resonances thus show up in giant recombination loss. This striking phenomenon was first identified in numerical solutions to the adiabatic hyperspherical approximation of the three-body Schrödinger equation, assuming simple model potentials and interpreted in terms of tunnelling through a potential barrier in the three-body entrance channel⁹. A different theoretical approach^{7,10}, based on effective field theory, provides the analytic expression $C(a) = 4,590 \sinh(2\eta_-) / (\sin^2[s_0 \ln(|a|/a_-)] + \sinh^2\eta_-)$. The free parameter a_- for the resonance positions at $a_-, 22.7a_-, \dots$ depends on the short-range part of the effective three-body interaction and is thus not determined in the frame of the universal long-range theory. As a second free parameter, the dimensionless quantity η_- describes the unknown decay rate of Efimov states into deeply bound dimer states plus a free atom, and thus characterizes the resonance width.

Our measurements are based on the magnetically tunable interaction properties of caesium atoms²² in the lowest internal state. By applying fields between 0 and 150 G, we varied the s -wave scattering length a in a range between $-2,500a_0$ to $1,600a_0$, where a_0 is Bohr's radius. Accurate three-body loss measurements are facilitated by the fact that inelastic two-body loss is energetically forbidden²⁰. The characteristic range of the two-body potential is given by the van der Waals length²³, which for caesium is $\ell \approx 100a_0$. This leaves us with enough room to study the universal regime requiring $|a| \gg \ell$. For negative a , a maximum value of 25 is attainable for $|a|/\ell$. Efimov's estimate $\frac{1}{\pi} \ln(|a|/\ell)$ for the number of weakly bound trimer states² suggests the presence of one Efimov resonance in the accessible range of negative scattering lengths.

Our experimental results (Fig. 2), obtained with optically trapped thermal samples of caesium atoms in two different set-ups (see Methods), indeed show a giant loss feature marking the expected resonance. We present our data in terms of a recombination length⁹ $\rho_3 = [2m/(\sqrt{3}\hbar)L_3]^{1/4}$, which leads to the simple relation $\rho_3/a = 1.36C^{1/4}$. Note that the general a^4 -scaling corresponds to a linear behaviour in $\rho_3(a)$ (straight lines in Fig. 2). A fit of the analytic theory^{7,10} to our experimental data taken for negative a at temperatures $T \approx 10$ nK shows a remarkable agreement and determines the resonance position to $a_- = -850(20)a_0$ and the decay parameter to $\eta_- = 0.06(1)$. The pronounced resonance behaviour with a small value for the decay parameter ($\eta_- \ll 1$) demonstrates a sufficiently

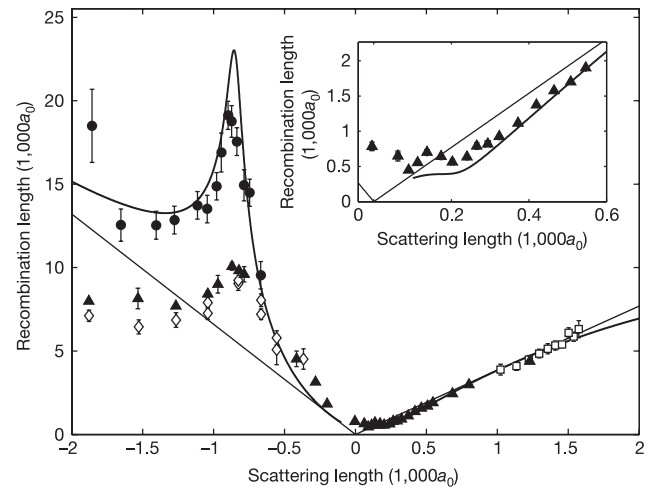


Figure 2 | Observation of the Efimov resonance in measurements of three-body recombination. The recombination length $\rho_3 \propto L_3^{1/4}$ is plotted as a function of the scattering length a . The dots and the filled triangles show the experimental data from set-up A for initial temperatures around 10 nK and 200 nK, respectively. The open diamonds are from set-up B at temperatures of 250 nK. The open squares are previous data²⁰ at initial temperatures between 250 and 450 nK. The solid curve represents the analytic model from effective field theory⁷ with $a_- = -850a_0$, $a_+ = 1,060a_0$, and $\eta_- = \eta_+ = 0.06$. The straight lines result from setting the \sin^2 and \cos^2 -terms in the analytic theory to 1, which gives a lower recombination limit for $a < 0$ and an upper limit for $a > 0$. The inset shows an expanded view for small positive scattering lengths with a minimum for $C(a) \propto (\rho_3/a)^4$ near $210a_0$. The displayed error bars refer to statistical uncertainties only. Uncertainties in the determination of the atomic number densities may lead to additional calibration errors for ρ_3 of up to 20%.

long lifetime of Efimov trimers to allow their observation as distinct quantum states.

All the results discussed so far are valid in the zero-energy collision limit of sufficiently low temperatures. For ultracold but non-zero temperatures the recombination length is unitarity limited¹⁹ to $5.2\hbar/(mk_B T)^{-1/2}$. For $T = 10$ nK this limit corresponds to about $60,000a_0$ and our sample is thus cold enough to justify the zero-temperature limit. For 250 nK, however, unitarity limits the recombination length to about $12,000a_0$. The Efimov resonance is still visible at temperatures of 200 and 250 nK (filled triangles and open diamonds in Fig. 2). The slight shift to lower values of $|a|$ suggests the evolution of the zero-energy Efimov resonance into a triatomic continuum resonance¹⁷. In further experiments at higher temperatures (data not shown) we observed the resonance to disappear above ~ 500 nK.

For positive scattering lengths, we found three-body losses to be typically much weaker than for negative values. Our measurements are consistent with a maximum recombination loss of $C(a) \approx 70$, or equivalently $\rho_3 \approx 3.9a$, as predicted by different theories^{9,11,12} (straight line for $a > 0$ in Fig. 2). For a below $600a_0$ the measured recombination length significantly drops below this upper limit (inset in Fig. 2). The analytic expression from effective field theory^{7,12} for $a > 0$ reads $C(a) = 67.1e^{-2\eta_+} (\cos^2[s_0 \ln(a/a_+)] + \sinh^2\eta_+) + 16.8(1 - e^{-4\eta_+})$ with the two free parameters a_+ and η_+ . The first term describes recombination into the weakly bound dimer state with an oscillatory behaviour that is due to an interference effect between two different pathways^{9,11}. The second term results from decay into deeply bound states. We use this expression to fit our data points with $a > 5\ell \approx 500a_0$. This somewhat arbitrary condition is introduced as a reasonable choice to satisfy $a \gg \ell$ for the validity of the universal theory. The fit is quite insensitive to the value of the decay parameter and yields $\eta_+ < 0.2$. This result is consistent with the theoretical assumption¹⁰ of the same value for the decay

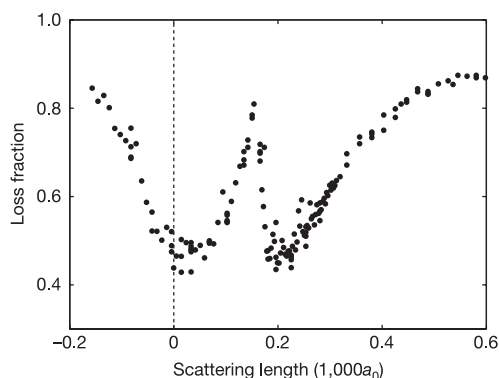


Figure 3 | Atom loss for small scattering lengths. Besides a minimum near zero scattering length, we identify a minimum of recombination loss at $\sim 210a_0$, which can be attributed to a predicted destructive interference effect^{9,11,12}.

parameter for positive and negative a , which in our case is $\eta_+ = \eta_- = 0.06$. For maximum $C(a)$, we obtain $a_+ = 1,060(70)a_0$. According to theory⁷, the trimer state hits the dimer–atom threshold at $a = 1.1a_+ \approx 1,170a_0$. The logarithmic periodicity of the Efimov scenario suggests that adjacent loss minima occur at $\sqrt{22.7} \times 1,060a_0 \approx 5,000a_0$ and at $1,060a_0/\sqrt{22.7} \approx 220a_0$. While the former value is out of our accessible range, the latter value ($a \approx 2\ell$) is too small to strictly justify universal behaviour in the resonance limit ($a \gg \ell$). Nevertheless, our experimental results (inset to Fig. 2) indicate a minimum at $a \approx 210a_0$ and the analytic expression for $C(a)$ is found to describe our data quite well down to this minimum.

The occurrence of the interference minimum in three-body loss is demonstrated more clearly in another set of experiments (Fig. 3), where we simply measured the loss of atoms after a fixed storage time in the optical trap. This minimum is located at $a = 210(10)a_0$ in addition to a second minimum close to zero scattering length. We point out that the existence of the minimum at $210a_0$ is very advantageous for efficient evaporative cooling of caesium as it combines a large scattering cross-section with very low loss. Inadvertently, we have already benefited from this loss minimum for the optimized production of a Bose–Einstein condensate of caesium²⁴.

The comparison of our experimental results to available three-body theory shows remarkable agreement, although the collision physics of caesium is in general a very complicated multi-channel scattering problem. We believe that the particular nature of the broad, ‘‘open-channel dominated’’ Feshbach resonance²⁵ that underlies the tunability of our system plays a crucial role. For such a resonance, the two-body scattering problem can be described in terms of an effective single-channel model. It is very interesting to investigate to what degree this great simplification of the two-body physics extends to the three-body problem. Here we particularly wonder how the regions of positive and negative scattering lengths are connected in our experiment, where a is changed through a zero crossing—that is, through a non-universal region, and not across the universal resonance region.

In our case, there is no obvious connection between the Efimov state that leads to the observed resonance for $a < 0$ and the states responsible for the behaviour for $a > 0$. In our analysis of the experimental data, we have thus independently fitted the data sets for negative and positive a . Nevertheless, the resulting values for the two independent fit parameters a_- and a_+ do suggest a connection: for the ratio $a_+/|a_-|$ our experiment yields 1.25(9), whereas universal theory⁷ predicts 0.96(3). These numbers are quite close in view of the Efimov factor of 22.7. If it is not an accidental coincidence, we speculate that the apparent relation between a_+ and a_- may be a further consequence of universality in a system where the resonant two-body interaction can be modelled in terms of a single scattering

channel. In general, the multi-channel nature of three-body collisions near Feshbach resonances^{26,27} leads to further interesting questions, such as whether there may be resonance effects beyond the Efimov scenario. Advances in three-body theory are necessary to answer these questions and to provide a complete interpretation of our present observations.

In the past few years, applications of Feshbach resonances in ultracold gases and the resulting ability to create dimer states have set the stage for many new developments in matter-wave quantum physics. The observation of an Efimov resonance now confirms the existence of weakly bound trimer states and opens up new ways^{6,8} of experimentally exploring the intriguing physics of few-body quantum systems.

METHODS

Magnetic tuning of the two-body interaction. For Cs atoms in their energetically lowest state (quantum numbers $F = 3$ for the total spin and $m_F = 3$ for its projection) the s -wave scattering length a varies strongly with the magnetic field²². Between 0 and 150 G the dependence can in general be well approximated by the fitting formula:

$$a(B)/a_0 = (1,722 + 1.52B/G) \left(1 - \frac{28.72}{B/G + 11.74} \right)$$

except for a few narrow Feshbach resonances²². The smooth variation of the scattering length in the low-field region results from a broad Feshbach resonance centred at about -12 G (equivalent to $+12$ G in the state $F = 3, m_F = -3$). In all our measurements we excluded the magnetic field regions where the narrow Feshbach resonances influence the scattering behaviour through coupling to other molecular potentials. The Efimov resonance is centred at 7.5 G.

Trap set-ups and preparation of the Cs gases. All measurements were performed with trapped thermal samples of caesium atoms at temperatures T ranging from 10 to 250 nK. We used two different experimental set-ups, which have been described elsewhere^{24,28}.

In set-up A we first produced an essentially pure Bose–Einstein condensate with up to 250,000 atoms in a far-detuned crossed optical dipole trap generated by two 1,060-nm Yb-doped fibre laser beams²⁴. We then ramped the magnetic field to 16.2 G, where the scattering length is negative with a value of $-50a_0$, thus inducing a collapse of the condensate²⁹. After an equilibration time of 1 s we were left with a thermal sample at typically $T = 10$ nK containing up to 20,000 atoms at peak densities ranging from $n_0 = 3 \times 10^{11} \text{ cm}^{-3}$ to $3 \times 10^{12} \text{ cm}^{-3}$. Alternatively, we interrupted the evaporation process before condensation to produce thermal samples at $T \approx 200$ nK in a crossed dipole trap generated by one of the 1,060-nm beams and a 10.6- μm CO₂ laser beam. After recompression of the trap this produced typical densities of $n_0 = 5 \times 10^{13} \text{ cm}^{-3}$. The measurements in the region of the loss minima as displayed in Fig. 3 were taken after a storage time of 200 ms at initial densities of $n_0 = 6 \times 10^{13} \text{ cm}^{-3}$.

In set-up B we used an optical surface trap²⁸ in which we prepared a thermal sample of 10,000 atoms at $T \approx 250$ nK via forced evaporation at a density of $n_0 = 1.0 \times 10^{12} \text{ cm}^{-3}$. The dipole trap was formed by a repulsive evanescent laser wave on top of a horizontal glass prism in combination with a single horizontally confining 1,060-nm laser beam propagating along the vertical direction.

Determination of three-body loss rate coefficients. We measured three-body loss rates in set-up A by recording the time evolution of the atom number N and the temperature T . A detailed description of this procedure has been given in ref. 20. In brief, the process of three-body recombination not only leads to a loss of atoms, but also induces ‘anti-evaporation’ and recombination heating. The first effect is present at any value of the scattering length a . The second effect occurs for positive values of a when the recombination products remain trapped. Atom loss and temperature rise are modelled by a set of two coupled nonlinear differential equations. We used numerical solutions to this set of equations to fit our experimental data. From these fits, together with measurements of the trapping parameters, we obtained the rate coefficient L_3 . In set-up B we recorded the loss at decay times sufficiently short to make sure that heating is negligible.

Received 12 December 2005; accepted 2 February 2006.

1. Efimov, V. Energy levels arising from resonant two-body forces in a three-body system. *Phys. Lett. B.* **33**, 563–564 (1970).
2. Efimov, V. Weakly-bound states of three resonantly-interacting particles. *Sov. J. Nucl. Phys.* **12**, 589–595 (1971).
3. Jensen, A. S., Riisager, K., Fedorov, D. V. & Garrido, E. Structure and reactions of quantum halos. *Rev. Mod. Phys.* **76**, 215–261 (2004).

4. Lim, T. K., Duffy, K. & Damer, W. C. Efimov state in the ^4He trimer. *Phys. Rev. Lett.* **38**, 341–343 (1977).
5. Brühl, R. *et al.* Matter wave diffraction from an inclined transmission grating: Searching for the elusive ^4He trimer Efimov state. *Phys. Rev. Lett.* **95**, 063002 (2005).
6. Braaten, E., Hammer, H.-W. & Kusunoki, M. Efimov states in a Bose-Einstein condensate near a Feshbach resonance. *Phys. Rev. Lett.* **90**, 170402 (2003).
7. Braaten, E. & Hammer, H.-W. Universality in few-body systems with large scattering length. Preprint at (<http://arXiv.org/abs/cond-mat/0410417>) (2004).
8. Stoll, M. & Köhler, T. Production of three-body Efimov molecules in an optical lattice. *Phys. Rev. A* **72**, 022714 (2005).
9. Esry, B. D., Greene, C. H. & Burke, J. P. Jr Recombination of three atoms in the ultracold limit. *Phys. Rev. Lett.* **83**, 1751–1754 (1999).
10. Braaten, E. & Hammer, H.-W. Three-body recombination into deep bound states in a Bose gas with large scattering length. *Phys. Rev. Lett.* **87**, 160407 (2001).
11. Nielsen, E. & Macek, J. H. Low-energy recombination of identical bosons by three-body collisions. *Phys. Rev. Lett.* **83**, 1566–1569 (1999).
12. Bedaque, P. F., Braaten, E. & Hammer, H.-W. Three-body recombination in Bose gases with large scattering length. *Phys. Rev. Lett.* **85**, 908–911 (2000).
13. Tiesinga, E., Verhaar, B. J. & Stoof, H. T. C. Threshold and resonance phenomena in ultracold ground-state collisions. *Phys. Rev. A* **47**, 4114–4122 (1993).
14. Inouye, S. *et al.* Observation of Feshbach resonances in a Bose-Einstein condensate. *Nature* **392**, 151–154 (1998).
15. Southwell, K. (ed.) *Ultracold matter Nature (Insight)* **416**, 205–246 (2002).
16. Efimov, V. Low-energy properties of three resonantly interacting particles. *Sov. J. Nucl. Phys.* **29**, 546–553 (1979).
17. Bringas, F., Yamashita, M. T. & Frederico, T. Triatomic continuum resonances for large negative scattering lengths. *Phys. Rev. A* **69**, 040702(R) (2004).
18. Nielsen, E., Suno, H. & Esry, B. D. Efimov resonances in atom-diatom scattering. *Phys. Rev. A* **66**, 012705 (2002).
19. D’Incao, J. P., Suno, H. & Esry, B. D. Limits on universality in ultracold three-boson recombination. *Phys. Rev. Lett.* **93**, 123201 (2004).
20. Weber, T., Herbig, J., Mark, M., Nägerl, H.-C. & Grimm, R. Three-body recombination at large scattering lengths in an ultracold atomic gas. *Phys. Rev. Lett.* **91**, 123201 (2003).
21. Fedichev, P. O., Reynolds, M. W. & Shlyapnikov, G. V. Three-body recombination of ultracold atoms to a weakly bound s level. *Phys. Rev. Lett.* **77**, 2921–2924 (1996).
22. Chin, C. *et al.* Precision Feshbach spectroscopy of ultracold Cs_2 . *Phys. Rev. A* **70**, 032701 (2004).
23. Bolda, E. L., Tiesinga, E. & Julienne, P. S. Effective-scattering-length model of ultracold atomic collisions and Feshbach resonances in tight harmonic traps. *Phys. Rev. A* **66**, 013403 (2002).
24. Kraemer, T. *et al.* Optimized production of a cesium Bose-Einstein condensate. *Appl. Phys. B* **79**, 1013–1019 (2004).
25. Köhler, T., Goral, K. & Julienne, P. S. Production of cold molecules via magnetically tunable Feshbach resonances. Preprint at (<http://arxiv.org/abs/cond-mat/0601420>) (2006).
26. Kartavtsev, O. I. & Macek, J. H. Low-energy three-body recombination near a Feshbach resonance. *Few-Body Syst.* **31**, 249–254 (2002).
27. Petrov, D. S. Three-boson problem near a narrow Feshbach resonance. *Phys. Rev. Lett.* **93**, 143201 (2004).
28. Rychtarik, D., Engeser, B., Nägerl, H.-C. & Grimm, R. Two-dimensional Bose-Einstein condensate in an optical surface trap. *Phys. Rev. Lett.* **92**, 173003 (2004).
29. Donley, E. A. *et al.* Dynamics of collapsing and exploding Bose-Einstein condensates. *Nature* **412**, 295–299 (2001).
30. Thomas, L. H. The interaction between a neutron and a proton and the structure of H^3 . *Phys. Rev.* **47**, 903–909 (1935).

Acknowledgements We thank E. Braaten, C. Greene, B. Esry, H. Hammer and T. Köhler for many discussions and E. Kneringer for support regarding the data analysis. We acknowledge support by the Austrian Science Fund (FWF) within Spezialforschungsbereich 15 and within the Lise Meitner programme, and by the European Union in the frame of the TMR networks ‘Cold Molecules’ and ‘FASTNet’. M.M. is supported within the Doktorandenprogramm of the Austrian Academy of Sciences.

Author Information Reprints and permissions information is available at npg.nature.com/reprintsandpermissions. The authors declare no competing financial interests. Correspondence and requests for materials should be addressed to H.-C.N. (christoph.naegerl@ultracold.at).

References

- [Ama73] R. D. Amado and F. C. Greenwood, *There is no Efimov effect for four or more particles*, Phys. Rev. D **7**, 2517 (1973).
- [And95] M. H. Anderson, J. R. Ensher, M. R. Matthews, and C. E. W. and E. A. Cornell, *Observation of Bose-Einstein Condensation in a Dilute Atomic Vapor*, Science **269**, 198 (1995).
- [AS05] J. R. Abo-Shaeer, D. E. Miller, J. K. Chin, K. Xu, T. Mukaiyama, and W. Ketterle, *Coherent molecular optics using ultracold sodium dimers*, Phys. Rev. Lett. **94**, 040405 (2005).
- [Bar04a] M. Bartenstein, A. Altmeyer, S. Riedl, S. Jochim, C. Chin, J. H. Denschlag, and R. Grimm, *Collective excitations of a degenerate gas at the BEC-BCS crossover*, Phys. Rev. Lett. **92**, 203201 (2004).
- [Bar04b] M. Bartenstein, A. Altmeyer, S. Riedl, S. Jochim, C. Chin, J. H. Denschlag, and R. Grimm, *Crossover from a molecular Bose-Einstein condensate to a degenerate Fermi gas*, Phys. Rev. Lett. **92**, 120401 (2004).
- [Bed00] P. Bedaque, E. Braaten, and H.-W. Hammer, *Three-body recombination in Bose gases with large scattering length*, Phys. Rev. Lett. **85**, 908 (2000).
- [Bet00] H. L. Bethlem, G. Berden, F. M. H. Crompvoets, R. Jongma, A. J. A. van Roij, and G. Meijer, *Electrostatic trapping of ammonia molecules*, Nature **406**, 491 (2000).
- [Bev92] P. R. Bevington and D. K. Robinson, *Data reduction and error analysis for the physical sciences*, McGraw-Hill, New York, 1992, 2nd ed.
- [Bly05] P. Blythe, B. Roth, U. Fröhlich, H. Wenz, and S. Schiller, *Production of Ultracold Trapped Molecular Hydrogen Ions*, Phys. Rev. Lett. **95**, 183002 (2005).
- [Bos24] S. Bose, *Plancks Gesetz und Lichtquantenhypothese*, Z. Phys. **26**, 178 (1924).
- [Brü05] R. Brühl, A. Kalinin, O. Kornilov, J. P. Toennies, G. C. Hegerfeldt, and M. Stoll, *Matter Wave Diffraction from an Inclined Transmission Grating: Searching for the Elusive ^4He Trimer Efimov State*, Phys. Rev. Lett. **95**, 063002 (2005).
- [Bra01] E. Braaten and H.-W. Hammer, *Three-body recombination into deep bound states in a Bose gas with large scattering length*, Phys. Rev. Lett. **87**, 160407 (2001).

- [Bra03] E. Braaten and H.-W. Hammer, *Universality in the three-body problem for ^4He atoms*, Phys. Rev. A **67**, 042706 (2003).
- [Bra06] E. Braaten and H.-W. Hammer, *Universality in few-body systems with large scattering length*, Phys. Rep. **428**, 259 (2006).
- [Bri04] F. Bringas, M. T. Yamashita, and T. Frederico, *Triatomic continuum resonances for large negative scattering lengths*, Phys. Rev. A **69**, 040702 (2004).
- [Chi01] C. Chin, *Cooling, Collisions and Coherence of Cold Cesium Atoms in a Trap*, Ph.D. thesis, Stanford University (2001).
- [Chi03] C. Chin, A. J. Kerman, V. Vuletic, and S. Chu, *Sensitive Detection of Cold Cesium Molecules Formed on Feshbach Resonances*, Phys. Rev. Lett. **90**, 033201 (2003).
- [Chi04a] C. Chin, M. Bartenstein, A. Altmeyer, S. Riedl, S. Jochim, J. H. Denschlag, and R. Grimm, *Observation of the pairing gap in a strongly interacting Fermi gas*, Science **305**, 1128 (2004).
- [Chi04b] C. Chin, V. Vuletic, A. J. Kerman, S. Chu, E. Tiesinga, P. Leo, and C. J. Williams, *Precision Feshbach spectroscopy of ultracold Cs_2* , Phys. Rev. A **70**, 032701 (2004), doi:10.1103/PhysRevA.70.032701.
- [Chi05] C. Chin, T. Kraemer, M. Mark, J. Herbig, P. Waldburger, H.-C. Nägerl, and R. Grimm, *Observation of Feshbach-like resonances in collisions between ultracold molecules*, Phys. Rev. Lett. **94**, 123201 (2005), doi:10.1103/PhysRevLett.94.123201.
- [Cla03] N. R. Claussen, S. J. J. M. F. Kokkelmans, S. T. Thompson, E. A. Donley, E. Hodby, and C. E. Wieman, *Very-high-precision bound-state spectroscopy near a ^{85}Rb Feshbach resonance*, Phys. Rev. A **67**, 060701 (2003).
- [CT99] C. Cohen-Tannoudji, B. Diu, and F. Laloë, *Quantenmechanik*, Walter de Gruyter, 1999.
- [Cub03] J. Cubizolles, T. Bourdel, S. J. J. M. F. Kokkelmans, G. V. Shlyapnikov, and C. Salomon, *Production of Long-Lived Ultracold Li_2 Molecules from a Fermi Gas*, Phys. Rev. Lett. **91**, 240401 (2003).
- [Dav95] K. B. Davis, M.-O. Mewes, M. R. Andrews, N. J. van Druten, D. Durfee, D. M. Kurn, and W. Ketterle, *Bose-Einstein Condensation in a Gas of Sodium Atoms*, Phys. Rev. Lett. **75**, 3969 (1995).
- [D'I04] J. D'Incao, H. Suno, and B. Esry, *Limits on universality in ultracold three-boson recombination*, Phys. Rev. Lett. **93**, 123201 (2004).
- [Don02] E. A. Donley, N. R. Claussen, S. T. Thompson, and C. Wieman, *Atom-molecule coherence in a Bose-Einstein condensate*, Nature **417**, 529 (2002).

- [Dür04a] S. Dürr, T. Volz, A. Marte, and G. Rempe, *Observation of Molecules Produced from a Bose-Einstein Condensate*, Phys. Rev. Lett. **92**, 020406 (2004).
- [Dür04b] S. Dürr, T. Volz, and G. Rempe, *Dissociation of ultracold molecules with Feshbach resonances*, Phys. Rev. A **70**, 031601(R) (2004).
- [Dür05] S. Dürr, T. Volz, N. Syassen, G. Rempe, E. van Kempen, S. K. abd B. Verhaar, and H. Friedrich, *Dissociation of Feshbach molecules into different partial waves*, Phys. Rev. A **72**, 052707 (2005).
- [Efi70] V. Efimov, *Energy levels arising from resonant two-body forces in a three-body system*, Phys. Lett. B **33**, 563 (1970).
- [Efi71] V. Efimov, *Weakly-bound states of three resonantly interacting particles*, Sov. J. Nucl. Phys. **12**, 589 (1971).
- [Efi79] V. Efimov, *Low-energy properties of three resonantly interacting particles*, Sov. J. Nucl. Phys. **29**, 546 (1979).
- [Ein25] A. Einstein, *Quantentheorie des einatomigen idealen Gases. Zweite Abhandlung*, Sitzungber. Preuss. Akad. Wiss. **1925**, 3 (1925).
- [Eng06] Thanks to B. Engeser for pointing this out! (2006).
- [Esr99] B. D. Esry, C. H. Greene, and J. P. Burke, Jr., *Recombination of three atoms in the ultracold limit*, Phys. Rev. Lett. **83**, 1751 (1999).
- [Esr06] B. D. Esry and C. H. Greene, *A menage a trois laid bare*, Nature **440**, 289 (2006).
- [Fad61] L. D. Faddeev, *Scattering Theory for a Three Particle System*, Sov. Phys. JETP **12**, 1014 (1961).
- [Fad65] L. D. Faddeev, *Mathematical Aspects of the Tree-Body Problem in the Quantum Scattering Theory*, Israel Program for Scientific Translations (1965).
- [Fed93] D. Fedorov and A. S. Jensen, *Efimov Effect in Coordinate Space Representation*, Phys. Rev. Lett. **71**, 4103 (1993).
- [Fed96] P. O. Fedichev, M. W. Reynolds, and G. V. Shlyapnikov, *Three-Body Recombination of Ultracold Atoms to a Weakly Bound s Level*, Phys. Rev. Lett. **77**, 2921 (1996).
- [Fes58] H. Feshbach, Ann. Phys. **5**, 357 (1958).
- [Fio98] A. Fioretti, D. Comparat, A. Crubellier, O. Dulieu, and F. M.-S. P. Pillet, *Formation of Cold Cs₂ Molecules through Photoassociation*, Phys. Rev. Lett. **80**, 4402 (1998).
- [Gar06] E. Garrido, D. V. Fedorov, and A. S. Jensen, *Efimov Effect in Nuclear Three-Body Resonance Decays*, Phys. Rev. Lett. **96**, 112501 (2006).

- [Geh03] M. E. Gehm, *Preparation of an Optically-Trapped Degenerate Fermi Gas of ${}^6\text{Li}$: Finding the Route to Degeneracy*, Ph.D. thesis, Duke University (2003).
- [Gre02] M. Greiner, O. Mandel, T. Esslinger, and T. W. H. I. Bloch, *Quantum phase transition from a superfluid to a Mott insulator in a gas of ultracold atoms*, Nature **415**, 39 (2002).
- [Gre03] M. Greiner, C. Regal, and D. Jin, *Emergence of a molecular Bose-Einstein condensate from a Fermi gas*, Nature **426**, 537 (2003).
- [Gre05] C. Greene, B. D. Esry, and J. P. D’Incao (2005), private communication.
- [Gri00] R. E. Grisenti, W. Schöllkopf, J. P. Toennies, G. C. Hegerfeldt, T. Köhler, and M. Stoll, *Determination of the Bond Length and Binding Energy of the Helium Dimer by Diffraction from a Transmission Grating*, Phys. Rev. Lett. **85**, 2284 (2000).
- [Gut98] M. C. Gutzwiller, *Moon-Earth-Sun: The oldest three-body problem*, Rev. Mod. Phys. **70**, 589 (1998).
- [Ham02] M. Hammes, D. Rychtarik, H.-C. Nägerl, and R. Grimm, *Cold-atom gas at very high densities in an optical surface microtrap*, Phys. Rev. A **66**, 051401(R) (2002), doi:10.1103/PhysRevA.66.051401.
- [Her03] J. Herbig, T. Kraemer, M. Mark, T. Weber, C. Chin, H.-C. Nägerl, and R. Grimm, *Preparation of a Pure Molecular Quantum Gas*, Science **301**, 1510 (2003), published online 21 Aug 2003, doi:10.1126/science.1088876.
- [Her05] J. Herbig, *Quantum degenerate Cesium: Atoms and Molecules*, Ph.D. thesis, Innsbruck University (2005).
- [Hod05] E. Hodby, S. T. Thompson, C. A. Regal, M. Greiner, A. C. Wilson, D. S. Jin, E. A. Cornell, and C. E. Wieman, *Production efficiency of ultracold Feshbach molecules in Bosonic and Fermionic systems*, Phys. Rev. Lett. **94**, 120402 (2005).
- [Jen04] A. S. Jensen, K. Riisager, D. V. Fedorov, and E. Garrido, *Structure and reactions of quantum halos*, Rev. Mod. Phys. **76**, 215 (2004).
- [Joa75] C. J. Joachain, *Quantum collision theory*, North-Holland Publishing Company Amsterdam · Oxford American Elsevier Publishing Co., Inc - New York, 1975.
- [Joc03a] S. Jochim, M. Bartenstein, A. Altmeyer, G. Hendl, S. Riedl, C. Chin, J. H. Denschlag, and R. Grimm, *Bose-Einstein condensation of molecules*, Science **302**, 2101 (2003).
- [Joc03b] S. Jochim, M. Bartenstein, A. Altmeyer, G. Hendl, C. C. and J. Hecker Denschlag, and R. Grimm, *Pure Gas of Optically Trapped Molecules Created from Fermionic Atoms*, Phys. Rev. Lett. **91**, 240402 (2003).

- [Jul03] P. Julienne and E. Tiesinga, private communication (2003).
- [Ker00] A. J. Kerman, V. Vuletić, C. Chin, and S. Chu, *Beyond Optical Molasses: 3D Raman Sideband Cooling of Atomic Cesium to High Phase-Space Density*, Phys. Rev. Lett. **84**, 439 (2000).
- [Ket99] W. Ketterle, D. S. Durfee, and D. M. Stamper-Kurn, *Making, probing and understanding Bose-Einstein condensates*, in: M. Inguscio, S. Stringari, and C. E. Wieman (Eds.), *Proceedings of the International School of Physics - Enrico Fermi*, 67, IOS Press, 1999, arXiv:cond-mat/9904034.
- [Köh06] T. Köhler, K. Góral, and P. S. Julienne, *Production of cold molecules via magnetically tuneable Feshbach resonances*, arXiv:cond-mat/0601420 (2006).
- [Kin04] T. Kinoshita, T. Wenger, and D. S. Weiss, *Observation of a one-dimensional Tonks-Girardeau gas*, Science **305**, 1125 (2004).
- [Kra] T. Kraemer, M. Mark, P. Waldburger, C. Chin, H.-C. Nägerl, and R. Grimm, *Internal-state interferometry with ultracold molecules*, manuscript in preparation.
- [Kra04] T. Kraemer, J. Herbig, M. Mark, T. Weber, C. Chin, H.-C. Nägerl, and R. Grimm, *Optimized production of a cesium Bose-Einstein condensate*, Appl. Phys. B **79**, 1013 (2004), arXiv:cond-mat/0408268.
- [Kra06] T. Kraemer, M. Mark, P. Waldburger, J. Danzl, C. Chin, B. Engeser, A. Lange, K. Pilch, A. Jaakola, H.-C. Nägerl, and R. Grimm, *Evidence for Efimov quantum states in an ultracold gas of caesium atoms*, Nature **440**, 315 (2006).
- [Lan32] L. D. Landau, Phys. Z. der Sowjetunion **2**, 46 (1932).
- [Lan77] L. D. Landau and E. M. Lifshitz, *Quantum Mechanics: Non-Relativistic Theory*, Pergamon Press, Oxford, 1977, 3rd ed.
- [Mac06] J. H. Macek and J. Sternberg, *Properties of Pseudopotentials for Higher Partial Waves*, Phys. Rev. Lett. **97**, 023201 (2006).
- [Mar05] M. Mark, T. Kraemer, J. Herbig, C. Chin, Hanns-Christoph Nägerl, and R. Grimm, *Efficient creation of molecules from a cesium Bose-Einstein condensate*, Europhysics Letters **69** (2005), arXiv:cond-mat/0409737, doi:10.1209/epl/i2004-10427-7.
- [Mar07a] M. Mark, Ph.D. thesis, University of Innsbruck (2007), manuscript in preparation.
- [Mar07b] M. Mark, J. G. Danzl, T. Kraemer, H.-C. Nägerl, and R. Grimm, *Precision spectroscopy of Feshbach molecules* (2007), to be published.
- [Maz06] I. Mazumdar, A. R. P. Rau, and V. S. Bhasin, *Efimov states and their Fano Resonances in a Neutron-Rich Nucleus*, Phys. Rev. Lett. **97**, 062503 (2006).

- [Met99] H. J. Metcalf and P. van der Straten, *Laser cooling and trapping*, Springer-Verlag, New York, 1999.
- [Mie96] F. H. Mies, C. J. Williams, P. S. Julienne, and M. Krauss, *Estimating Bounds on Collisional Relaxation Rates of Spin-Polarized ^{87}Rb Atoms at Ultracold Temperatures*, J. Res. Natl. Inst. Stand. Tech. **101**, 521 (1996).
- [MS01] F. Masnou-Seeuws and P. Pillet, *Formation of ultracold molecules via photoassociation in a gas of lasercooled atoms*, Adv. At. Mol. Opt. Phys. **47**, 53 (2001).
- [Mud04] M. Mudrich, O. Bünermann, F. Stienkemeier, O. Dulieu, and M. Weidemüller, *Formation of cold bialkali dimers on helium nanodroplets*, Eur. J. Phys. D **31**, 291 (2004).
- [Muk04] T. Mukaiyama, J. R. Abo-Shaeer, K. Xu, J. K. Chin, and W. Ketterle, *Dissociation and Decay of Ultracold Sodium Molecules*, Phys. Rev. Lett. **92**, 180402 (2004).
- [Nie99] E. Nielsen and J. H. Macek, *Low-energy recombination of identical bosons by three-body collisions*, Phys. Rev. Lett. **83**, 1566 (1999).
- [Nie01] E. Nielsen, D. V. Fedorov, A. S. Jensen, and E. Garrido, *The three-body problem with short-range interactions*, Phys. Rep. **347**, 373 (2001).
- [Par04] B. Paredes, A. Widera, V. Murg, O. Mandel, S. Fölling, I. Cirac, T. W. H. G. V. Shlyapnikov, and I. Bloch, *Tonks-Girardeau gas of ultracold atoms in an optical lattice*, Nature **429**, 277 (2004).
- [Pet02] C. J. Pethick and H. Smith, *Bose-Einstein Condensation in Dilute Gases*, Cambridge University Press, 2002.
- [Pet04] D. S. Petrov, C. Salomon, and G. V. Shlyapnikov, *Weakly bound dimers of fermionic atoms*, Phys. Rev. Lett. **93**, 090404 (2004).
- [Pla04] L. Platter, H. W. Hammer, and U. G. Meißner, *The Four-Boson Problem with Short-Range Interactions*, Phys. Rev. A **70**, 052101 (2004).
- [Raa87] E. L. Raab, M. Prentiss, A. Cable, S. Chu, and D. E. Pritchard, *Trapping of Neutral Sodium Atoms with Radiation Pressure*, Phys. Rev. Lett. **59**, 2631 (1987).
- [Reg03] C. A. Regal, C. Ticknor, J. L. Bohn, and D. S. Jin, *Creation of ultracold molecules from a Fermi gas of atoms*, Nature **424**, 47 (2003).
- [Rie05] T. Rieger, T. Junglen, S. A. Rangwala, P. W. H. Pinkse, and G. Rempe, *Continuous loading of an electrostatic trap for polar molecules*, Phys. Rev. Lett. **95**, 173002 (2005).
- [Rob01] J. L. Roberts, N. R. Claussen, S. L. Cornish, E. A. Cornell, and C. E. Wieman, *Controlled Collapse of a Bose-Einstein Condensate*, Phys. Rev. Lett. **86**, 4211 (2001).

- [Rom04] M. W. J. Romans, R. A. Duine, S. Sachdev, and H. T. C. Stoof, *Quantum phase transition in an atomic Bose gas with a Feshbach resonance*, Phys. Rev. Lett. **93**, 020405 (2004).
- [Rus29] H. N. Russell, A. G. Shenstone, and L. A. Turner, *Report on Notation for Atomic Spectra*, Phys. Rev. **33**, 900 (1929).
- [Ryc04] D. Rychtarik, B. Engeser, H.-C. Nägerl, and Rudolf Grimm, *Two-Dimensional Bose-Einstein Condensate in an Optical Surface Trap*, Phys. Rev. Lett. **92**, 173003 (2004), doi:10.1103/PhysRevLett.92.173003.
- [Sch94] W. Schöllkopf and J. P. Toennies, *Nondestructive Mass Selection of Small van der Waals Clusters*, Science **266**, 1345 (1994).
- [Sit91] A. G. Sitenko, *Scattering theory*, Springer Verlag, 1991.
- [SK98] D. M. Stamper-Kurn, H.-J. Miesner, A. P. Chikkatur, S. I. and J. Stenger, and W. Ketterle, *Reversible Formation of a Bose-Einstein Condensate*, Phys. Rev. Lett. **81**, 2194 (1998).
- [Smi06] G. Smirne, R. M. Godun, D. Cassettari, V. Boyer, C. J. Foot, T. Volz, N. Syassen, S. Dürr, G. Rempe, M. D. Lee, K. Goral, and T. Köhler, *Collisional relaxation of Feshbach molecules and three-body recombination in ^{87}Rb Bose-Einstein condensates*, arXiv:cond-mat/0604183 (2006).
- [Sto05] M. Stoll and T. Köhler, *Production of three-body Efimov molecules in an optical lattice*, Phys. Rev. A **72**, 022714 (2005).
- [Str03] K. E. Strecker, G. B. Partridge, and R. G. Hulet, *Conversion of an atomic Fermi gas to a long-lived molecular Bose gas*, Phys. Rev. Lett. **91**, 080406 (2003).
- [Stw76] W. C. Stwalley, *Stability of Spin-Aligned Hydrogen at Low Temperatures and High Magnetic Fields: New Field-Dependent Scattering Resonances and Predissociations*, Phys. Rev. Lett. **37**, 1628 (1976).
- [Sya06] N. Syassen, T. Volz, S. Teichmann, S. Dürr, and G. Rempe, *Collisional decay of ^{87}Rb Feshbach molecules at 1005.8 G* (2006), submitted to Phys. Rev. A.
- [Tha06] G. Thalhammer, K. Winkler, F. Lang, S. Schmid, R. Grimm, and J. H. Denschlag, *Long-lived Feshbach molecules in a 3D optical lattice*, Phys. Rev. Lett. **96**, 050402 (2006).
- [Tho35] L. Thomas, *The interaction between a neutron and a proton and the structure of H^3* , Phys. Rev. **47**, 903 (1935).
- [Tho05a] S. T. Thompson, E. Hodby, and C. E. Wieman, *Spontaneous dissociation of ^{85}Rb Feshbach molecules*, Phys. Rev. Lett. **94**, 020401 (2005).
- [Tho05b] S. T. Thompson, E. Hodby, and C. E. Wieman, *Ultracold Molecule Production via a Resonant Oscillating Magnetic Field*, Phys. Rev. Lett. **95**, 190404 (2005).

- [Tie93] E. Tiesinga, B. J. Verhaar, and H. T. C. Stoof, *Threshold and resonance phenomena in ultracold ground-state collisions*, Phys. Rev. A **47**, 4114 (1993).
- [Tre01] P. Treutlein, K. Y. Chung, and S. Chu, *High-brightness atom source for atomic fountains*, Phys. Rev. A **63**, 51401 (2001).
- [Van02] N. Vanhaecke, W. de Souza Melo, B. L. T. and Daniel Comparat, and P. Pillet, *Accumulation of Cold Cesium Molecules via Photoassociation in a Mixed Atomic and Molecular Trap*, Phys. Rev. Lett **89**, 063001 (2002).
- [Vol05] T. Volz, S. Dürr, N. Syassen, G. Rempe, E. van Kempen, and S. Kokkelmans, *Feshbach spectroscopy of a shape resonance*, Phys. Rev. A **72**, 010704 (2005).
- [Web03a] T. Weber, *Bose-Einstein Condensation of Optically Trapped Cesium*, Ph.D. thesis, University of Innsbruck (2003).
- [Web03b] T. Weber, J. Herbig, M. Mark, and H.-C. N. R. Grimm, *Bose-Einstein Condensation of Cesium*, Science **299**, 232 (2003), published online 5 Dec 2002, doi:10.1126/science.1079699.
- [Web03c] T. Weber, J. Herbig, M. Mark, H.-C. Nägerl, and R. Grimm, *Three-body recombination at large scattering lengths in an ultracold atomic gas*, Phys. Rev. Lett. **91**, 123201 (2003), doi:10.1103/PhysRevLett.91.123201.
- [Wei85] H. Weichenmeier, U. Diemer, M. Wahl, M. Raab, W. Müller, and W. Demtröder, *Accurate ground state potential of Cs₂ up to the dissociation limit*, J. Chem. Phys. **82**, 5354 (1985).
- [Wei98] J. D. Weinstein, R. deCarvalho, T. Guillet, Bretislav Friedrich, and J. M. Doyle, *Magnetic trapping of calcium monohydride molecules at millikelvin temperatures*, Nature **395**, 148 (1998).
- [Xu03] K. Xu, T. Mukaiyama, J. R. Abo-Shaeer, J. K. Chin, and D. E. M. W. Ketterle, *Formation of Quantum-Degenerate Sodium Molecules*, Phys. Rev. Lett. **91**, 210402 (2003).
- [Yam06] M. T. Yamashita, L. Tomio, A. Delfino, and T. Frederico, *Four-boson scale near a Feshbach resonance*, Europhys. Lett. **75**, 555 (2006).
- [Zen32] C. Zener, Proc. Roy. Soc. London Ser. A **137**, 696 (1932).
- [Zwi03] M. Zwierlein, C. Stan, C. Schunck, S. Raupach, S. Gupta, Z. Hadzibabic, and W. Ketterle, *Observation of Bose-Einstein Condensation of Molecules*, Phys. Rev. Lett. **91**, 250401 (2003).
- [Zwi05] M. W. Zwierlein, A. S. J. R. Abo-Shaeer, C. H. Schunck, and W. Ketterle, *Vortices and superfluidity in a strongly interacting Fermi gas*, Nature **435**, 1047 (2005).

Danke!!!

Rudi Grimm, für die Betreuung der Arbeit, für seine Ideen, die zum Gelingen der Arbeit unerlässlich waren und die Gelegenheit auf dem interessanten Gebiet der kalten Atome zu arbeiten;

Hanns-Christoph Nägerl, der jederzeit ansprechbar war und seine vielseitigen Forschungserfahrungen gerne geteilt hat;

Michael Mark, der die Höhen und Tiefen der Arbeit im Labor mit mir geteilt hat, für die zahlreichen Diskussionen, sein Mitdenken und seine Geduld - ohne seinen unermüdlichen Einsatz wäre es nicht gegangen;

Tino Weber und Jens Herbig, die beiden Cs BEC Pioniere, die einen hervorragenden Aufbau hinterlassen haben und ohne die der Start ins Projekt nicht so reibungslos verlaufen wäre;

Cheng Chin, der einen unerschöpflichen Quell an Motivation sein eigen nennt und andere damit infiziert, für sein breites Wissen und zahlreichen Ideen; Francesca Ferlaino, Steven Knoop und Hans Danzl für die entspannte Arbeitsatmosphäre bei gleichzeitiger Höchstleistung am Experiment.

Den ehemaligen Kollegen Matthias Theis, David Rychtarik, Selim Jochim, Markus Bartenstein, Michael Hellwig, Philipp Waldburger und den aktiven Gerhard Hendl, Gregor Thalhammer, Klaus Winkler, Bastian Engeser, Alexander Altmeyer, Mattias Gustavsson, Stefan Riedl, Karl Pilch, Almar Lange, Elmar Haller, Florian Lang, Gabriel Rojas-Kopeinig, Stefan Schmid, Toni Flir, Christoph Kohstall und den Mitgliedern der IQOQI-Gruppe für ihre Unterstützung, den guten Teamgeist in der Forschungsgruppe und die gute Zeit in Innsbruck.

Christine Götsch-Obmascher, Karin Köhle und Patricia Moser im Sekretariat für ihren guten Willen und ihre stete Ansprechbarkeit; Toni Schönherr und Helmut Jordan stellvertretend für die Werkstatt.

Meinen Geschwistern Anna-Katharina und Christian und meinen Eltern, die mir immer eine Heimat gegeben haben.

This page was added on 11 Nov. 2006 after submission of the thesis.